IDŐJÁRÁS

QUARTERLY JOURNAL
OF THE HUNGARIAN METEOROLOGICAL SERVICE

CONTENTS

****

http://omsz.met.hu/irodalom/firat_ido/ido_hu.html

VOL. 105 * NO. 4 * 2001 – VOL. 106 * NO. 1 * 2002

IDŐJÁRÁS

Quarterly Journal of the Hungarian Meteorological Service

Editorial Office: P.O. Box 39, H-1675 Budapest, Hungary or
Gilice tér 39, H-1181 Budapest, Hungary
E-mail: prager.t@met.hu or *antal.e@met.hu*
Fax: (36-1) 346-4809

Subscription by

mail: IDŐJÁRÁS, P.O. Box 39, H-1675 Budapest, Hungary
E-mail: prager.t@met.hu or *antal.e@met.hu*; *Fax: (36-1) 346-4809*

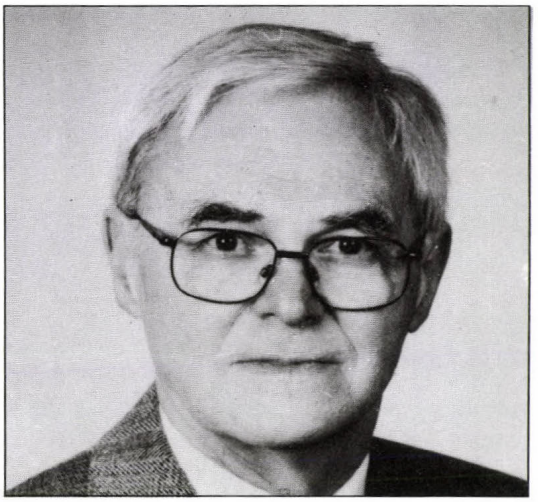

Dr. György Major is 60

Dr. György Major celebrated his 60th birthday in 2001. However a little late, Időjárás, the journal in which a significant part of his excellent scientific papers was published, and for which he had been acting as Editor-in-Chief for four years wishes to celebrate his anniversary with a number containing nine articles written by his friends, colleagues and apprentices, working in Hungary and abroad. The authors dedicate their papers to him as a sign of appreciation for the help and friendship they received and continue to receive from Dr. Major.

Dr. Major is a really honourable and sympathetic main personality of the Hungarian meteorological scientific community and also of the much broader international scientific communities of atmospheric physicists: radiation experts and satellite meteorologists, astronomers, etc. In the name of the Editorial Board, which comprises members from the above communities, and—feeling obliged to do so—in the name of the mentioned communities in the whole, we would like to send you, dear Gyurka, our best regards, and wish you continuing successes in your work and personal life.

Dr. György Major's scientific career

Dr. György Major was born in Beregszász, in 1941. He finished his studies at the Eötvös Loránd University of Budapest in 1964, and received two diplomas, one as teacher of mathematics and physics, and one as meteorologist. Dr. Major started to work at the Hungarian Meteorological Service (HMS) just after finishing the university, where he held various researchers and then leading positions. He achieved his PhD (CSc) degree in 1975, and then the DSc degree in 1981. He published about 80 scientific articles, most of them in English in leading scientific periodicals. He remained faithful to the Service throughout his whole scientific career as an active researcher, until his recent retirement. However, he is active in the HMS even now, fulfilling the position of President of the Scientific Council of the Service.

His scientific interest was always concentrated on the field of atmospheric physics, and especially, atmospheric radiation and satellite meteorology. His major scientific achievements were connected with the methodology of solar radiation measurements, the estimation of circum-solar radiation, the analysis of radiation budget of the Earth-atmosphere system, radiation climatology of Hungary, and industrial-engineering applications of solar radiation. The development of meteorological satellite technology turned his interest more and more to satellite radiation measurements and applications. A basic scientific result of a research team led by him was the compilation of monthly and yearly insolation maps of the Earth's surface that was then published by the World Meteorological Organization.

Beside his scientific activities he had been taking a significant share in the university education of meteorologists for a long time at his mother university and he is one of the authors of the current university text-book on atmospheric physics. One of his successes has been the establishment of a scientific school in atmospheric radiation and satellite meteorology where generations of young scientists received excellent postgraduate education during the years passed. In recent years he has been very active in promoting talented young scientists to achieve academic degrees/titles.

He plays an active role in both domestic and international scientific organizations and societies. In 1993 he was elected a corresponding member and in 1998 a regular member of the Hungarian Academy of Sciences. From 1990 to 1996 he served also as the Chairman of the Meteorological Scientific Committee of the Academy. From 1993 he has been serving as Secretary-General of the Hungarian Meteorological Society, he acted as Secretary-General of the Hungarian Astronautical Society in the period 1985–1993, and as President of the same society in the years 1997–2000. He also worked as the Editor-in-Chief of the present 106 years old scientific periodical from 1995 to 1998. As regards his memberships in international organizations, he is a Member of the International Radiation Commission, a commission of ICSU/IUGG/IAMAS, and also the Commission for Atmospheric Sciences of the WMO. He had been working for a long period as the Director of the Regional Radiation Centre in Budapest, which is a part of the Baseline Surface Radiation Network (a WMO/ICSU organization).

IDŐJÁRÁS

Quarterly Journal of the Hungarian Meteorological Service
Vol. 105, No. 4 — Vol. 106, No. 1, October 2001 — March 2002, pp. 189–205

Shortwave radiation budget of the Earth: Absorption and cloud radiative effects

Istvan Laszlo[1] and **Rachel T. Pinker**[2]

[1]*NOAA/NESDIS/Office of Research and Applications; Camp Springs, MD 20746, USA;*
[2]*Department of Meteorology, University of Maryland, College Park, MD 20742, USA*
E-mails: Istvan.Laszlo@noaa.gov; pinker@atmos.umd.edu

(Manuscript received October 29, 2001; in final form December 31, 2001)

Abstract—The University of Maryland, Global Energy and Water Cycle Experiment, Shortwave Radiation Budget algorithm was used with satellite data from the D1 product of the International Satellite Cloud Climatology project to estimate monthly values of the shortwave top of atmosphere (TOA) and surface fluxes for the period of July 1983–June 1994. Based on this data set, regional, zonal and global averages of absorption and cloud radiative effects are examined in the total shortwave spectrum. Absorption of radiation varies significantly both regionally and with latitude. Out of the 342 W m^{-2} of radiation arriving annually from the Sun at the top of the atmosphere 240 W m^{-2} is absorbed by the Earth. Annual global mean atmospheric and surface absorption are larger by 11 and 34 W m^{-2}, respectively, for land than for ocean. The top of atmosphere radiation budget is in good agreement with those from the ERBE and ScaRaB missions.The global annual average SW flux absorbed at the surface from this study is 165 W m^{-2}, and agrees well with other satellite studies. However, this value is about 20 W m^{-2} larger than the absorption indicated by studies that employ radiation data measured at ground sites. SW cloud radiative forcing at the TOA and the surface from this study is –46 W m^{-2} and –49 W m^{-2}, respectively.

Key-words: cloud radiative forcing, GEWEX/SRB algorithm, shortwave radiation budget, solar absorption, solar net flux, solar radiation

1. Introduction

The planet Earth receives energy from space in the form of solar radiation. Part of this energy is reflected back to space and part of it is absorbed by the atmosphere and the surface. Part of the absorbed solar energy is then re-radiated back to space in the form of thermal (infrared) radiation, and part of it will drive the weather and determine the climate. The measure of this energy

exchange between the planet Earth and space is the planetary radiation budget. A similar budget is defined to measure the energy exchange between the atmosphere and the surface.

Clouds play a key role in shaping the energy exchange both at the planetary and surface level. Because of their generally higher albedo, they reflect more solar radiation to space than a cloudless atmosphere would, and thus reduce the energy available for absorption by the atmosphere and the surface. On the other hand, they reduce the heat lost to space by reemitting part of the thermal radiation towards the surface. The physical mechanism and the effect of this cloud-induced change on the interaction between radiation and climate are rather complex, and in some cases not yet fully understood. For example, recent studies of the top of atmosphere radiation budget observed by satellites show decadal variations at the level of 4 W m^{-2} in shortwave (SW) and longwave (LW) fluxes, and about 1 W m^{-2} in total net flux across the entire tropics. This variability is caused by changes in cloudiness, an observational fact that current climate models cannot capture (*Wielicki et al.*, 2002). The decadal variations in the radiative fluxes are consistent with other meteorological fields and show a decadal change in the strength of the Hadley and Walker circulations (*Chen et al.*, 2002). Data from the CERES (Clouds and the Earth's Radiant Energy System) instrument on the TRMM (Tropical Rainfall Measuring Mission) satellite showed dramatic changes in the effect clouds have on the SW and LW radiation in early 1998. These changes were caused by a factor of two drop in the median cloud altitude over the western Pacific Ocean Warm Pool. The cloud height changes were shown to be related to the total shutdown of the tropical Walker Cell circulation. Preliminary studies show that climate models are not currently capturing this signal very well (*Cess et al.*, 2001).

Early studies of the radiation budget calculated the flux components from estimates of the radiative properties of the atmosphere and the surface (e.g., *Budyko*, 1974). Satellite data offer improvements over the early estimates of the planetary budget in two ways: 1) they provide a more accurate observation of atmospheric and surface properties, and 2) the planetary radiation budget is directly observed. The surface radiation budget is usually obtained from the planetary budget using models, since surface radiation is not observed directly from space. However, even for the surface budget, satellite data clearly present advantages by providing a constraint at the top of atmosphere via the requirement of conservation of energy in the total surface-atmosphere system. Over the past decade or so, there have been a number of studies that employ various satellite data to infer the radiation budget, or at least some component of it. For example, SW radiation budget parameters were estimated from the International Satellite Cloud Climatology Project (ISCCP) data by *Bishop* and *Rossow* (1991), *Darnell et al.* (1992), *Pinker* and *Laszlo* (1992), *Rossow* and

Zhang (1995), and from the Earth Radiation Budget Experiment (ERBE) data by *Li* and *Leighton* (1993).

In the current paper, only the shortwave (SW) component of the radiation budget is presented. We define shortwave as the electromagnetic spectrum between 0.2 and 4.0 μm. The SW radiation budget was obtained from the D1 product of the ISCCP using Version 2.1 of the University of Maryland (UMD), Global Energy and Water Cycle Experiment (GEWEX), Shortwave Radiation Budget (SRB) algorithm (*Pinker* and *Laszlo*, 1992; *Laszlo* and *Pinker*, 1997). Downward and upward radiative fluxes at the top of the atmosphere and at the surface were calculated for 6596 equal-area cells covering the entire globe at every three hours for a period of about 11 years (July 1983–August 1994). Each cell represents an area of about 280×280 km. Selected daily and monthly SW fluxes from this data set are also available on a CD-ROM (*University of Maryland Shortwave Radiation Budget Daily and Monthly Data Set, July 1983–August 1994, D1 Product Version 1.0, June 2000*) upon request from the Department of Meteorology, University of Maryland, College Park, MD 20742, USA (e-mail: srb@atmos.umd.edu). The new data set represents an improvement over the previous radiation budget data provided in the *First WCRP Surface Radiation Budget Global Data Sets, Short-wave Radiation Parameters March 1985–December 1988 (Version 1.1)*, and distributed by the NASA Earth Observing System Distributed Active Archive Center at NASA Langley Research Center, Hampton, VA, USA (*Whitlock et al.*, 1995). The latter data set used the C1 data of ISCCP, while the current data are based on the D1 product. The ISCCP D1 product is an improved version of the C1 product (*Rossow* and *Schiffer*, 1999); the improvements, among others, are related to a new cloud screening methodology that resulted in a better cloud detection over snow, in particular, in the polar regions. Differences of D1 and C1 estimates of the surface downward flux were found to be large ($\sim$100 W m^{-2}) on a regional scale at high latitudes, but zonal average differences were less than 10 W m^{-2} for tropical and middle latitude regions (*Laszlo et al.*, 1997). In addition to using the D1 data of ISCCP, the UMD/GEWEX/SRB algorithm applied in the new data set is an improved version of the one used in Version 1.1 of the WCRP/SRB data. Following *Ramaswamy* and *Freidenreich* (1992), Version 2.1 of the algorithm employs a more accurate parameterization of water vapor absorption as described in *Laszlo* and *Pinker* (1997).

In Section 2, we briefly describe the UMD/GEWEX/SRB algorithm and the ISCCP D1 satellite data that are used to obtain the SW radiation budget data set. Next, in Section 3, we present results on the radiation budget, concentrating on absorption and radiative effects of clouds. A brief analysis of the same data set has already been presented by *Pinker et al.* (2000). In the current

paper, we expand on that work, and present a more comprehensive analysis of global fluxes. Finally, in Section 4, we offer some conclusions and a summary of the main results.

2. *Flux retrieval method and input data set*

2.1 The UMD/GEWEX/SRB algorithm

Version 2.1 of the UMD/GEWEX/SRB algorithm (hereafter referred to as the UMD algorithm) determines the upward and downward shortwave fluxes at the top of the atmosphere and at the surface from satellite-derived clear and cloudy radiances, clear-sky composite radiance, cloud cover fraction, as well as the total amount of water vapor and ozone (*Pinker* and *Laszlo*, 1992; *Laszlo* and *Pinker*, 1997). The radiative fluxes are calculated in five spectral intervals, 0.2–0.4, 0.4–0.5, 0.5–0.6, 0.6–0.7, and 0.7–4.0 μm, by determining the atmospheric transmission and reflection and surface albedo pertaining to a particular satellite observation. This is done by comparing the satellite-measured top of atmosphere (TOA) shortwave reflectance to a radiative model of the surface-atmosphere system. The former is estimated from the narrowband radiance observed by the satellite, using spectral and angular transformations between narrowband radiance and shortwave reflectance. The radiative model accounts for absorption by the radiatively most important gases (water vapor and ozone), and multiple scattering by cloud and aerosol. Absorption by ozone and water vapor is parameterized following *Lacis* and *Hansen* (1974) and *Ramaswamy* and *Freidenreich* (1992), respectively. Optical properties and vertical distribution of the concentration of aerosols are from the Standard Radiation Atmospheres (WCP-55, 1983). Extinction properties of clouds are derived from the parameterization of *Stephens* (1978) and *Stephens et al.* (1984). A single cloud layer placed between 2 and 5.5 km is assumed. The radiative transfer in this plane parallel, vertically inhomogeneous, scattering and absorbing atmosphere is solved by the delta-Eddington method based on the numerical algorithm of *Wiscombe* (1977). To ensure fast performance on a global scale, the radiative model is made available for the flux retrieval in the form of a pre-calculated look-up table. The look-up table describes the relationship between reflectance and transmittance for a representative (discrete) set of water vapor and ozone amounts, aerosol and cloud optical depths, and solar zenith angles.

In deriving the fluxes, first the surface albedo is estimated from the clear-sky composite reflectance by correcting it for Rayleigh scattering, aerosol extinction and absorption by ozone and water vapor. In this step, the amount of

aerosol is specified according to the Standard Radiation Atmospheres *(WCP-55*, 1983). Next, two sets of atmospheric transmittance-reflectance pairs are selected from the look-up table according to the input solar zenith angle, water vapor and ozone amount, and combined with the surface albedo to yield shortwave TOA reflectances. The two sets are for clear and cloudy conditions with varying values of the aerosol and cloud optical thickness, respectively. Finally, clear-sky and cloudy-sky transmittances and fluxes are obtained by adjusting the model aerosol and cloud optical thickness until the clear and cloudy TOA reflectances match, respectively, the shortwave reflectances derived from the satellite-observed clear-sky and cloudy-sky radiances. The clear-sky and cloudy-sky fluxes are then weighted according to the cloud cover fraction to yield the all-sky flux. In addition to the all-sky flux, the clear-sky flux is also saved, thus making it possible to quantify the radiative effects of clouds. Although fluxes are calculated in the five spectral intervals listed above, in the final product, they are summed up to provide values in three broad intervals: visible (VIS: 0.4–0.7 μm), near infrared (NIR: 0.7–4.0 μm) and shortwave (SW: 0.2–4.0 μm).

The key features of the UMD algorithm that set them apart from similar algorithms are:

- fully physical (the relationship between surface and top of the atmosphere radiative fluxes are obtained from radiative transfer theory);
- spectral and solar zenith angle dependence of the surface reflectance are included;
- cloud optical depth dependent on cloud type (effective radius of droplets changes);
- aerosol absorption explicitly included, even under cloudy conditions;
- direct and diffuse components of fluxes are separated (improved modeling of radiative interaction with vegetation and oceans is possible);
- modular (improvements in the representation of physics in the algorithm can easily be incorporated; different sets of satellite data can be used).

The various elements of the UMD/GEWEX/SRB algorithm have been tested in a number of different ways. The radiative transfer component was evaluated in the framework of the Intercomparison of Radiation Codes in Climate Models (ICRCCM). The UMD fluxes were in good agreement with those from high-resolution radiative transfer models (*Fouquart et al.*, 1991). The differences in atmospheric absorption, when compared to high-resolution computations, are about 2% and 7% for the clear and the cloudy cases, respectively. A validation of satellite-estimated monthly-mean downward fluxes at the surface against ground measurements showed that, on the average, biases

are less than 20 W m^{-2} (*Whitlock et al.*, 1995). However, the satellite-estimated fluxes are less accurate in regions of intense biomass burning and heavy aerosol concentrations (*Konzelmann et al.*, 1996).

The UMD algorithm estimates a relatively large number of SRB parameters (spectral upward and downward, total and diffuse fluxes at the top of atmosphere and at the surface for clear-sky and all-sky conditions). Among these, for the current study, we selected parameters that quantify the absorption of solar radiation and the radiative effects of clouds.

The amount of radiation absorbed by the earth-atmosphere system is measured by the difference of the incoming and exiting radiative fluxes, and is referred to as the net flux (NF). The net flux at TOA is obtained from the satellite data, and is considered measured. The net flux at the surface is measured directly only at a limited number of sites; on a global scale, it is usually derived from the TOA net flux using a relationship between TOA and surface values. This relationship is either estimated empirically or obtained from modeling. In the UMD algorithm, the connection between TOA and surface net fluxes is established from radiative transfer simulations, and essentially amounts to the following relationship (*Laszlo* and *Pinker*, 1994):

$$\begin{aligned} n_{SRF}(\mu_0) &= A + B\, n_{TOA}(\mu_0), \\ B &= (1-\tilde{r}) / \tilde{t}, \\ A &= t_0(\mu_0) - B(1 - r_0(\mu_0)), \end{aligned} \tag{1}$$

where n_{TOA} and n_{SRF} are the fractional TOA and surface net fluxes, respectively, t_0, $\tilde{t}$, r_0 and $\tilde{r}$ are the planar and spherical transmissivity and reflectivity of the atmosphere, and μ_0 is the cosine of the solar zenith angle. Since, as it was shown in *Laszlo* and *Pinker* (1994), A and B varies relatively weakly with changing atmospheric condition, the above relationship is very closely linear.

Clouds modulate the radiative energy exchange between the atmosphere and its boundaries (space and the surface). Since the albedo of clouds is usually larger than that of the cloudless sky, they reflect more radiation to space and transmit less radiation to the surface, and thus reduce the shortwave radiation absorbed by the atmosphere-surface system. This ability of clouds to force changes in the source and sink terms of the energy budget is referred to as cloud radiative forcing (CRF). A measure of this forcing is the difference between the all-sky and clear-sky net fluxes (NF_{all} and NF_{clear}) (e.g., *Ramanathan et al.*, 1989), and is defined as

$$CRF = NF_{all} - NF_{clear}. \tag{2}$$

2.2 *Input data*

The input data used in this study for the UMD algorithm are from the D1 product of the International Satellite Cloud Climatology Project (ISCCP) (*Rossow* and *Schiffer,* 1999). ISCCP is a project of the World Climate Research Programme (WCRP) with the objective of collecting and analyzing satellite radiance measurements to infer the spatial and temporal distribution of cloud radiative properties on a global scale. It began its collection of visible and infrared radiances from the imaging radiometers onboard an array of operational weather satellites in July 1983. The array consists of the NOAA polar orbiters and the geostationary satellites, GOES, METEOSAT and GMS. First, the radiances are sampled to reduce data volume, then radiometrically calibrated and navigated, and finally placed in a common format.

The visible ($\approx$ 0.6 μm) and infrared ($\approx$ 11 μm) radiances common to all satellites are normalized to those of the Advanced Very High Resolution Radiometer (AVHRR). The normalization procedure attempts to create a uniform radiance set for the whole globe. The calibration of the AVHRR is monitored and the calibration standard is transferred from one satellite to the next in the NOAA series. The radiances are sorted according to whether they correspond to clear or cloudy scenes. The analyzed radiances are merged with the TIROS Operational Vertical Sounder (TOVS) daily analysis product produced by the National Oceanic and Atmospheric Administration (NOAA) and the weekly snow/ice cover data from the NOAA/National Environmental Satellite Data and Information Service (NESDIS) and NAVY/NOAA Joint Ice Center. The D1 data have a nominal spatial resolution of about 280 km, 6596 equal-area grid cells make up the whole globe. The data are provided at a nominal temporal resolution of 3 hours. The D1 product differs from the earlier C1 product (*Schiffer* and *Rossow*, 1985), in that the analysis method used to produce it was changed to improve cirrus cloud detection over land, low-level cloud detection over snow and ice by using 3.7-μm radiances, etc.

The D1 parameters used as input to the UMD algorithm are the mean visible clear, cloudy and clear-sky composite radiances, column amount of ozone and precipitable water amount, solar and satellite zenith and relative azimuth angles at every three hours. The fluxes retrieved at this temporal resolution are summed over a day to obtain daily values, and over a month to get monthly values. Fluxes for all three temporal resolutions are saved in the UMD/SRB product. In the next section, we present an analysis of the monthly results.

3. Results

Using the ISCCP D1 data in the UMD algorithm leads to SRB parameters at the three-hourly, daily and monthly time scales, however in the current study, we present results only for the monthly means.

3.1 Regional distribution

Mean values of the shortwave radiation absorbed by the atmosphere-surface system and those at the surface (TOA and surface net fluxes) for all-sky and clear-sky conditions were calculated for each of the 6596 equal-area ISCCP grid cell by averaging the 132 monthly values covering the period between July 1983 and June 1994. The regional distribution of the mean values for all-sky conditions is presented in *Fig. 1*. The comparison of the two fields reveals a high degree of similarity. This similarity suggests a strong correlation between TOA and surface net fluxes, a fact that has been exploited to retrieve surface solar absorption from satellite-measured TOA albedo, as mentioned in the previous section. Both fields show strong solar zenith angle dependence that is mainly modified only by persistent cloud cover. The largest absorption (> 300 W m^{-2}) by the system occurs over tropical oceanic regions with relatively low cloud cover. Poleward of 70° latitude, the absorbed energy is less than about 100 W m^{-2}. The surface absorption in the tropics is about 100 Wm^{-2} less than the system absorption and it is generally 50–100 W m^{-2} less over land than over ocean. On a global scale, the smallest surface absorption occurs in the polar regions, as expected, due to the high surface albedo and low surface irradiance available for absorption there. The largest absorption is in the equatorial Pacific Ocean between the longitudes of about 120°W and 150°W.

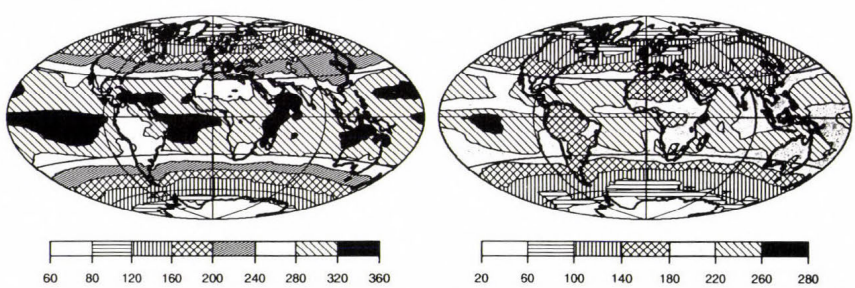

Fig. 1. Geographical distribution of annual mean shortwave energy absorbed by the earth-atmosphere system (left panel) and that by the surface (right panel) for all-sky conditions. Units are W m^{-2}.

The difference between the TOA and surface net flux is the flux absorbed by the atmosphere. The regional distribution of its ratio to the TOA solar irradiance is shown in *Fig. 2* for all-sky conditions. Atmospheric absorption varies between 18% and 28% regionally. The smallest absorption occurs over relatively clear oceanic regions, while the largest absorption is over the tropical land areas of South America, equatorial Africa, most of the Sahara and the Arabian Peninsula, Pakistan and northeast India. A somewhat enhanced absorption, relative to clear regions, is observed in the cloudy Intertropical Convergence Zone (ITCZ), just north of the equator. Because of the markedly different optical depths of clouds and aerosols over ocean and land, the gradient of absorption is the largest along the coastlines. This large gradient is, however, not necessarily realistic everywhere, since the aerosol optical depth field was initialized by a rather rudimentary climatology that assumed a visible optical depth of 0.1 over ocean and 0.23 over land. The clear-sky atmospheric absorption (not shown) varies over a somewhat larger range than that of the all-sky; it ranges from 17% to 32%. The low values are concentrated over the Southern-Hemisphere oceans between the latitudes of about 30°S and 60°S. Large values of absorption can be observed over the equatorial land areas, similar to that seen for all-sky.

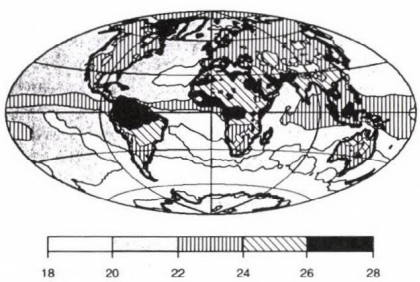

Fig. 2. Geographical distribution of annual mean shortwave radiation absorbed by the all-sky atmosphere in percent of the TOA irradiance.

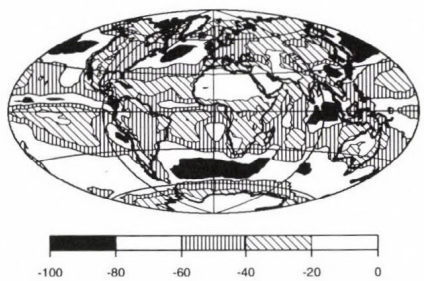

Fig. 3. Geographical distribution of annual mean shortwave cloud radiative forcing at the surface. Units are W m^{-2}.

The effect of clouds on the annual surface shortwave radiative energy budget is shown in *Fig. 3.* All forcing values are negative, indicating that clouds reduce the energy available for absorption at the surface in the shortwave spectrum (SW cooling). The largest forcing is observed over the northern Atlantic and Pacific oceans, to the south of the African continent and over the Asian monsoon region to the south of India. It is the result of the persistent

cloud cover in these regions and the high albedo of clouds compared to the dark ocean surface. Somewhat weaker shortwave cloud forcing is associated with the deep convective regions over central Africa and the Amazon. Similarly, a significant cloud forcing is evident off the west coast of Africa, in the regions of stratocumulus clouds off the coast of California and Chile and near the Philippines and over the ITCZ. Low shortwave cloud forcing values are found over the Sahara, the Arabian Peninsula, most of Australia, to the south of the ITCZ, over Greenland and for the snow/ice covered Polar regions. Cloud forcing at the TOA (not shown) is similar to that at the surface, except its magnitude is somewhat smaller.

3.2 Zonal averages

Total column SW absorption, that is the absorption by the atmosphere-surface system, varies significantly with latitude (*Fig. 4*). It is about 40% in the polar latitude bands, while it reaches about 75% in the tropics. Most of the SW absorption occurs at the surface. It is also the surface absorption that defines the latitudinal variation of the column absorption, since the atmospheric absorption varies only very slightly with latitude as shown in the lower panel of *Fig. 4*. There is a slight asymmetry between the northern (NH) and southern hemisphere (SH) atmospheric absorption; the northern-hemisphere atmospheric absorption is slightly larger (22.3%) than that of the southern hemisphere (20.9%). Surface SW absorption is, however, somewhat larger over the southern hemisphere, and almost balances the larger northern hemisphere atmospheric absorption in the hemispheric column absorptions, leading to SW column absorptions of 68.4% (NH) and 67.9% (SH).

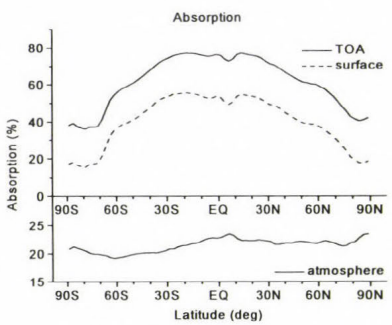

Fig. 4. Zonal mean of annual mean absorption by the atmosphere-surface system, by the atmosphere and by the surface under all-sky conditions.

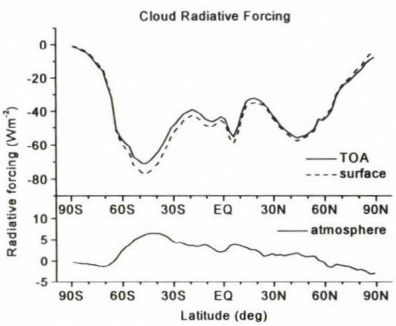

Fig. 5. Zonal mean of annual mean cloud radiative forcing at TOA, at the surface and of the atmosphere.

The SW cloud radiative forcing also exhibits a strong latitudinal dependence (*Fig. 5*). The largest forcing (more negative) values occur in the northern and southern hemisphere storm tracks (around 45°N and 45°S), and the smallest forcing is at high latitudes. At high latitudes, a large part of the radiation is already reflected back by the bright snow/ice cover even under clear skies, and the presence of clouds does not change this significantly. Except for zones of high latitudes, surface cloud forcing is stronger than the TOA forcing.

3.3 Global annual mean

Annual mean net fluxes of the 6596 equal-area cells were averaged to obtain global mean values. Because of the lack of satellite observations at certain high latitudes, some cells have no fluxes reported. To reduce the effect these missing cells might have on the global average, monthly average of the TOA downward flux was calculated both analytically and numerically from the available cells, and all fluxes were multiplied by the ratio of numerical to analytical TOA flux. To facilitate comparisons with other studies, we assumed a solar constant of 1367 W m^{-2} for the analytical TOA downward flux, although in the UMD algorithm the solar constant is 1372.6 W m^{-2}. This led to a global annual mean SW irradiance of 342 W m^{-2} at the TOA. Global annual mean radiation budget parameters at the top of atmosphere and at the surface are summarized in *Table 1*. The parameters listed in this table include the all-sky downward flux, net flux, albedo and cloud radiative forcing. The global average of the SW radiation absorbed at the surface is 165 W m^{-2}. The atmosphere absorbs an additional 75 W m^{-2}, bringing the total solar energy absorbed by the system to 240 W m^{-2}. Global annual SW cloud radiative forcing at the surface is 3 W m^{-2} larger than at the TOA.

Table 1. Global annual mean all-sky downward flux (DF), net flux (NF), albedo (A), and cloud radiative forcing (CRF) at the top of atmosphere (TOA), at the surface and of the atmosphere. Fluxes and cloud radiative forcing are in W m^{-2}

Global annual mean shortwave radiation budget parameters									
TOA				Surface				Atmosphere	
DF	NF	A	CRF	DF	NF	A	CRF	NF	CRF
342	240	0.298	–46	188	165	0 122	–49	75	3

Table 2 presents a comparison between global annual mean SW radiation budget parameters in the present study and those obtained from other studies. The comparison is admittedly not comprehensive, however the selected studies do represent different approaches for estimating the solar radiation budget.

Some of these studies are concerned with only the surface or the TOA radiation budget, but four of them address both the TOA and the surface absorption. All studies, except one, employ satellite data. *Ohmura* and *Gilgen* (1993) use radiation data directly observed at the ground along with estimates of the surface albedo, and report a global annual value of surface-absorbed solar radiation (net flux (NF) at surface) of 142 W m^{-2}. *Major* (1998) finds a value of 146 W m^{-2} for the same quantity in two earlier studies. In one of these studies, *Major* (1976) used a limited sample of Nimbus-3 satellite data and surface radiation data, and obtained an annual mean global surface-absorbed solar radiation of 43%. Subsequently, combining an extended number of surface data with global satellite observation of cloudiness, *Major et al.* (1981) received a value of 146 W m^{-2} for the surface-absorbed solar flux. The latter value is in close agreement with that of *Ohmura* and *Gilgen* (1993). *Li et al.* (1997), who used satellite data from the Earth Radiation Budget Experiment (ERBE) along with a highly parameterized form of the radiative transfer, received a value that is 15 W m^{-2} larger than that of *Ohmura* and *Gilgen* (1993). *Rossow* and *Zhang* (1995) applied the C1 data of ISCCP and a modified version of the NASA/Goddard Institute for Space Studies (GISS) radiative transfer model, and arrived at the same value of surface absorption as the one found in the current study, which is 23 W m^{-2} higher than the one by *Ohmura* and *Gilgen* (1993). The highest surface absorption (168 W m^{-2}) reported in this comparison is from *Kiehl* and *Trenberth* (1997), who used model calculations constrained by satellite observations at TOA. Although the surface absorption is the same in the *Rossow* and *Zhang* (1995) study and in the current (UMD) study, the shortwave radiation absorbed by the atmosphere differs in the two studies; the UMD model atmosphere absorbs 10 W m^{-2} more radiation. The UMD atmospheric absorption is in the middle of the range listed in *Table 2*; in which the highest atmospheric absorption (83 W m^{-2}) is obtained by *Li et al.* (1997). Both *Rossow* and *Zhang* (1995) and the current study use the ISCCP satellite data, however, the former is based on the C1 product while the latter employs the more recent D1 data. The water vapor data in these products are different, and this difference contributes to the difference observed in the atmospheric absorption in the two studies. The TOA albedo is also higher in the *Rossow* and *Zhang* (1995) study; this means more radiation is reflected back to space and less is available for absorption in the atmosphere. The difference in cloud cover in the two ISCCP products contributes to the difference seen in TOA albedos. In addition, the two studies employ different methods to derive fluxes. *Rossow* and *Zhang* (1995) take the cloud optical depth and surface reflectance directly from the ISCCP product and calculate surface and TOA radiation budget parameters from these. The UMD algorithm, on the other hand, uses the ISCCP radiances and retrieves the cloud optical depth and surface re-

flectance independently of ISCCP. In the process, the UMD algorithm uses angular and spectral transformations of the radiance to TOA albedo that are derived from the ERBE data. This results in an annual mean global TOA albedo of 30% that is in agreement with the value obtained from ERBE, and independently from the more recent French-Russian-German Scanner for Radiation Budget (ScaRaB) project (*Kandel et al.*, 1998). The global annual mean value of the shortwave TOA cloud radiative forcing (CRF) ranges from –46 W m^{-2} to –54 W m^{-2}. It is interesting to note that the two extreme values come from the two studies that use the ISCCP data. The CRF value from *Kiehl* and *Trenberth* (1997) is in the middle of this range. The ERBE and the ScaRaB data sets, which are considered two of the best TOA radiation budget data sets today, lead to a CRF value of –48 W m^{-2}. (The same CRF value of *Li et al.* (1997) is not independent from the ERBE value, since at the TOA, it only represents a direct application of the clear and all sky data from the ERBE.)

Table 2. Comparison of global annual mean SW radiation budget parameters (solar constant, all-sky flux reflected at TOA (UF), net flux (NF) at the surface and of the atmosphere and cloud radiative forcing (CRF) at TOA). The parameters listed are from *Major et al.* (1981), *Ohmura* and *Gilgen* (1993) (OG), *Li et al.* (1997) (LMA), *Kiehl* and *Trenberth* (1997) (KT), *Rossow* and *Zhang* (1995) (RZ), the ERBE and the ScaRaB satellite experiments, and the present study (UMD). Fluxes and cloud radiative forcing are in W m^{-2}. TOA albedos in percent are also given (in parenthesis)

Comparison of global annual mean SW radiation budget parameters								
	Major et al. (1981)	OG	LMA	KT	RZ ISCCP C1	UMD ISCCP D1	ERBE Mar 85–Feb 89	ScaRaB Mar 94–Feb 95
Solar constant			1365	1367	1366	1367		
UF at TOA			101		112	102	101	102
			(30)	(31)	(33)	(30)	(30)	(30)
NF of atm			83	67	65	75		
NF at surface	146	142	157	168	165	165		
CRF at TOA			–48	–50	–54	–46	–48	–48

Ohmura and *Gilgen* (1993) used data from the Global Energy Balance Archive (GEBA) to evaluate the global surface solar radiation budget. The main source of the radiation data in GEBA is the data collected by the World Radiation Data Center in St. Petersburg, Russia. *Major* (1976) and *Major et al.* (1981) also used radiation data from the same network of stations. The above studies use relationships based on radiation data at these stations and conventional or satellite data to extrapolate the SRB to a global scale. These stations are concentrated on land areas, and it is not obvious if and how they can be used to estimate SRB on a global scale. To estimate the differences between SRB parameters for different scenes, we calculated averages sepa-

rately from the land, ocean and costal ISCCP grid cells. The result for all-sky conditions is summarized in *Table 3*. Because the average land surface albedo is about three times that of the ocean, surface absorption for land is expected to be smaller than the oceanic value of 175 W m^{-2}. The annual surface-absorbed solar radiation averaged for land cells is 141 W m^{-2}; this, incidentally, is almost exactly the same value that *Ohmura* and *Gilgen* (1993) obtained for the global average. Although the cloud cover averaged for land cells is smaller than that averaged for ocean cells, the amount of radiation available for absorption at the surface is less because the average optical depth is about three times larger over land than over ocean. In spite of the larger cloud optical depth over land, the TOA shortwave cloud radiative forcing over land is 16 W m^{-2} weaker than that over ocean. The atmosphere over land areas absorbs 10 W m^{-2} more SW radiation than the atmosphere over the oceans. SRB values for coastal cells lie between the values for land and ocean cells.

Table 3. Global annual mean SW all-sky net flux at the top of atmosphere (TOA), at the surface (SRF) and of the atmosphere (ATM) for land, ocean, coastal and all ISCCP-D1 cells. SW TOA cloud radiative forcing (CRF), cloud fraction (CF) and cloud optical thickness (τ) are also listed along with all-sky SW TOA and surface albedos (A_{TOA}, A_{SRF}). Net fluxes and CRF are in W m^{-2}

SW radiation budget parameters for various scene types								
	TOA	SRF	ATM	CRF	CF	τ	A_{TOA}	A_{SRF}
All	240	165	75	–46	0.67	10.6	0.298	0.122
Land	224	141	83	–34	0.60	21.7	0.345	0.250
Ocean	247	175	72	–50	0.70	6.5	0.278	0.074
Coast	236	160	76	–42	0.67	14.5	0.310	0.140

4. Summary and conclusions

We used the ISCCP D1 data as input to the UMD/GEWEX/SRB algorithm to estimate monthly values of the shortwave TOA and surface net fluxes for the period of July 1983–June 1994 (132 months). Shortwave radiation absorbed by the atmosphere-surface system has a strong regional and zonal variability. Annual global mean atmospheric and surface absorption for land and ocean areas differ by 11 and 34 W m^{-2} , respectively. The global annual average SW flux absorbed at the surface from this study is 165 W m^{-2}; this agrees with the value reported by *Rossow* and *Zhang* (1995), but it is 19 W m^{-2} larger than the value reported by *Major* (1998) and 23 W m^{-2} larger than the average obtained by *Ohmura* and *Gilgen* (1993). The latter studies used direct observations of the downward SW irradiance; however, the surface albedo was estimated indirectly with a potentially large uncertainty. An additional source of uncertainty

in the latter estimates is the uneven spatial coverage of station data. Sources of errors in the UMD/SRB parameters are also numerous. For example, misclassification of scenes in the satellite data results in erroneous spectral and angular transformations. Even if the scene identification is correct, the spectral and angular transformations applied to three-hourly radiances are valid only in a statistical sense. Moreover, the surface albedo retrieval assumes only a very rudimentary aerosol climatology, which in turn affects the flux retrievals. The radiative transfer and the inversion procedure assume plane parallel clouds and account for the current state of knowledge about cloud-radiation interactions. Several recent studies (e.g., *Cess et al.*, 1995) suggest that clouds may absorb about 20–25 W m^{-2} more SW radiation than is calculated by models, including the one used in the current study. The additional absorption would reduce the surface absorbed flux reported in this study to 145 W m^{-2}, bringing it into agreement with the values reported by *Ohmura* and *Gilgen* (1993) and by *Major* (1998). At the same time, atmospheric absorption would increase to 95 W m^{-2}, which would make this the highest value in *Table 2*. However, the existence of this "anomalous" cloud absorption is not universally accepted. It is argued that although an increased absorption may exist in the tropics, it is more likely caused by underestimation of the aerosol absorption in that region (e.g., *Li et al.*, 1997).

SW cloud radiative forcing at the TOA and at the surface from this study is –46 W m^{-2} and –49 W m^{-2}. Cloud forcing over ocean is 16 W m^{-2} larger than over land. It is noted, that cloud forcing does not uniquely measure the radiative effect of clouds since it is calculated relative to the clear sky. In other words, the same cloud would have a larger effect on a dark oceanic scene than on a brighter land scene.

Acknowledgements—This work was supported by grant NAG59634 from the National Aeronautical and Space Administration (NASA) Research Division, Office of Earth Science, MDAR Code Y (*Dr. D. Anderson*, Project Manager), by grant NAG56667 from the NASA PATHFINDER Mission to Planet Earth (MTPE) Program Science Division (*Dr. J. Dodge*, Program Manager), and by grant NAG11831 from the NASA Radiation Sciences Program Office of MTPE Code YS (*Dr. R. Curran*, Project Manager). The ISCCP D1 data were obtained from the NASA Langley Research Center Atmospheric Sciences Data Center. We thank *Dr. B. Zhang* for the help with the calculations.

References

Bishop, J.K.B. and *Rossow, W.B.*, 1991: Spatial and temporal variability of global surface solar irradiance. *J. Geophys. Res. 96*, 16839-16858.

Budyko, M.I., 1974: *Climate and Life* (ed.: *D.H. Miller*). Academic Press, San Diego, California, 508 pp.

Cess, R.D., Zhang, M.H., Minnis, P., Corsetti, L., Dutton, E.G., Forgan, B.W., Garber, D.P., Gates, W.L., Hack, J.J., Harrison, E.F., Jing, X., Kiehl, J.T., Long, C.N., Morcrette, J.J.,

Potter, G.L., Ramanathan, V., Subasilar, B., Whitlock, C.H., Young, D.F., and *Zhou, Y.*, 1995: Absorption of solar-radiation by clouds - Observations versus models. *Science 267*, 496-499.

Cess, R.D., Zhang, M.G., Wang, P.H., and *Wielicki, B.A.*, 2001: Cloud structure anomalies over the tropical Pacific during the 1997/98 El Niño. *Geophys. Res. Lett. 28*, 4547-4550.

Chen J, Carlson, B.E., and *Del Genio, A.D*, 2002: Evidence for strengthening of the tropical general circulation in the 1990s. *Science 295*, 838-841.

Darnell, W.L., Staylor, W.F., Gupta, S.K., Ritchey, N.A., and *Wilber, A.C.*, 1992: Seasonal variation of surface radiation budget derived from International Satellite Cloud Climatology Project C1 data. *J. Geophys. Res. 97*, 15741-15760.

Fouquart, Y., Bonnel, B., and *Ramaswamy, V.*, 1991: Intercomparing shortwave radiation codes for climate studies. *J. Geophys. Res. 96*, 8955-8968.

Kandel, R, Viollier, M., Raberanto, P., Duvel, J.Ph., Pakhomov, L.A., Golovko, V.A., Trishchenko, A.P., Mueller, J., Raschke, E., Stuhlmann, R., and *the International ScaRaB Scientific Working Group (ISSWG)*, 1998: The ScaRaB earth radiation budget dataset. *Bull. Amer. Meteor. Soc. 79*, 765-783.

Kiehl, J.T. and *Trenberth, K.E.*, 1997: Earth's annual global mean energy budget. *Bull. Amer. Meteor. Soc. 78*, 197-208.

Konzelmann, T., Cahoon, D.R., and *Whitlock, C.H.*, 1996: Impact of biomass burning in equatorial Africa on the downward surface shortwave irradiance: Observations versus calculations. *J. Geophys. Res. 101*, 22833-22844.

Lacis, A.A. and *Hansen, J.E.*, 1974. A parameterization for the absorption of solar radiation in the earth's atmosphere. *J. Atmos. Sci. 31*, 118-132.

Laszlo, I. and *Pinker, R.T.*, 1997: Impact of changes to water vapor parameterization on surface short-wave radiative fluxes. In *IRS '96: Current Problems in Atmospheric Radiation*. A. Deepak Publishing, Hampton, Virginia, USA, 526-529.

Laszlo, I. and *Pinker, R.T.*, 1994: On the relationship between shortwave net radiative fluxes at the top of the atmosphere and at the surface. Preprints *Eighth Conference on Atmospheric Radiation*. Nashville, TN, January 23-28, 1994. Amer. Meteor. Soc., 532-533.

Laszlo, I., Pinker, R.T., and *Whitlock, C.H.*, 1997: Comparison of short-wave fluxes derived from two versions of the ISCCP products. In *IRS '96: Current Problems in Atmospheric Radiation*. A. Deepak Publishing, Hampton, Virginia, USA, 762-765.

Li, Z. and *Leighton, H.G.*, 1993: Global climatologies of solar radiation budgets at the surface and in the atmosphere from 5 years of ERBE data. *J. Geophys. Res. 98*, 4919-4930.

Li, Z., Moreau, L., and *Arking, A.*, 1997: On solar energy disposition: A perspective from observation and modeling. *Bull. Amer. Meteor. Soc. 78*, 53-70.

Major, G., 1976: Absorption of short-wave solar radiation in the atmosphere. Országos Meteorológiai Szolgálat Kisebb Kiadványai 40, Budapest, 49 pp.

Major, G., 1998: On surface-absorbed solar radiation. *Bull. Amer. Meteor. Soc. 79*, 92-93.

Major, G., Miskolczi, F., Putsay, M., Rimóczi-Paál, A., Takács, O., and *Tárkányi, Zs.*, 1981: World maps of relative global radiation. Annex to WMO Tech. Note 172. [Available from *World Meteorological Organization, C. P. 2300, Geneva 2, Switzerland.*]

Ohmura, A. and *Gilgen, H.*, 1993: Re-evaluation of the global energy balance. *Interactions between Global Climate Systems, The Legacy of Hann. Geophys. Monogr.* No. 75. Amer. Geophys. Union, 93-110.

Pinker, R.T. and *Laszlo, I.*, 1992: Modeling surface solar irradiance for satellite applications on a global scale. *J. Appl. Meteor. 31*, 194-211.

Pinker, R.T., Laszlo, I., and *Zhang, B.*, 2001: Pathfinder large scale radiative fluxes: Data availability and their use in climate research. In *IRS 2000: Current Problems in Atmospheric Radiation* (eds.: *W.L. Smith* and *Yu.M. Timofeyev*). A. Deepak Publishing, Hampton, Virginia, 481-484.

Ramaswamy, V. and *Freidenreich, S.M.*, 1992: A study of broadband parameterizations of the solar radiative interactions with water vapor and water drops. *J. Geophys. Res. 97*, 11,487-11,512.

Rossow, W.B. and *Schiffer, R.A.*, 1999: Advances in understanding clouds from ISCCP. *Bull. Amer. Meteor. Soc. 80*, 2261-2287.

Rossow, W.B. and *Zhang, Y.-C.*, 1995: Calculation of surface and top of atmosphere radiative fluxes from physical quantities based on ISCCP data sets 2. Validation and first results. *J. Geophys. Res. 100*, 1167-1197.

Schiffer, R.A and *Rossow, W.B,* 1985: ISCCP global radiance data set: A new resource for climate research. *Bull. Amer. Meteor. Soc. 66*, 1498-1505.

Stephens, G.L., 1978: Radiation profiles in extended water clouds, II. Parameterization schemes. *J. Atmos. Sci. 35*, 2123-2132.

Stephens, G.L., Ackerman, D., and *Smith, E.A.*, 1984: A shortwave parameterization revised to improve cloud absorption. *J. Atmos. Sci. 41*, 687-690.

WCP-55, 1983: World Climate Research Report of the experts meeting on aerosols and their climatic effects. Williamsburg, Virginia, 28-30 March 1983, (eds.: *A. Deepak* and *H.E. Gerber*), 107 pp.

Whitlock, C.H., Charlock, T.P., Staylor, W.F., Pinker, R.T., Laszlo, I., Ohmura, A., Gilgen, H., Konzelman, T., DiPasquale, R.C., Moats, C.D., LeCroy, S.R., and *Ritchey, N.A.*, 1995: First Global WCRP Shortwave surface Radiation Budget Data Set. *Bull. Amer. Meteor. Soc. 76*, No. 6, 1-18.

Wielicki, B.A., Wong, T., Allan, R.P., Slingo, A., Kiehl, J.T., Soden, B.J., Gordon, T., Miller, A. J., Yang, S.-K., Randall, D.A., Robertson, F., Susskind, J., and *Jacobowitz, H.*, 2002: Evidence for large decadal variability in thetropical mean radiative energy budget. *Science 295*, 841-844.

Wiscombe, W.J., 1977: The delta-Eddington approximation for a vertically inhomogeneous atmosphere. *NCAR Technical Note TN-121+STR.*

IDŐJÁRÁS

Quarterly Journal of the Hungarian Meteorological Service
Vol. 105, No. 4 — Vol. 106, No. 1, October 2001 — March 2002, pp. 207–218

Effect of the atmospheric boundary layer on the radiative fluxes

Marian Ostrožlík and **František Smolen**

Geophysical Institute of Slovak Academy of Sciences
Dúbravská cesta 9, 842 28 Bratislava, Slovak Republic
E-mail: geofostr@savba.sk

(Manuscript received September 27, 2001; in final form January 8, 2002)

Abstract—Based on the short- and long-wave radiative fluxes in the high-mountain positions Skalnaté Pleso and Stará Lesná the influence of the atmospheric boundary layer on the radiative fields in the High Tatras is studied. Besides the time and space variability of the radiative fluxes the attention to the emissivity, radiative cooling and heating in the investigated atmospheric layer as well as the influence of the low clouds on the long-wave radiation balance is paid.

Key-words: global radiation, diffuse radiation, short- and long-wave radiative fluxes, radiation balance, atmospheric emissivity, radiative cooling

1. Introduction

Present knowledge on the radiative fields distribution in the atmosphere shows that the atmospheric boundary layer plays an important role at the transfer and the transformation of the radiant energy. Its physical conditions are characterized by the large time and spatial variability which depends not as on the general and local circulation but as on the proper radiative processes which take place in the atmospheric boundary layer. An explanation of the complicated processes is possible on the basis of the theoretical knowledge on radiant energy transfer as well as from a detailed analysis of experimental data, obtained by means of the radiative fluxes measurement in the atmosphere.

Thermal energy obtained by the transformation of the short-wave radiation in the Sun-Earth-atmosphere system is a main source of energy for the meteorological processes in the lower atmospheric layers. The long-wave

radiative fluxes enable to obtain some information about transport of thermal energy in the atmospheric boundary layer. Wide range of shapes, sizes, and microphysical properties of clouds in a substantial measure influence the transformation of the radiative fluxes.

2. Data and methods

To propose to explain some regularities of the atmospheric boundary layer as well as the influence of the low clouds on the time and space variability of the short- and long-wave radiative fluxes, and the radiative processes in the atmospheric boundary layer between Stará Lesná and Skalnaté Pleso the measurements at the meteorological observatories Skalnaté Pleso (φ=49°12′N, λ=20°14′E, h=1778 m a.s.l.) and Stará Lesná (φ=49°09′N, λ=20°17′E, h=810 m a.s.l.) were used.

The vertically different position of both sites approximately 1000 m and their small horizontal distance (about 3000–4000 m) make suitable conditions to study the following properties of the atmosphere: atmospheric transmissivity, absorption ability, emissivity and radiative cooling or heating. Using of the analogical measurement technique and method at the both sites provide us the opportunity to a certain measure to eliminate mistakes which could be occurred by the quantitative evaluation of the investigated layer influence on the radiative fluxes.

3. Results and discussion

Based on the 5-year data set of continuous measurements of the radiative fluxes at the both observatories (*Ostrožlík* and *Janičkovičová,* 1992–1995) some results in the short-wave and long-wave spectral ranges are presented.

3.1 Global solar radiation – G

Vertical change of the global solar radiation we expressed by the parameter δ, which is given as a ratio of differences of the global solar radiation at Stará Lesná and Skalnaté Pleso to the global solar radiation at Skalnaté Pleso in %. Annual course of this parameter at the clear sky, overcast sky and at the average cloud conditions is presented in *Fig. 1.* Decrease of the flux density of the global solar radiation with altitude is expressed by the negative sign of the δ value.

Obtained results have shown that at the clear sky the flux density of the global solar radiation increases with altitude during the whole year up to 6% in average. The most vertical changes of the flux density occur in the months

April, May, June (approximately 9–10%). On the other side, the smallest changes of the global solar radiation are in November. In this month the flux densities are practically the same at the both localities.

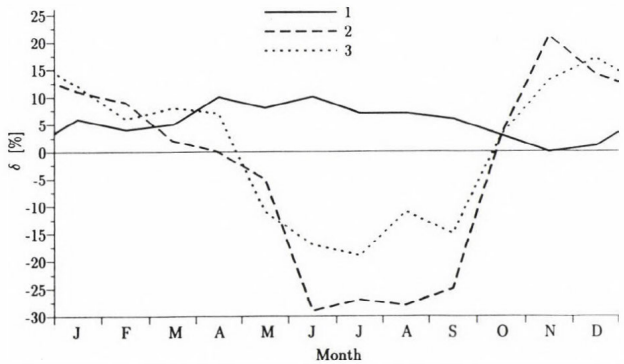

Fig. 1. Variability of the global solar radiation (δ) in the atmospheric layer between Skalnaté Pleso and Stará Lesná: 1 – clear sky, 2 – overcast sky, 3 – average conditions during the period 1991–1995.

A quite different situation of the annual course of the vertical change of the global solar radiation is at the overcast sky as well as at the average cloud conditions. In these cases in the summer months the flux density of global solar radiation is lower at Skalnaté Pleso than at Stará Lesná. It confirms that in this period of the year the cloudiness more attenuates the global solar radiation at Skalnaté Pleso than at Stará Lesná. Obtained results were compared with results of measurement in Hungary (*Major* and *Takács*, 1974), where it is stated that the growing values of global radiation are compensated by cloudiness only in summer.

3.2 Diffuse radiation – D

Fig. 2 illustrates the annual change of the diffuse radiation at Stará Lesná and at Skalnaté Pleso in dependence on cloudiness. It can be seen that at the clear sky the diffuse irradiance decreases with altitude in all months of the year. However, at the average cloud conditions it is remarkable that the diffuse irradiance in the spring months—from February to April—is higher at Skalnaté Pleso than at Stará Lesná. It means that in this part of year the diffuse irradiance increases with altitude. The mentioned anomaly in the diffuse radiation distribution is connected with the interaction of the snow cover reflectance, the

multiple reflection in a complex terrain, cloudiness, and the short-wave radiation backscattering.

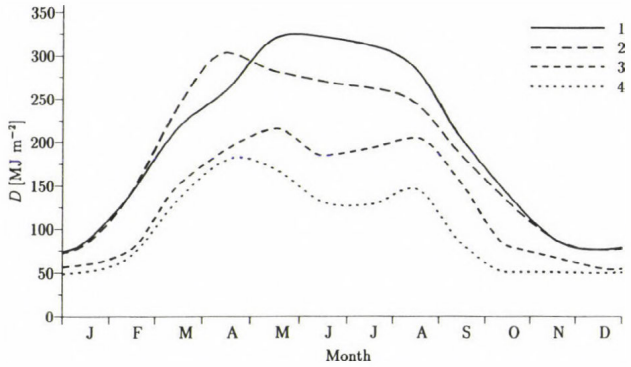

Fig. 2. Annual course of the mean monthly sums of diffuse radiation (D) at Skalnaté Pleso (2 – average conditions, 4 – clear sky) and at Stará Lesná (1 – average conditions, 3 – clear sky) during the period 1991–1995.

Effect of the atmospheric boundary layer on the short-wave radiation can be also characterized by the ratio of diffuse radiation (D) to global solar radiation (G). This ratio indirectly expresses the scattering ability of the investigated atmospheric layer. Obtained results have shown that the ratio D/G is 0.22 at Skalnaté Pleso and 0.28 at Stará Lesná in annual mean at the clear sky. Scattering ability varies greatly both in space and time depending upon the atmospheric conditions. The smallest value of the scattering occurs in February. The difference of D/G values at Skalnaté Pleso and at Stará Lesná is only 0.015. The largest scattering of this layer occurs in warming period and the corresponding difference between D/G values at both observatories is 0.122. During the day the largest scattering falls on 4 till 5 hours and on the other side the lowliest scattering occurs as a rule at noon or at the afternoon hours. A low scattering of the considered atmospheric layer in February shows on the low turbidity in the atmospheric boundary layer. The small values of Linke's turbidity factor (T_p) also confirm this fact. Mean value of T_p is 1.75 in February in the layer Skalnaté Pleso and Stará Lesná (*Smolen,* 1961).

We must emphasize that in the high-mountain positions the values of diffuse radiation are in a great measure influenced by the backscattering and the multiple reflection of the short-wave radiation in the atmosphere (*Möller,* 1965; *Smolen* and *Ostrožlík,* 1998a). A numerical comparison of the calculated data of the intensification factor (G_r/G_0) or (D_r/D_0) with the backscattering coefficient (d) shows that while in the highest positions of the mountain massif

the diffuse radiation flux density is influenced by the backscattering and multiple reflectance, the reason of short-wave radiation flux density increase in the lower positions is mainly the backscattering (G_r and D_r are the global and diffuse radiation at the high albedo of snow cover, G_0 and D_0 are the global and diffuse radiation in July at the same Sun's elevation as the G_r and D_r). The mentioned factors will influence not as the short-wave radiation balance (B_K) but as the total radiation balance (B) in the final consequence.

3.3 Short-wave radiation balance – B_K

More detailed analysis of the B_K values has shown that in case of the clear sky to the more expressive vertical change of B_K value comes as it exists at the mean cloud conditions. Its value in a great measure depends on the seasonal period (*Pjatkovskaja,* 1975). The difference between the short-wave radiation balance at Skalnaté Pleso and Stará Lesná (ΔB_K) enables to determine the magnitude of the radiative flux divergence in the atmospheric boundary layer. We must emphasize, that the ΔB_K value in a great measure depends on the vertical change of the reflecting ability of the active surface. Functional dependence of the short-wave radiation balance differences ΔB_K on the corresponding differences of surface albedo ΔA in the short-wave spectral range can be expressed by polynomial of degree 3 (*Fig. 3*).

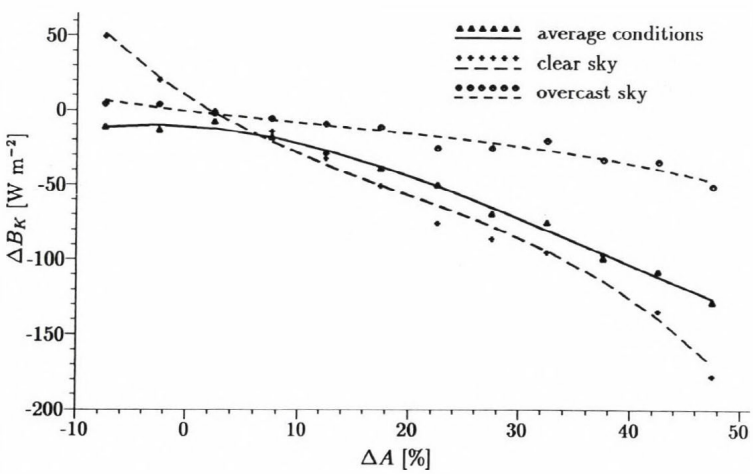

Fig. 3. Dependence of the short-wave radiative flux differences (ΔB_K) upon the differences of surface albedo (ΔA) in the atmospheric layer between Skalnaté Pleso and Stará Lesná during the 1991–1995 period.

Some another results about the time variability of the radiative receipt or radiative loss of heat in a consequence of the interaction of the short-wave radiation fluxes in the layer between Skalnaté Pleso and Stará Lesná in case of clear sky, low clouds as well as average cloud conditions are presented in the paper of authors *Smolen* and *Ostrožlík* (1999a).

3.4 Long-wave radiation balance – L^*

The loss of thermal energy by active surface was expressed by means of long-wave radiation balance. It was shown that the loss of thermal energy increases with altitude in the investigated layer. It is especially remarked at the clear sky (*Smolen et al.*, 1996). The measure of the long-wave radiation balance decrease with altitude enables the vertical gradient of long-wave radiation balance γ_{L^*}. Daily course of the γ_{L^*} value at the overcast sky as well as at the clear sky are illustrated in *Fig. 4*. We can see an analogous course of the γ_{L^*} in both cases. The mean values of vertical gradient γ_{L^*} are substantially higher at the clear sky than at the overcast sky. We can also observe a sudden decrease of the γ_{L^*} value after 15 h. This is especially marked in case of overcast sky. In this case γ_{L^*} values obtain a negative sign in a time interval of 18 to 20 h. It means that L^* values are higher at Skalnaté Pleso than at Stará Lesná.

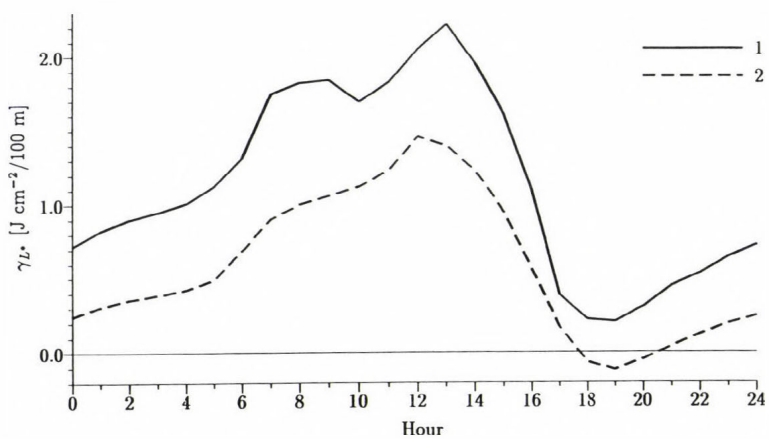

Fig. 4. Daily course of the long-wave radiation balance vertical gradient (γ_{L^*}) in the layer between Skalnaté Pleso and Stará Lesná during the 1991–1995 period (1 – overcast sky, 2 – clear sky).

3.5 Total radiation balance – B

Measurements of the short- and long-wave radiative fluxes at Skalnaté Pleso and Stará Lesná enabled to study the total radiation balance in the atmospheric boundary layer as well as its change with altitude. Time variability of the total radiation balance at the levels Skalnaté Pleso and Stará Lesná are illustrated in *Fig. 5*. Based on the 5-year measurement data it was shown that while the annual mean of radiation balance at Skalnaté Pleso is only 6.941 J cm^{-2}, the corresponding value at Stará Lesná represents up 21.124 J cm^{-2}. It can be seen that radiation balance decreases with altitude in the investigated layer. This fact is remarkable during the day.

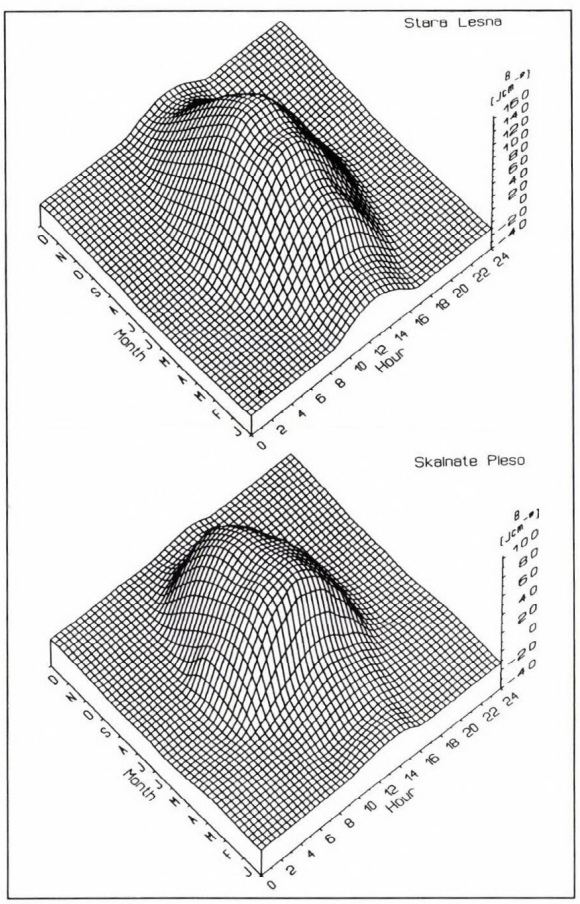

Fig. 5. Time variability of the total radiation balance at Skalnaté Pleso and at Stará Lesná at the average cloud conditions during the 1991–1995 period.

The vertical gradient of radiation balance (γ_B) served a measure of radiation balance decreasing in the layer between Skalnaté Pleso and Stará Lesná. Daily course of this gradient is demonstrated in *Fig. 6*. From the course of the curves we can see that γ_B has a pronounced daily course with maximum at noon. The most intensive decrease of radiation balance with altitude occurs in spring months. This expressive decrease of radiation balance with increasing altitude is due to the large reflecting ability of the active surface in the higher mountain localities.

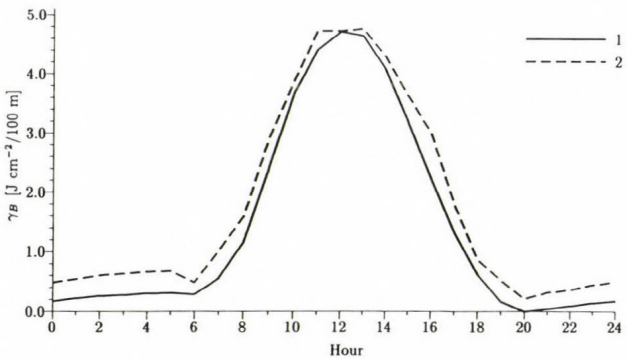

Fig. 6. Daily course of the radiation balance vertical gradient (γ_B) in the layer between Skalnaté Pleso and Stará Lesná during the 1991–1995 period (1 – average conditions, 2 – clear sky).

3.6 Atmospheric emissivity – ε_a

Daily course of the total atmospheric emissivity is presented in *Fig. 7* at the clear sky. From the comparison of the individual curves we receive that the total atmospheric emissivity at Skalnaté Pleso is characterized by the higher daily amplitude than Stará Lesná. There is a question, what is the reason which causes such daily course of the total atmospheric emissivity? It is known that the atmospheric emissivity is directly dependent on optical depths of absorbing gases as well as on their temperature. The different daily course of total atmospheric emissivity at Skalnaté Pleso than at Stará Lesná will be probably caused by vertical change of the water vapour content.

In general, the atmospheric emissivity decreases with the altitude. This decrease at the clear sky in the investigated layer represents in average by 15% and depends on the vertical change of the water vapor content, and CO_2 as well as on the air temperature (*Smolen* and *Ostrožlík,* 2001). In spite of fact

that *Staley* and *Jurica* (1970) have shown on the smaller variability of the water vapor emissivity with temperature change, surely we must take into attention the air temperature change with altitude at the study of total atmospheric emissivity.

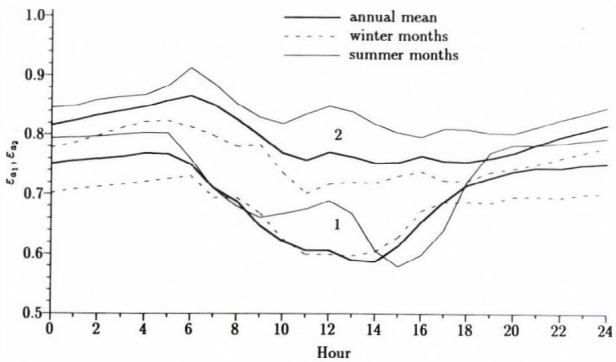

Fig. 7. Daily course of total atmospheric emissivity (ε_a) at Skalnaté Pleso (1) and at Stará Lesná (2) at the clear sky during the 1991–1995 period.

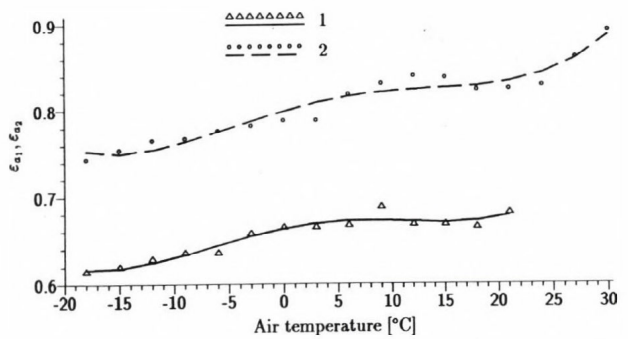

Fig. 8. Dependence of total atmospheric emissivity ($\varepsilon_{a_1}, \varepsilon_{a_2}$) on air temperature at Skalnaté Pleso (1) and at Stará Lesná (2) during the 1991–1995 period.

Fig. 8 demonstrates the dependence of total atmospheric emissivity on air temperature at the levels for the cases, when the optical depth of precipitated water vapor above these levels is from 0.300 to 2.500 g cm^{-2}. Such values correspond the mean meteorological conditions in the high-mountain regions. It is remarkable that the atmospheric emissivity at the clear sky at Skalnaté Pleso as well as at Stará Lesná slowly rises with the increasing air temperature. This

dependence of atmospheric emissivity on air temperature can be expressed with a relatively good accuracy by the polynomial function of 4. degree.

3.7 Radiative cooling and heating rate – $(\delta T / \delta t)_{\Delta F}$

Study of the relationships between the radiative temperature fluxes $(\delta T / \delta t)_{\Delta F}$ and the cloudiness in the atmospheric layer between Stará Lesná and Skalnaté Pleso has shown that the cloud cover decreases the radiative cooling rate. According to experimental data, the mean annual values of the radiative cooling rate are: at the average cloud conditions 0.070 K h^{-1}, at the clear sky 0.1218 K h^{-1}, and at the overcast sky 0.012 K h^{-1}. The most intensive radiative cooling rate is in December at the clear sky, and the mean value of $(\delta T / \delta t)_{\Delta F}$ is 0.171 K h^{-1}. On the other side the smallest values of the radiative cooling rate are in August. A some decrease of the radiative cooling rate in August can be probably caused by the development of the convective clouds in the highland regions during the day.

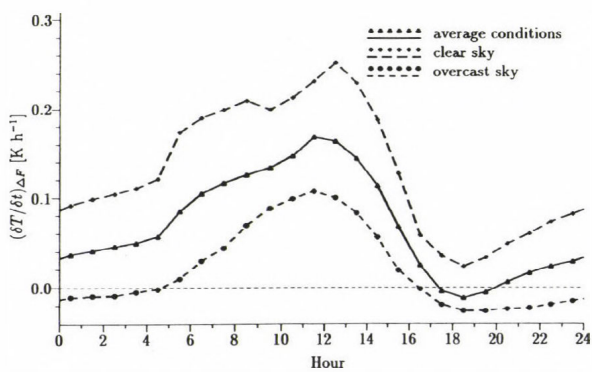

Fig. 9. Daily course of the radiative cooling rate $(\delta T / \delta t)_{\Delta F}$ in the layer between Skalnaté Pleso and Stará Lesná during the 1991–1995 period.

Fig. 9 presents daily variations of the radiative cooling rate in the investigated atmospheric layer in dependence on cloudiness. It can be seen that the daily course of the radiative cooling or heating rate has a pronounced daily course with midday maximum. The most intensive radiative cooling rate at noon occurs as a result of the mutual interaction of the long-wave radiative fluxes. In this part of day the mean values of $(\delta T / \delta t)_{\Delta F}$ is 0.228 K h^{-1}. The sudden change of radiative cooling rate occurs in the later afternoon hours. In evening hours after the sunset the radiative heating occurs (values have a

negative sign). Such radiative heating in the evening hours is especially pronounced at the overcast sky conditions.

Increasing of the low cloud amount very expressively contributes to the decrease of the radiative cooling rate. Separation of the atmospheric layer between Stará Lesná and Skalnaté Pleso to three sublayers by the low clouds has shown, that the most intensive radiative cooling exists in the sublayer over the clouds. The values of $(\delta T / \delta t)_{\Delta F}$ at the certain meteorological conditions can reach up to 1.591 K h^{-1}. A relatively small radiative cooling rate is observed in the cloudy sublayer, and below its. The radiative heating of the atmosphere very often occurs in the sublayer below the clouds. The values of the radiative heating rate can be up to -0.042 K h^{-1} and depend in a substantial measure from the low cloud extent. More detailed analysis of the radiative air temperature changes in the atmospheric boundary layer between Skalnaté Pleso and Stará Lesná is made in the papers *Smolen* and *Ostrožlík* (1998b, 1999b).

4. Conclusions

Evaluation of the experimental data of the short- and long-wave radiative fluxes in the atmospheric layer between Stará Lesná and Skalnaté Pleso has shown:

- investigated atmospheric layer attenuates of the global solar radiation flux density up to 6% but at the clear sky the flux density of the global solar radiation increases with altitude by 6% in average,
- while at Skalnaté Pleso the global solar radiation and diffuse irradiation are influenced by the backscattering and multiple reflectance, at Stará Lesná it is caused mainly by the backscattering,
- short-wave radiation balance depends in a great measure on vertical change of the reflecting ability of the active surface,
- the annual mean of the total radiation balance at Stará Lesná is 21.12 J cm^{-2} while at Skalnaté Pleso represents only 6.94 J cm^{-2},
- the atmospheric emissivity usually decreases with altitude and manifests the expressive time variability. This decrease represents 15% at the clear sky in the mentioned layer,
- emitted ability of atmosphere considerably varies during the year and the smallest values reaches in February,
- cloud cover in the atmospheric layer between Stará Lesná and Skalnaté Pleso decreases the radiative cooling rate. The mean values of the radiative cooling rate are: 0.070 at the average cloud conditions, 0.1218 K h^{-1} at the clear sky, and 0.012 K h^{-1} at the overcast sky.

Acknowledgement—The authors are grateful to the Grant Agency for Science (Grants No. 2/6041/01, 2/2093/22) for partially supporting this work.

References

Major, G. and *Takács, O.*, 1974: Change of sunshine duration and annual global radiation with altitude on the basis of data measured in Hungary (in Hungarian). *Időjárás 78*, 281-287.

Möller, F., 1965: On the backscattering of global radiation by the sky. *Tellus 17*, 350-355.

Ostrožlík, M. and *Janičkovičová, Ľ.* (eds.), 1992–1995: *Results of Meteorological Measurements at the Observatories of the Geophysical Institute of the Slovak Academy of Sciences*. Geophysical Institute of SAS, Bratislava, 33.

Pjatkovskaja, N. P., 1975: Radiation balance and short-wave radiative heat flux in the different climatic regions. *Trudy GGO, 276*, 43-61.

Smolen, F., 1961: Atmospheric turbidity conditions in Carpathian region of Slovakia based on actinometric measurements (in Slovak). In *Príspevok k meteorológii Karpát. Vydavateľstvo Slov. akadémie vied*. Bratislava, 67-78.

Smolen, F. and *Ostrožlík, M.*, 1998a: Effect of albedo, atmospheric turbidity and cloudiness on the diffuse radiation in the high-mountain positions. *Contr. Geophys. Inst. SAS, Ser. Meteorol. 18*, 4-18.

Smolen, F. and *Ostrožlík, M.*, 1998b: Radiative cooling rate in the atmospheric boundary layer. *Időjárás 102*, 247-257.

Smolen, F. and *Ostrožlík, M.*, 1999a: Short-wave radiation balance and its vertical change in the atmospheric boundary layer in high-mountain conditions. *Meteorol. čas. 2*, 5-9.

Smolen, F. and *Ostrožlík, M.*, 1999b: Effect of clouds on the radiative temperature changes in the atmospheric boundary layer in the high-mountain conditions. *Contr. Geophys. Inst. SAS, Ser. Meteorol. 19*, 9-21.

Smolen, F. and *Ostrožlík, M.*, 2001: Emissivity of the atmospheric boundary layer in the high-mountain conditions. *Contrib. Geophys. and Geodesy. 30,* 495-508.

Smolen, F., Ostrožlík, M., and *Žák, B.*, 1996: Long-wave radiation fluxes in 200 m thick surface layer of atmosphere – the international experiment BOHUNICE ´89. *Contrib. Geophys. Inst. SAS, Ser. Meteorol. 16*, 7-16.

Staley, D. O. and *Jurica, G. M.*, 1970: Flux emissivity tables for water vapor, carbon dioxide and ozone. *J. Applied Meteorol. 9*, 365-372.

IDŐJÁRÁS

Quarterly Journal of the Hungarian Meteorological Service
Vol. 105, No. 4 — Vol. 106, No. 1, October 2001 — March 2002, pp. 219 - 230

A comparison between measured and calculated values of atmospheric long-wave radiation

Klaus Behrens[1] and **Klaus Gericke**

Deutscher Wetterdienst, Meteorologisches Observatorium Potsdam,
Pf. 60 06 52, D-14405 Potsdam, Germany
E-mails: klaus.behrens@dwd.de; klaus.gericke@dwd.de

(Manuscript received December 3, 2001; in final form January 30, 2002)

Abstract—In the past 10 years an enormous progress was made in measuring long-wave radiation. In this study the measurements of atmospheric long-wave radiation, which have been carried out with different types of pyrgeometers at the German BSRN station at Lindenberg since October 1994, are compared with model calculations by LOWTRAN 7 at clear sky. It was found that since November 1996, the measurements have been matched the calculated values. Comparison of measured and modeled values is a good method to check the data quality.

Key-words: atmospheric long-wave radiation

1. Introduction

In the past 10 years an enormous progress was made in measuring long-wave radiation. The initial impulse came from the World Climate Research Program (WCRP), which initiated the Baseline Surface Radiation Network (BSRN) with goals which could only reached by improvements of the instruments and corresponding calibration methods (*Ohmura et al.*, 1998).

Especially by investigations and developments, which were done at World Radiation Center (WRC) Physikalisch Meteorologisches Observatorium at Davos (PMOD) (Switzerland) with the characterization of pyrgeometers (*Philipona et al.*, 1995) and within the framework of the BSRN with the round-robin calibration experiment (*Philipona et al.*, 1998), important steps were gone. In recent time these efforts continued by the development of a sky-

[1] Corresponding author

scanning radiometer for absolute measurements of atmospheric long-wave radiation (*Philipona,* 2001) and an International Pyrgeometer and Absolute Sky-scanning Radiometer Comparison (IPASRC-I and II) (*Philipona et al.*, 2001).

Since October 1994, at the German BSRN-Station the Meteorological Observatory at Lindenberg, measurements of atmospheric long-wave radiation have been carried out with the Precision Infrared Radiometer (PIR) pyrgeometer, developed by the Eppley Laboratory Inc. (USA), used different instruments and distinguished calculation formulas as well as with CG4 pyrgeometers, developed by Kipp & Zonen (Netherlands).

The goal of this investigation is to discuss the comparability of the atmospheric downward radiation measured and calculated both with different types of pyrgeometers and distinguished formulas within the previous seven years. Therefore, these measurements are compared with an independent method using the LOWTRAN 7 radiation code.

2. Instruments and data

The atmospheric long-wave radiation measured at Lindenberg is influenced by the above mentioned improvements. *Fig. 1* shows that downward long-wave radiation was measured by four different PIRs and two different CG4s partly in parallel during the past seven years between October 1994 and November 2001.

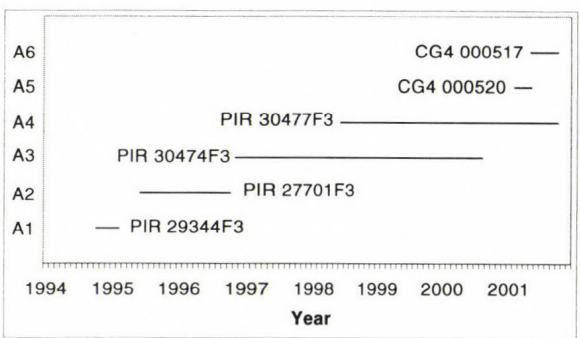

Fig. 1. Pyrgeometers used at the different periods (Ai) to measure atmospheric long-wave radiation at the BSRN station at Lindenberg (Germany).

Type and number of the pyrgeometers as well as the corresponding periods they were used are arranged in *Table 1*. Furthermore, because of a steadily improving knowledge about the PIRs, atmospheric long-wave radiation was

calculated by distinguished formulas, which are supplemented in an additional column together with those formulas applied to the CG4. All PIRs were shaded by a disc to prevent a heating of the dome by direct solar radiation. Additionally, during the first two measuring periods the remaining diffuse solar radiation, measured by CM 21 pyranometer, which was also shaded by a disc, was taken into account in Eq. (1) for correcting the downward long-wave radiation. Furthermore, the dome temperature of the PIRs was also measured because it was needed in the Eqs. (1) to (3) introduced in the formulas by *Albrecht et al.* (1974) and later by *Philipona et al.* (1995). These correction steps were applied to improve the determination of the atmospheric long-wave radiation, because of the known effects of the large dome absorptance of the PIRs (*Albrecht et al.*, 1974, *Enz et al.*, 1975).

Table 1. Pyrgeometers and measurement periods as well as the corresponding formulas for calculating atmospheric long-wave irradiance A

Pyrgeometer	Period	Formula	
PIR 29344 F3	01.10.1994–01.03.1995	$A1 = \frac{U}{C} + \sigma T_b^4 - 4\sigma (T_d^4 - T_b^4) - 0.026D$	(1)
PIR 27701 F3	14.06.1995–15.11.1996	$A2 = \frac{U}{C} + \sigma T_b^4 - 4\sigma (T_d^4 - T_b^4) - 0.026D$	(1)
PIR 30474 F3	15.11.1996–22.08.2000	$A3 = \frac{U}{C} + \sigma T_b^4 - 3\sigma (T_d^4 - T_b^4)$	(2)
PIR 30477 F3	16.06.1998–31.10.2001	$A4 = \frac{U}{C}(1 + k_1 \sigma T_b^3) + k_2 \sigma T_b^4 - k_3 \sigma (T_d^4 - T_b^4)$	(3)
CG4 000520	15.02.2001–08.05.2001	$A5 = \frac{U}{C} + \sigma T_b^4$	(4)
CG4 000517	08.05.2001–31.10.2001	$A6 = \frac{U}{C} + \sigma T_b^4$	(4)

A: atmospheric long-wave irradiance; the figures after "A" sign the period/instrument
U: voltage of the thermopile
C: sensitivity of the pyrgeometer
σ: Stefan-Boltzmann-constant
T: absolute temperature of the pyrgeometer
b: body
d: dome
k: correction factor
D: diffuse solar radiation

Because of the different construction, the measurement of the dome temperature is not necessary used in the CG4 for the determination of downwelling long-wave radiation. All pyrgeometers were ventilated with an air stream blowing around the pyrgeometer body and the dome.

The pyrgeometers used during the first two periods were calibrated with a black body at the Meteorological Observatory at Potsdam (MOP). The calibration factor of PIR 30474 F3 was derived comparing this instrument outdoors with MOP's reference pyrgeometer (PIR 30475 F3), which was calibrated at WRC PMO Davos. Also PIR 30477 F3 was calibrated at WRC Davos. The calibration factor of the CG4s were checked outdoors in comparison with the reference of the MOP with the result that no change of the factors was necessary.

Model calculation using LOWTRAN 7 (*Kneizys et al.,* 1988) are chosen to achieve the described goal. Profiles of height, pressure, temperature and relative humidity sampled by the radiosonde of the Lindenberg station are used as special input data of the model. LOWTRAN 7 restricts the number of atmospheric levels to be inserted of 34. This number of levels was distributed between the ground and 100 hPa which is the last level with information about relative humidity in a routine sounding. The input data were used at the 15 standard isobaric levels up to 100 hPa supplemented by significant levels mainly in the range up to 500 hPa. A higher resolution of the atmospheric profiles in the lower atmosphere is important because most information about long-wave downward radiation is generated in the first hectometers of the atmosphere (*Ohmura,* 2001). This fact is also important for the decision about the averaging time of the radiation measurements by the pyrgeometer comparing with calculated values by the model.

A balloon bearing the radiosonde is rising with a rate of ascent of between 5 and 8 m s^{-1} (*WMO,* 1996). This means that in 15 minutes the radiosonde reaches a level of about 500 hPa and consequently the layer emitting the biggest share of the atmospheric long-wave radiation to the ground is explored. An extension of the averaging time up to 75 minutes, those time the radiosonde reaches the summit, does not bring more and better information but it will smooth the measured downwelling radiation.

Because every model reflects only a certain part of the reality, the investigations were concentrated on the only "simple" but well defined case of a cloudless sky. Furthermore, such selected homogeneous data make it easier to detect differences between the pyrgeometers. A clear sky was determined by the means of the hourly synoptic observations at the weather station. These conditions had to be fulfilled during the flight of the radiosonde that means at the main hours of observation and one hour before. At Lindenberg radiosondes are launched daily at 00, 06, 12 and 18 UTC. Therefore the measured data of atmospheric long-wave radiation are compared only with the calculated values by the model at these fixed times.

At BSRN Stations average, standard deviation as well as minimum and maximum values of the measured irradiance of all radiation quantities including the here investigated atmospheric long-wave radiation are calculated and

recorded every minute for the last 60 seconds. As discussed above, on the base of these measured data mean value (Am), standard deviation, minimum and maximum were calculated over a time-span of 15 minutes beginning with the time of launching the radiosonde. These 15-minute-averages are going to be compared with the values received by the corresponding LOWTRAN 7 calculations (Ac). In every case a ratio Am/Ac was calculated.

Table 2 gives overview about the number of measured values in the case of a cloudless sky. Related to the total more than 50% of the cases occurred at 00 UTC in the night.

Table 2. Number of the investigated cases at the different periods and the main hours of observation

	A1	A2	A3	A4	A5	A6	Total
00 UTC	32	136	187	186	29	17	587
06 UTC	16	71	87	73	3	13	263
12 UTC	7	33	34	24	0	2	100
18 UTC	10	41	44	46	3	6	150
Total	65	281	352	329	35	38	1100

3. Results

The comparison of the measured atmospheric long-wave radiation Am with the corresponding calculated values Ac by the LOWTRAN 7 model at 00 UTC is presented as an example at scatter diagrams in *Figs. 2a–f.* The short periods A1 and A6 cover only the cold and the warm season, respectively. Therefore, the plotted values in Figs. 2a and f are concentrated at the lower and the upper part of the range related to the corresponding sky temperatures, while the data of the other periods cover the full range.

The pictures of the first two periods (Figs. 2a and b) show a bias between measured and calculated values, because all crosses are remarkably clear about the line signing the equality of Am and Ac. In both cases the measurements are about 4% higher than the calculations. The comparisons made later on (Figs. 2c–f) show a good correspondence between measurements and calculations. The mean ratios Am/Ac are only slightly higher than 1.

Table 3 gives an overview about the mean ratios Am/Ac as well as the standard deviations in different periods and at the different times of observations in detail. During the first two periods, the ratios between measured and calculated values Am/Ac are about 1.04 with exception of 12 UTC in the second period, e.g., measurements and calculations are significantly different. As it is visible in Figs. 2c–f, ratios are close to 1 during all other periods for all

instruments. The measurements with the PIR 30474 F3 (period A3) are fitting best the modeled values. It seems that the downward long-wave radiation values measured by the CG4 are slightly higher than those measured in parallel by the PIRs and the calculated values. Because of the very small number of measurements made with the CG4 (see Table 2), clear sky did not occur at 12 UTC in period A5, and these facts should be considered as preliminary and not overrated. Furthermore, the comparison of night-time and daytime values shows no significant difference during all periods with exception of A2. This is a result of the permanent shading of the PIR's dome, because the solar radiation could not heat the dome.

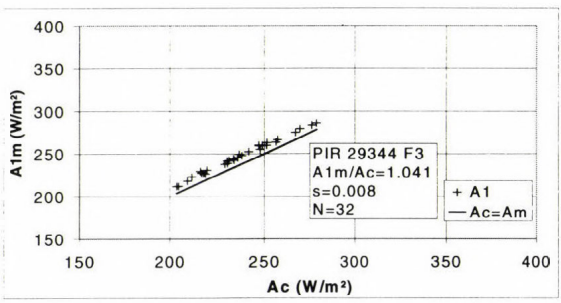

(a)

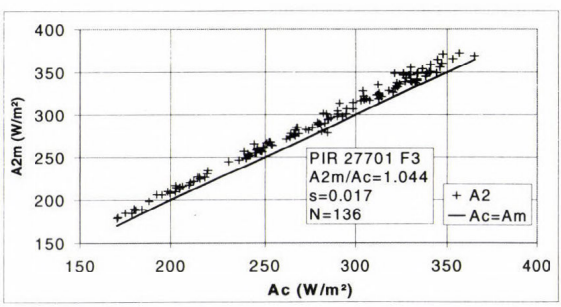

(b)

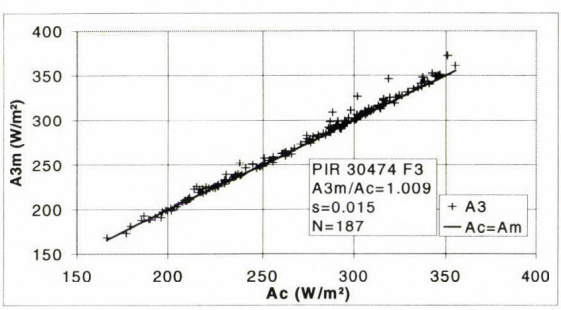

(c)

→ →

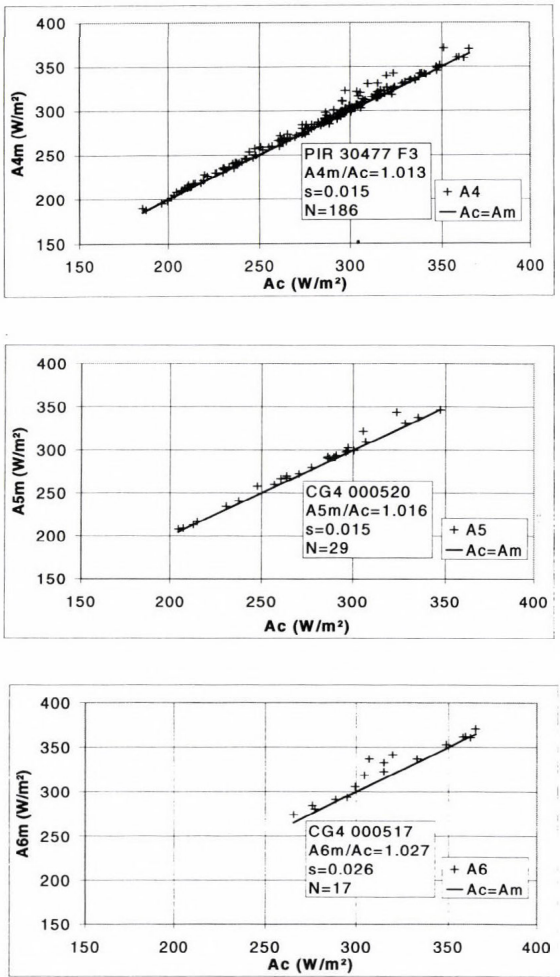

Fig. 2a–f. Comparisons of calculated irradiances of atmospheric long-wave radiation (Ac) by LOWTRAN 7 with measured irradiances (Am) in different periods as well as with different pyrgeometers. In the box are given mean ratio (Am/Ac), standard deviation (s) and number of measurements (N) at 00 UTC at Lindenberg, Germany.

Time series of the ratios between the measured and calculated values Am/Ac at the four main hours of observation are given in *Figs. 3a–d.* The large deviations in the two first periods, already have been discussed, also attract attention in these pictures. The good correspondence of measured and calculated values at 12 UTC during the period A2 can not be explained up to now, especially because no changes in the measurements were documented.

The ratios at 00 UTC (Fig. 3a) seem to follow a yearly course. Therefore, the mean ratios are calculated for every period divided into winter and summer. Summer includes the months from April to September, while the remaining months are assigned to the winter. *Table 4* shows the results, which are similar to those of Table 3. The winter and summer ratios are close together. Standard deviations of these averages have the same magnitude as given in Table 2, which means that they are from the same population. Winter and summer ratios do not significantly differ. In some cases, e.g., in periods A5 and A6 at 06 UTC, the mean ratios have a small difference. This is caused by the small number of cases of these samples. They should be excluded from the assessment.

Table 3. Mean ratios Am/Ac and their standard deviations at the different periods and the main hours of observation

	Period	**A1**	**A2**	**A3**	**A4**	**A5**	**A6**
00 UTC	Mean (Am/Ac)	1.041	1.044	1.009	1.013	1.016	1.027
	Stdev	*0.008*	*0.017*	*0.015*	*0.015*	*0.015*	*0.026*
06 UTC	Mean (Am/Ac)	1.039	1.040	1.007	1.008	1.014	1.011
	Stdev	*0.010*	*0.018*	*0.011*	*0.010*	*0.021*	*0.010*
12 UTC	Mean (Am/Ac)	1.038	0.998	1.005	1.014	-	1.025
	Stdev	*0.007*	*0.022*	*0.011*	*0.014*	-	*0.016*
18UTC	Mean (Am/Ac)	1.040	1.043	1.005	1.014	1.021	1.015
	Stdev	*0.007*	*0.015*	*0.012*	*0.014*	*0.019*	*0.008*

Table 4. Mean ratios Am/Ac at the different periods and the main hours of observation separated for winter and summer season

	Season	**A1**	**A2**	**A3**	**A4**	**A5**	**A6**
00 UTC	Winter	1.041	1.046	1.005	1.010	1.008	1.036
	Summer	1.038	1.042	1.012	1.014	1.017	1.020
06 UTC	Winter	1.039	1.046	1.005	1.007	1.001	1.028
	Summer	1.042	1.032	1.008	1.008	1.042	1.008
12 UTC	Winter	1.038	0.997	1.004	1.008	-	1.025
	Summer	-	0.999	1.007	1.018	-	-
18 UTC	Winter	1.040	1.044	1.002	1.011	1.004	1.019
	Summer	-	1.040	1.012	1.016	1.029	1.013

Time series of the ratios Am/Ac (Figs. 3a–d) show also a number of outliers (about 5%) at every series, if an outlier is defined as a value which is outside of the range of mean ±2*standard deviation. Investigations have shown that the outliers are related to standard deviations of Am, which are larger than in the normal case. One possible reason may be that these selected cloudless cases based on hourly synoptic observations were disturbed (no really clear cases) during the averaging time of the fundamental data. *Dutton (1993)* mentioned similar results and explained it by atmospheric variability and inhomogeneity as well as LOWTRAN 7 input variations. In these cases the given model conditions of a clear sky did not match the observed state of the atmosphere reflected by the measurements of the pyrgeometer. The recalculation of the ratios Am/Ac and the corresponding averages, after cancelling the outliers, led only to marginal changes of the means and smaller standard deviations as one could expect, because of the normal distribution of the ratios.

Fig. 4 shows a relative frequency distribution of the differences Am-Ac after cancelling the outliers at 00 UTC for the periods A3 and A4, the periods with the largest number of observations. Nearly 30% of the data during the A3 period between ±1 W m^{-2} and about 60% lies within ±3 W m^{-2}. The differences of A4 are slightly moved to higher values. The most frequent number of values (about 38%) are observed between 1 and 3 W m^{-2}. This underlines the very good agreement between measured and calculated atmospheric long-wave radiation after November 1996.

4. Conclusions

- This study showed that the comparison of atmospheric long-wave radiation measured by different types of pyrgeometers at different periods with independent calculations by means of a model, in this case LOWTRAN 7, is a good method to check the data quality under well defined conditions.
- The atmospheric long-wave radiation measured during the first two periods at a cloudless sky is about 4% too high and has to be corrected. Furthermore, a similar investigation is necessary to study this quantity at a totally covered sky including different types of clouds and to get further information in the case of broken clouds. Finally, on the base of this information a decision has to be made about the usage of one or more correction factors related to the clear or cloudy sky.
- The measurements carried out with PIRs or related to a PIR calibrated at the WRC PMO at Davos as well as with the CG4s are close to the independent calculations of LOWTRAN 7 at a clear sky.

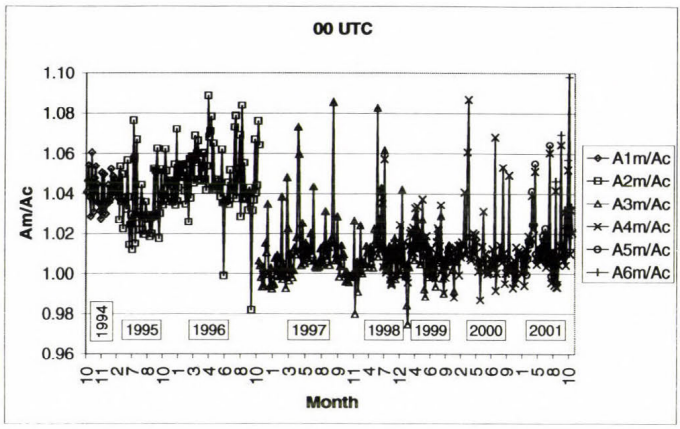
00 UTC
Am/Ac
1.10
1.08
1.06
1.04
1.02
1.00
0.98
0.96
A1m/Ac
A2m/Ac
A3m/Ac
A4m/Ac
A5m/Ac
A6m/Ac
1994
1995
1996
1997
1998
1999
2000
2001
Month

(a)

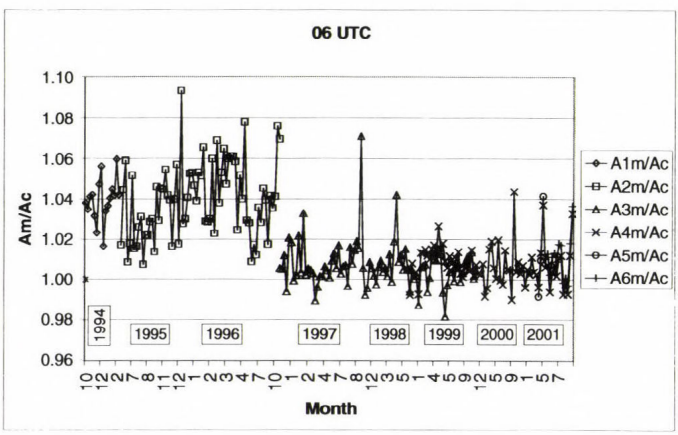
06 UTC
Am/Ac
1.10
1.08
1.06
1.04
1.02
1.00
0.98
0.96
A1m/Ac
A2m/Ac
A3m/Ac
A4m/Ac
A5m/Ac
A6m/Ac
1994
1995
1996
1997
1998
1999
2000
2001
Month

(b)

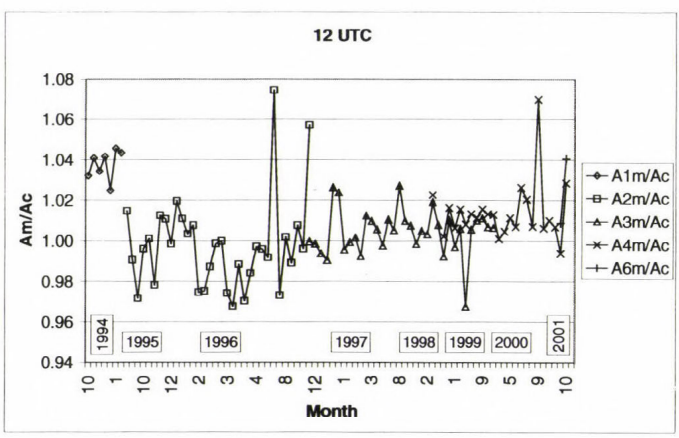
12 UTC
Am/Ac
1.08
1.06
1.04
1.02
1.00
0.98
0.96
0.94
A1m/Ac
A2m/Ac
A3m/Ac
A4m/Ac
A6m/Ac
1994
1995
1996
1997
1998
1999
2000
2001
Month

(c)

→ →

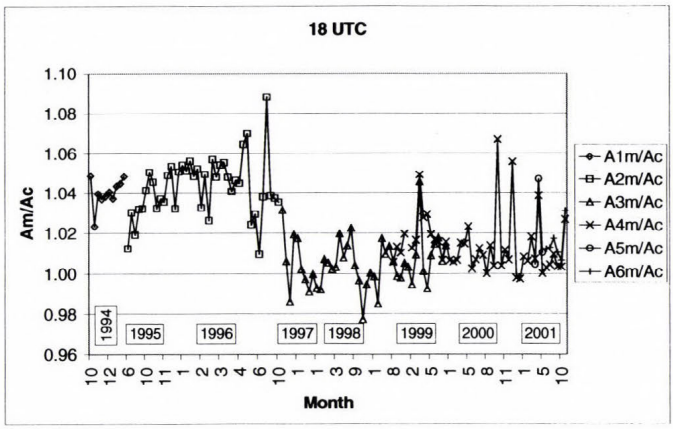

Fig. 3a–d. Ratios of measured (Am) and calculated (Ac) values by LOWTRAN 7 of atmospheric long-wave radiation at Lindenberg, Germany.

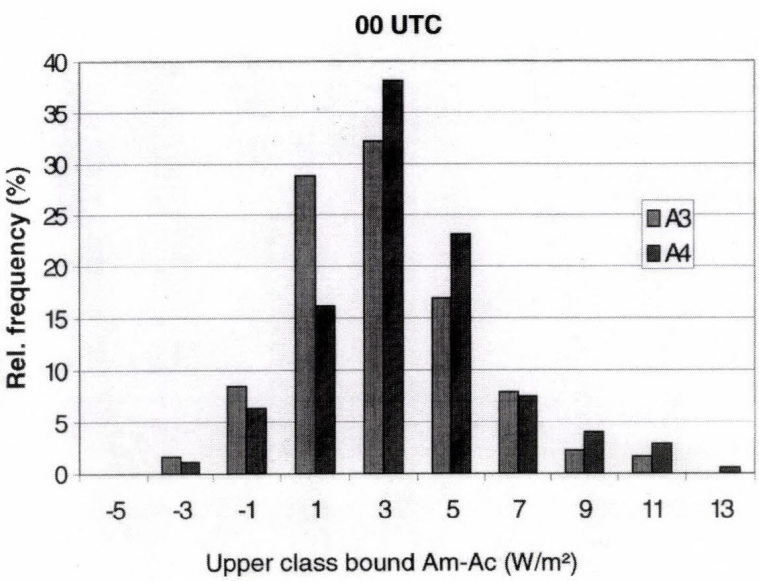

Fig. 4. Relative frequency distribution of the differences between measured (Am) and calculated (Ac) irradiances of atmospheric long-wave radiation during the periods A3 and A4, after removing outliers at 00 UTC, at Lindenberg, Germany.

References

Albrecht, B., Peollet, M., and *Cox, S. K.*, 1974: Pyrgeometer measurements from aircraft. *Rev. Sci. Instrum. 45,* 33-38.

Dutton, E. G., 1993: An extended comparison between LOWTRAN 7 computed and observed broadband thermal irradiances: Global extreme and intermediate surface conditions. *J. Atmos. Oceanic Technol. 10,* 326-336.

Enz, J. W., Klink, J. C., and *Baker, D. G.*, 1975: Solar radiation effects on pyrgeometer performance. *J. Appl. Meteor. 14,* 1297-1302.

Kneizys, F. X., Shettle, E. P., Abreu, L. W., Chetwynd, J. H., Anderson, G. P., Gallery, W. O., Selby, J. E. A., and *Clough, S. A.*, 1988: Users guide to LOWTRAN 7, AFGL-TR-88-0177. Air Force Geophysics Laboratory, Hanscom AFB, MA 01731, USA, 137p.

Ohmura, A., 2001: Physical basis for temperature-based melt-index method. *J. Appl. Meteor. 40,* 753-761.

Ohmura, A., Dutton, E. G., Forgan, B., Fröhlich, C., Gilgen, H., Hegner, H., Heimo, A., König-Langlo, G., McArthur, B., Müller, G., Philipona, R., Pinker, R., Whitlock, C. H., Dehne, K., and *Wild, M.*, 1998: Baseline Surface Radiation Network (BSRN/WCRP): New precision radiometry for climate research. *Bull. Amer. Meteor. Soc. 79,* 2115-2136.

Philipona, R., 2001: Sky-scanning radiometer for absolute measurements of atmospheric longwave radiation. *Appl. Opt. 40,* 2376-2383.

Philipona, R., Fröhlich, C., and *Betz, C.*, 1995: Characterization of pyrgeometers and the accuracy of atmospheric longwave radiation measurements. *Appl. Opt. 34,* 1598-1605.

Philipona, R., Fröhlich, C., Dehne, K., DeLuisi, J., Augustine, J., Dutton, E., Nelson, D., Forgan, B., Novotny, P., Hickey, J., Love, S. P., Bender, S., McArthur, B., Ohmura, A., Seymour, J. H., Foot, J. S., Shiobara, M., Valero, F. P. J., and *Strawa, W.*, 1998: The Baseline Surface Radiation Network pyrgeometer round-robin calibration experiment. *J. Atmos. Oceanic Technol. 15,* 687-696.

Philipona, R., Dutton, E., Stoffel, T., Michalsky, J., Reda, I., Stifter, A., Wendling, P., Wood, N., Clough, A. S., Mlawer, E. J., Anderson, G., Revercomb, H. E., Shippert, T. R., and *Timothy, R.*, 2001: Atmospheric longwave irradiance uncertainty: Pyrgeometers compared to an absolute sky-scanning radiometer, atmospheric emitted radiance interferometer and radiative transfer model calculations. *J. Geophys. Res. 106* , 28,129- 28,142.

WMO, 1996: Guide to meteorological instruments and methods of observation. WMO-No. 8, 6th edition.

IDŐJÁRÁS

Quarterly Journal of the Hungarian Meteorological Service
Vol. 105, No. 4 — Vol. 106, No. 1, October 2001 — March 2002, pp. 231–242

A space-based GPS meteorological application

Éva Borbás[1], **Paul Menzel**[2] and **Jun Li**[1]

[1]*Space Science and Engineering Center, University of Wisconsin / Madison, 1225 West Dayton St., Madison, WI, 53706, USA; E-mail: eva.borbas@ssec.wisc.edu*

[2]*NOAA/NESDIS Office of Research and Applications, 1225 West Dayton St., Madison, 53706, WI, USA*

(Manuscript received November 2, 2001; in final form December 12, 2001)

Abstract—The First Global Positioning System (GPS) satellite was launched in 1978, but the history of GPS meteorology (radio occultation) began in the 1960's with the beginning of the interplanetary flight. The studies of GPS meteorological applications appeared shortly after GPS system started to operate. In the literature many papers can be found about both the space-based and ground-based GPS applications; several papers discuss the opportunity of using GPS data for NWP and climatological applications. In this paper another GPS meteorological application is described. Radiances from current polar orbiting infrared (IR) and microwave (MW) sounders are used to derive temperature and moisture profiles in the troposphere in a physical retrieval algorithm. Specifications of the tropopause and the surface are necessary information in the profile retrieval. While the altitude of tropopause can be difficult to define in radiometric approaches, the GPS provides an opportunity to derive very accurate upper atmospheric temperature profiles by using radio occultation (RO) techniques. In this paper we show that the combination of radiometric (IR and MW) and geometric (RO) information yields improved tropospheric temperature and moisture profiles when compared to those inferred from either system alone.

Key-words: GPS occultation, ATOVS temperature and humidity retrieval

1. Introduction

Precise observations of the atmospheric water vapor and temperature with good temporal and spatial coverage are essential for weather prediction and climate research. The existing ground-based meteorological observing systems do not provide enough information about the state of the atmospheric temperature and especially rapidly changing variables like humidity. Currently

humidity observations that are operationally available for Numerical Weather Prediction (NWP) models are radiosonde data twice per day at about 200 km spatial resolution over land, and satellite data over clear sky regions. To get precise, timely and frequent information about humidity is one of the important problems of weather prediction. This would improve the accuracy of short-term cloud and precipitation forecasts by creating a better initial state for the NWP model. In satellite meteorology, because of the poor vertical resolution of the current observing systems, radiometric techniques are unable to distinguish the tropopause altitude. IR and MW sounders have limited skill in the stratosphere. The Global Positioning System is capable of deriving very accurate upper tropospheric and stratospheric temperature and moisture profiles by using radio occultation (RO) techniques. For climatological research long term, global, homogeneous and stable data sets are necessary. The GPS provides an opportunity to derive very accurate, long term, global coverage of atmospheric temperature and humidity profiles and total precipitable water (TPW) measurements.

This paper introduces the latest status in the space based GPS Meteorology as atmospheric sounding and shows some results of our own study in this field. In Section 2 the GPS meteorology will be defined and the short history of its development will be mentioned. Section 3 will highlight the advantages and disadvantages of this new method and discuss some solutions for its shortcomings. Future systems will be introduced in Section 4. Finally, in Section 5 the own results of a simulated study are described.

2. GPS meteorology

The Global Positioning System is a space based navigation system created by the United States (US) Department of Defense (DOD) originally for military purposes. The system consists of 24 GPS satellites orbiting the Earth at an altitude of 20,200 km in 6 orbit panels. The first GPS satellite was launched in 1978. The system description can be found in detail in *Hoffmann-Wellenhof et al.* (1993). A very similar Russian navigation system called Global Navigation Satellite System (GLONASS) (*http://www.rssi.ru/SFCSIC/SFCSIC_main.html*) has been operating since 1996. There are receivers able to receive signals from both systems (*Allan*, 1996) providing an opportunity to choose the best positioning satellite for processing purpose, however they are not well spread.

The history of GPS meteorology (*Lee et al.*, 2001) started in the 1960's with the first days of the interplanetary flight. At that time the team of Jet Propulsion Laboratory (JPL) and Stanford University had the idea to probe the atmosphere of Mars and later other planets using the radio link between the

Earth and Marine 3 and 4 spacecrafts. Using RO techniques to investigate the neutral atmosphere, especially to measure the refractivity profiles of the planets, became possible after developing the two way coherent Doppler Tracking system and introducing the Abel transformation (*Fjeldbo* and *Eshleman*, 1968), the latter which converts the observed bending angle to refractivity. Using the radio occultation technique to investigate the neutral atmosphere of the Earth became realistic (less cost effective) with the appearance of the Global Positioning System. In 1988, GPS Geoscience Instrument (GGI) (JPL and the Stanford University) submitted the first GPS occultation proposal to NASA, and in 1995 NASA's first Low Earth Orbiting (LEO) satellite called MicroLab-1, carrying a small GPS receiver, was launched. This program called GPS/MET (*Ware et al.*, 1995) and operated by the University Corporation for Atmospheric Research (UCAR) has successfully demonstrated active limb sounding of the earth's atmosphere using radio occultation technique. More than 70,000 occultation data were collected between April 1995 and February 1997 providing big data base for demonstrating purposes and for making statistical comparisons. *Ware et al.* (1996) and *Kursinski et al.* (1996) made the first validation of these data. An other comprehensive analysis and validation study (*Rocken et al.*, 1997) showed that the agreement between refractivity profiles from GPS/MET data, Numerical Weather Prediction model analyses and radiosonde data are promising especially in the layer between 5 and 30 km. The standard deviation of the differences is about 2%. In July 15, 2000, after the success of the GPS/MET program, the German CHAMP (CHAllenging Minisatellite Payload) LEO satellite was launched with the latest generation of JPL GPS receivers. The objective of this mission is almost the same of the GPS/MET program, i.e., to perform limb sounding of the Earth's neutral atmosphere and ionosphere and also to determine the Earth's gravity and magnetic fields. CHAMP has an improved antenna providing improved signal quality. Its capabilities enable sounding better into the lower troposphere than the GPS/MET system. The first validation result (*Wickert et al.*, 2001) showed that the GPS-observed temperature bias (comparing to the NWP analyses) is less than 1 K above tropopause and less than 0.5 K in the 12 and 20 km at latitudes higher than 30 degree.

The meteorological applications of GPS are so widespread, that we can speak about separated branch of meteorology called GPS meteorology. These applications can be subdivided to space-based and ground-based GPS meteorology depending where the GPS receiver is placed. In this paper we focused on the space-based GPS meteorology, which uses the radio occultation technique to derive meteorological profiles (temperature or humidity) from the measured bending angle (refractivity) profiles. The equation relating the GPS

atmospheric refractivity (index of refraction) to atmospheric temperature and moisture was first expressed by *Smith* and *Weintraub* (1953):

$$N = 77.6\frac{P}{T} + 3.73 * 10^5 \frac{P_w}{T^2}, \tag{1}$$

where P is the atmospheric pressure (hPa), P_w is the water vapor partial pressure (hPa) and T is the temperature (K) of the atmosphere. The first term is referred to as the dry or hydrostatic term, and the second one is the wet or moist term. The detailed description of the GPS radio occultation technique can be found in *Lee et al.* (2001).

A network of several ground based GPS receiver stations is also necessary for the navigation system. During the processing of GPS signals, the effect (time delay and curving of the signals) of the troposphere, called tropospheric delay were considered as a noise and a number of methods were developed to estimate and eliminate it (*Bevis et al.*, 1992). Using these methods the total precipitable water, which is the function of the troposheric delay, can be determined for every GPS station. In spite of the fact that some of these methods have been available since 1970's, the data of the permanent GPS networks has been used for meteorological purposes only since 1990's related to getting precise enough ephemeris in a reasonable time for quazi-operational purposes. Since this time was shortened from 2 weeks to several hours, this application became promising for use in meteorological prediction. The number and size of these networks is growing very quickly (e.g., the Japanese GPS network already includes at least 1000 permanent GPS stations).

Another type of error in the GPS technique is the effect of the multipath signals, which may be also a new type data source in the future. It occurs when the GPS signals arrive at the receiver's antenna not only from the satellites, but from a nearby reflecting surface as well. *Komjathy et al.* (2000) demonstrated that GPS signals reflected from the ocean surface and received at an aircraft altitude of 3 to 5 km can be a remote sensing application to determine ocean surface wind speeds. This technique can be a new source of data for research of global ocean current circulation and global warning if similar results can be obtained using a GPS receiver on a LEO satellite.

3. Advantages and disadvantages of RO

One of the main advantages of the GPS occultation technique is that it does not require calibration, providing long-term stability of products near real-time in all weather conditions. Theoretically, one receiver carried on a LEO satellite

can measure 500 profiles per day with global coverage of the Earth in space and time. In practice, the GPS/MET system could measure about 250 occultations per day, and after filtering, about 150 occultations per day could be collected. This number can be higher in the case of the CHAMP satellite carrying a higher quality receiver and antenna. An 8 LEO satellite constellation could already provide 4000 soundings per day (see COSMIC mission, *Lee et al.,* 2001).

The system has a very high vertical resolution: 1.5 km in the stratosphere and 0.5 km in the lower troposphere. It is mainly limited by diffraction and horizontal atmospheric inhomogeneity (*Kursinski et al.*, 1997). The horizontal resolution is about 300 km, limited by the assumption of spherically symmetrical atmosphere in the Abelian transformation. Both resolutions can be improved by different methods like "backpropagation technique" (*Gorbunov and Gurvich*, 1998) or the holography method (*Hocke et al.,* 1999). Another method to avoid the error due to the spherical symmetry is the use of the bending angle profiles as GPS measurements via direct assimilation into the NWP model using variation method (*Healy and Eyre*, 2000). Using the GPS bending angle profiles directly also can be a solution for another disadvantage of the system: the ambiguity in separating the dry and moist contributions to the total refractivity. From the GPS refractivity profiles, derived from the bending angle profiles, the temperature profiles or the humidity profiles can be computed (see Eq. 1) if the other is known. Likewise, the temperature profiles can be computed from the dry area of the atmosphere. Another approach is to use the NWP temperature profiles as ancillary information to get the GPS humidity profiles.

The accuracy of the GPS products was estimated by *Kursinski et al.* (1997). The accuracy of the GPS refractivity profiles is the greatest (0.4%) or about 1 K for temperature in ranges from 5 km to 30 km. The accuracy became worse above and below this layer. Errors below 5 km are due to the variable water vapor content, multipath effect and the receiver itself, which can not always maintain phase lock in this region due to the low Signal to Noise ratio. Inconsistencies above 30 km are caused by measurement errors, calibration errors, and the effects of the solar and diurnal cycles in the ionosphere.

The RO retrieval method can still be improved in the future. In the lower troposphere the signal to noise ratio can be increased with higher gain antennas and lower-noise amplifiers as demonstrated by the now operating CHAMP satellite (*Wickert et al.*, 2001) carrying the latest version of JPL GPS flight receivers, since more than half of the selected profiles in the study reached the 1 km above the surface. An improved ionosphere calibration method would improve stratospheric retrievals and reduce the systematic errors that occur during the daytime retrievals because of the solar cycle maximum.

4. Future systems

After the successful GPS/MET project, the currently operating German CHAMP LEO satellite can provide an opportunity for the preparation for operational RO missions. The first operational RO mission will start with the launch of the Metop EUMETSAT Polar Satellite (EPS) around 2005. At that time the EPS Metop will already be part of the Joint Polar system (JPS) with the NPOESS (National Polar-orbiting Operational Environmental Satellite System) satellites, which also will carry GPS receivers (GPSOS) both providing 500 occultations per day since 2009.

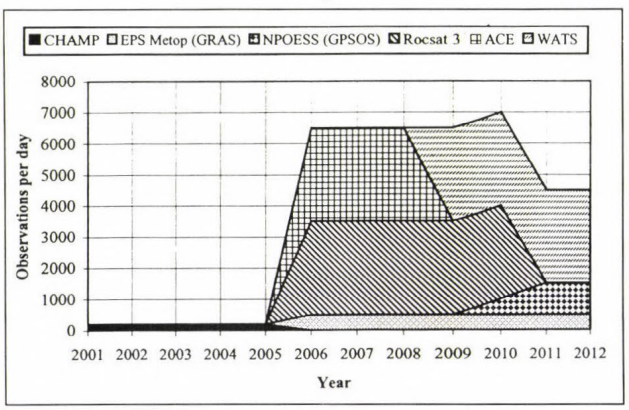

Fig. 1. Predicted radio occultation data sources based on planned and proposed missions (*Luntama*, 2001).

One of the proposed scientific small satellite missions is the ROCSAT-3 program, which is a collaboration project between UCAR (USA) and National Space Program Office (NSPO) (Republic of China) to develop a constellation of eight low-earth orbiting satellites. The system is called Constellation Observing System for Meteorology, Ionosphere and Climate (COSMIC) (*Lee et al.*, 2001). The program is planned for the 2005–2010 period. Other small satellite programs are the ACECHEM (Atmospheric Composition Explorer for Chemistry and Climate Interaction) with a 6-satellite constellation, proposed operation between 2005 and 2008; and WATS (Water Vapour and Wind in Atmospheric Troposphere and Stratosphere) starting about 2008/2010. Both are candidates of ESA Earth Explorer Core Missions for climate monitoring. The predicted future daily number observations (occultations) are shown in *Fig. 1*. The figure shows that in the near future the number of the observations may be much more than that obtained from the currently existing radiosonde observation network.

In the literature many papers can be found about GPS/MET validation (*Ware et al.*, 1996; *Rocken et al.*, 1997) and about different meteorological case studies using the GPS/MET observations (*Nishida et al.*, 2000; *Kuo et al.*, 1998). Several papers discuss the opportunity of NWP and climatological application. In the next section another GPS meteorological application is described: GPS data are used in the radiometric temperature and humidity radiometric retrieval method.

5. An example of the application of GPS occultation: a simulation study

The aim of this simulation study was to investigate the effect of combining the radio occultation and radiometric data on temperature and moisture profile retrievals as a possible meteorological application of GPS RO technique. Radiometric retrieval techniques using measurements from polar orbiting IR and MW sounders are used to infer temperature and moisture profiles in the lower and upper troposphere. Combining the two systems better quality of retrieved temperature and humidity profiles is expected as they have complementary characteristics: the radiometric technique has limited skill in the stratosphere and to detect the altitude of tropopause. Also, the measurements have good horizontal resolution, but less good vertical resolution. Since the GPS RO technique has a very good vertical resolution but poorer horizontal resolution, it is capable of deriving very accurate upper tropospheric and stratospheric temperature or refractivity profiles. It lacks skill in the low troposphere (see before). The best characteristic of RO technique for improving the radiometric retrieval method is that it can provide very accurate and detailed information around the tropopause.

5.1 Simulation approach

In our study, temperature and humidity retrievals were performed using a statistical regression approach. For simulating the IR and MW brightness temperatures, GPS refractivity and temperature profiles, and surface-based temperature and humidity observations, the NOAA88 radiosonde dataset was used which contains 7547 radiosonde profiles globally distributed in space and time. The profiles have been interpolated into 42 pressure levels from 0.1 hPa to 1050 hPa.

The simulated IR and MW data represent the NOAA Advanced TIROS Operational Vertical Sounder (ATOVS). It has three instruments: the High-resolution Infrared Radiation Sounder (HIRS) with 19 IR and one visible

channels, mainly used for temperature sounding at a maximum horizontal resolution of 18 km (at nadir point). The second instrument is the Advanced Microwave Sounding Unit-A (AMSU-A) with 15 MW channels, measuring energy within the oxygen absorption bands, so it is temperature sensitive. Its horizontal resolution is 45 km at nadir and 125 km at board. The new five channel microwave humidity sounder (AMSU-B) has a best horizontal resolution of 17 km at nadir. The brightness temperatures of the 19 IR and the 20 MW channels were simulated by using a so-called PFAAST pressure layer model fast algorithm for atmospheric transmittances (*Hannon et al.*, 1996). Microwave surface emissivity is inferred from the AMSU-A 50.3 GHz window channel brightness temperature (*Huang and Li*, 1998). In the simulation nominal instrument plus 0.2 K forward model noise were randomly added to the measurements.

To get ancillary information about tropopause, we simulated the GPS refractivity profiles representing the RO derived measurements from a GPS LEO satellite. The noise and vertical resolution of GPS profiles were estimated by a very detailed simulation study (*Kursinski et al.*, 1997). The GPS profiles were simulated on 16 levels between 5 and 30 km, where the best accuracy was accepted. Below 5 km, the noise became bigger because of the presence of moisture and the limitation of GPS occultation technique (see above). Above 30 km, ionospheric electrons cause increased noise. The vertical resolution is limited by the diffraction: 2 km below about 15 km height and 1.5 km above this level. The noise of refractivity was 0.4% on every level.

Another boundary condition of the radiometric retrieval technique is the specification of the surface. Surface temperature and humidity were defined as the lowest level of the RAOB profiles. 0.5 Kelvin temperature and 10% mixing ratio were added to generate noises.

Retrievals were performed using a statistical regression approach. Regression coefficients were computed from 90% of all RAOB profiles and the remaining 10% were used for verification. Bias and rms errors were computed between the retrievals and RAOB profiles in 1 km layers for temperature profiles and 2 km layers for humidity. Bias and rms errors for humidity were normalized by the true value to get the statistics in percentage.

In the statistical regression scheme, both linear and quadratic terms for brightness temperatures, GPS profiles and surface observations were used. This resulted in an 7.4% (from 24.9% to 17.5%) improvement of rms error in the total precipitable water over using just linear terms of ATOVS and GPS measurements. The main improvements are caused by using the quadratic terms of AMSU-B brightness temperature because humidity is a nonlinear function of brightness temperature in the radiative transfer equation, but a linear function of the refractivity (see equation above).

5.2 Results

To study the impact of the different information sources (ATOVS, GPS, and surface), the following combinations of retrievals were calculated:

- Retrievals using HIRS brightness temperature;
- Retrievals using HIRS data and surface (SFC) temperature and humidity;
- Retrievals using HIRS + SFC and GPS refractivity profiles;
- Retrievals using HIRS + GPS data;
- Retrievals using HIRS +AMSU (ATOVS) brightness temperature;
- Retrievals using ATOVS + SFC data;
- Retrievals using ATOVS + GPS + SFC data, and
- Retrievals using ATOVS + GPS data.

The bias and rms errors were computed between the retrievals obtained from these different combinations of information and NOAA88 radiosonde profiles. These statistics for temperature retrievals are shown in *Fig. 2* and for humidity retrievals in *Fig. 3*.

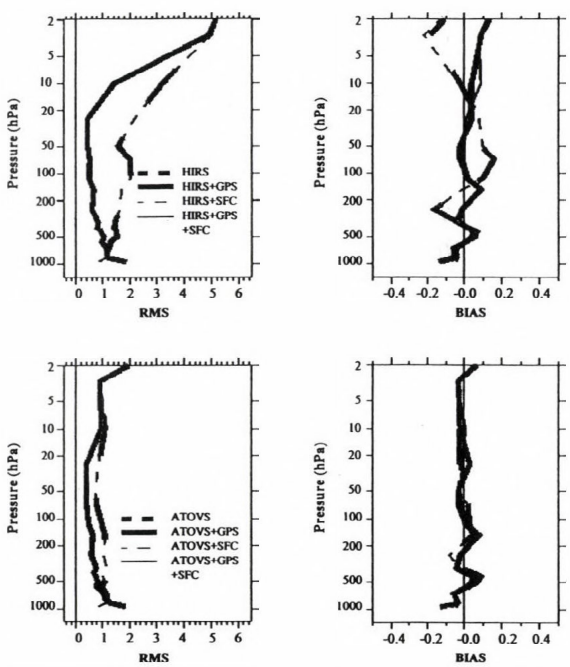

Fig. 2. RMS and BIAS (K) of temperature profiles between NOAA88 radiosonde profiles and the retrievals using different sources of data. Retrievals without AMSU (upper panels) and with AMSU (lower panels) are shown.

The effect of GPS information on HIRS retrievals is an about 1.5 K improvement in the layers above 100 hPa level and more than 0.5 K below down to the 475 hPa pressure level. Note that the HIRS instrument can characterize the GOES sounder as well since its sounder has similar characteristics (18 infrared channel). The effect of GPS refractivity profiles on the ATOVS temperature retrievals is less dramatic (lower panel of Fig. 2). It is a 0.3 K improvement between the 400 and 15 hPa layers with the maximum of 0.48 K in layer 135–85 hPa. The surface temperature and humidity information can improve the retrieval in the surface layer by about 1 K in both (HIRS and ATOVS retrieval) cases. Significant difference (positive effect) between using or not AMSU channel information can be seen above 10 hPa level, where other data were not available. It can be seen that the most powerful combination is when we use all data together (gray narrow solid line on the lower panel of Fig. 2). The rms error of that "best case" is under the 1.2 K between 3 and 920 hPa pressure levels. The biases in all cases were under the $\pm$ 0.2 K.

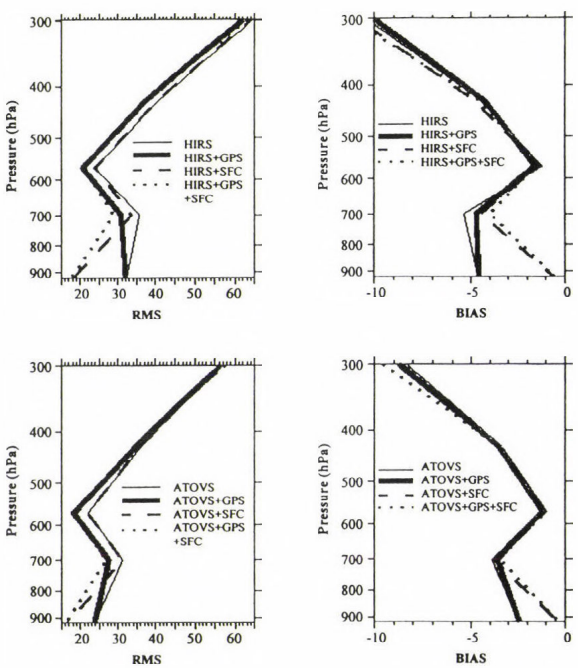

Fig. 3. RMS and BIAS errors of humidity (mixing ratio, in unit %) between NOAA88 radiosonde profiles and the retrievals using different sources of data. Retrievals without AMSU (upper panels) and with AMSU (lower panels) are shown.

It is evident that the effect of GPS refractivity profiles on radiometric humidity retrievals is less important than it was for temperature because the refractivity profiles were derived only above altitude of 5 km where the water vapor content is already very low. The maximum improvement of GPS data on HIRS humidity retrievals is 4.7% in the 780–620 hPa layers, while the impact on ATOVS retrievals is 4.3%. Surface observations are obviously very useful; their effect on ATOVS retrieval in the surface layer is a 7.6% improvement. The biases of humidity retrievals are negative, but using more information sources decreased them.

6. Summary

This paper introduced GPS meteorology with a short history of its development. The advantages and disadvantages of this new meteorological application were mentioned. Further improvements in the proposed future systems suggest that this scientific area is very promising. Several papers discuss the opportunity for NWP and climatological applications, but in this paper another GPS meteorological application is described: the use of GPS data to support the retrieval of temperature and humidity profiles from satellite radiances. In this study we followed a statistical regression approach, using radiometric (IR and MW) and radio occultation data. The test results showed that the RO data improved the IR and MW retrievals of temperature and moisture in the upper troposphere and the temperature retrievals in the stratosphere. The best quality results were obtained by using all of sources of information.

In the future this study will be repeated on real data (RO data from GPS/MET or CHAMP measurements) to do a fully independent validation.

Acknowledgements—This work was supported in part by NOAA Cooperative Agreement NAO7EC0676 and by the Hungarian National Research Foundation (OTKA-T032466).

References

Allan, D.W., 1996: Harmonizing GPS and GLONASS. *GPS World, May 1996*, 51-53.

Fjeldbo, G. and *Eshleman, V.R.*, 1968: The atmosphere of Mars analyzed by integral inversion of the Marine IV occultation data. *Planet. Space Sci. 16*, 1035-1059

Gorbunov, M.E. and *Gurvich, A.S.*, 1998: Microlab-1 experiment: Multipath effects in the lower ptroposphere. *J. Geophys. Res. 103*, D12, 13,819-13,826.

Hannon, S., Strow, L.L., and *McMillan, W.W.*, 1996: Atmospheric infrared fast transmittance models: A comparison of two approaches. *Proc. SPIE, 2830*, 94-105.

Healy, S. B. and *Eyre, J. R.*, 2000: Retrieving temperature, water vapour and surface pressure information from refractive-index profiles derived by radio occultations: A simulation study. *Quart. J. Roy. Meteor. Soc. 126*, 1661-1683.

Hocke, K., Pavelyev, A G., Yakovlev, O.I., Barthes, L., and *Jakowski, N.*, 1999: Radio occultation data analysis by the radioholographic method. *J. Atmos. Soar-Terr. Phys. 61*, 1169-1177.

Hoffmann-Wellenhof, B., Lichtenegger, H., and *Collins, J.*, 1993: *GPS-theory and Practice.* Springer Verlag ,Wien, New York. Second edition.

Huang, H. L. and. *Li, J.*, 1998: Determination of microwave emissivity from Advanced Microwave Sounder Unit measurements. *Proc. of SPIE, The International Society for Optical Engineering, 3503*, 233–237.

Komjathy, A., Zavorotny, V. U., Axelrad, P., Born, G. H., and *Garrison, J. L.*, 2000: GPS signal scattering from sea surface: Wind speed retrieval using experimental data and theoretical model. *Remote Sensing of Environ. 73*, 162-174.

Kuo, Y.-H., Zou, X., Chen, S. J., Huang, W., Guo, Y.-R., Anthes, R. A., Exner, M., Hunt, D., Rocken, C., and *Sokolovskiy, S.*, 1998: A GPS/MET sounding through and intense upper-level front. *Bull. Amer. Meteor. Soc. 79*, 617-626.

Kursinski, E.R., Hajj, G.A., Bertiger, W.I., Leroy, S.S., Meehan, T.K., Romans, L.J., Schofield, J.T., McCleese, D.J., Melboume, W.G., Thornton, C.L., Yunk, T. P., Eyre, J.R., and. *Nagatani, R. N.*, 1996: Initial results of radio occultation observations of Earth's atmosphere using the global positioning system. *Science 271*, 1107-1110.

Kursinski, E.R., Hajj, G.A., Schofield, J.T., Linfields, R.P., and *Hardy, K.R.*, 1997: Observing Earth's atmosphere with radio occultation measurement using the Global Positioning System. *J. Geophys. Res. 102*, 23,429-23,465.

Lee, L.-C., Rocken, C. and *Kursinski, R.*, 2001*: Applications of Constellation Observing system for Meteorology, Ionosphere & Climate.* Springer Verlag, Hong Kong Ltd.

Luntama, J.-P., 2001: Space based GPS Meteorology and GOS.
http: //www.wmo.ch/hinsman/CGMS Workshop web/Luntama web/sld015.thm.

Nishida, M., Shimizu, A., Tsuda, T., Rocken, C., and *Ware, R.H.*, 2000: Seasonal and longitudinal variations in the tropical tropopause observed with the GPS occultation technique (GPS/MET). *J. Meteor. Soc. Japan 78*, 691-700.

Rocken, C., Anthens, R., Exner, M., Hunt, D., Sokolovskiy, S., Ware, R., Gorbunov, M., Schreiner, W., Feng, D., Herman, B., Kuo, Y.-H., and *Zou, X.*, 1997: Analysis and validation of GPS/MET data in the neutral atmosphere. *J. Geophys. Res. 102*, No. D25, 29,849-29,866.

Smith, E.K. and *Weintraub, S.*, 1953: The constants in the equation for atmospheric refractive index at radio frequencies. *J. Res. Natl. Bur. Stand. 50*, 39-41.

Ware, R.H., Exner, M.L., Herman, B. M., Kuo, Y-H., Meehan, T.K., and *Rocken, C.*, 1995: GPS/MET Preliminary Report, July 1995. *http://cosmic.cosmic.ucar.edu/gpsmet/over/septsumm_top.html*

Ware, R., Exner, M., Feng, D., Gorbunov, M., Hardy, K., Herman, B., Kuo, Y., Meehan, T., Melbourne, W., Rocken, C., Schreiner, W., and *Trenberth, K.*, 1996: GPS sounding of the atmosphere from low earth orbit: Preliminary results. *Bull. Amer. Meteor. Soc. 77*, 19-40.

Wickert, J., Reigber, C., Beyerle, G., König, R., Marquardt, C., Schmidt, T., Grunwaldt, L., Galas, R., Meehan, T.K., Melbourne, W.G., and *Hocke, K.*, 2001: Atmosphere sounding by GPS radio occultation: First results from CHAMP. *Geophys. Res. Lett. 28*, 3263-3266.

IDŐJÁRÁS

Quarterly Journal of the Hungarian Meteorological Service
Vol. 105, No. 4 — Vol. 106, No. 1, October 2001 — March 2002, pp. 243-251

High accuracy skin temperature retrieval from spectral data of multichannel IR imagers

Ferenc Miskolczi

Science Applications International Corporation,
1 Enterprise Pkwy, Suite 300, Hampton, VA 23666, USA
E-mail: f.m.miskolczi@larc.nasa.gov

(Manuscript received November 14, 2001)

Abstract—The increasing number of IR spectral channels of recent satellite imagers implies the more accurate retrieval of surface skin temperature. In this paper the theoretical accuracy limits as a function of channel numbers, viewing angles and noise equivalent radiances have been studied. Based on LBL computations of the channel radiances regression type relationships have been established between the brightness temperatures and the skin-temperatures. In this study model filter functions of the 7 IR channels of the GLI imager of the ADEOS-I have been used with a large set of temperature profiles. The global and seasonal distribution of temperature profiles were considered by groups of climatologically representative temperature profiles. Standard singular value decomposition program package was used to solve the multivariable linear regression problem. Results show that the accuracy limits of the skin temperature retrievals are depending mainly on the noise equivalent radiances and up to around 60 degree viewing angles remaining in the range of 0.1–0.2 K.

Key-words: remote sensing, skin temperature, ADEOS

1. Introduction

Satellite based remote sensing of the Earth-atmosphere system has an increasing role in climate change detection. Imager instruments have nowadays improved accuracy and more channels allowing the development of better retrieval algorithms for a variety of surface and atmospheric parameters. The first step in the retrieval of the surface temperature is to derive the accurate skin temperature from the radiance measurements. Formerly, with imagers using one or two spectral channels, accuracy was limited. The necessary information on the characteristics and involvement of the H_2O and other molecular species in the windows absorption was unavailable. The Global Imager, (GLI), on board the Advanced

Earth Observing Satellite, (ADEOS 2), offers four window channels and three H_2O channels for better surface temperature detection with a possibility of obtaining information on the initial trend of the moisture profile. In the present paper, the theoretical accuracy limits of the clear-sky skin temperature retrievals using the GLI infrared channels have been established, based on high resolution radiative transfer computations and regression analysis.

2. Method

For a given filter function the average wave number, the effective wave number and the channel radiance are expressed as:

$$v_k^a = \frac{\int_{\Delta v} v \Phi_k(v)\, dv}{\int_{\Delta v} \Phi_k(v)\, dv}, \tag{1}$$

$$v_k^e = \frac{\int_{\Delta v} v I(v)\, \Phi_k(v) dv}{\int_{\Delta v} I(v)\, \Phi_k(v)\, dv}, \tag{2}$$

and

$$I_k = \frac{\int_{\Delta v} I(v) \Phi_k(v) dv}{\int_{\Delta v} \Phi_k(v) dv}, \tag{3}$$

where $I(v)$ is the spectral radiance, $\Phi_k(v)$ is the filter function, v is the wave number and the subscript k refers to the serial number of the spectral channel. In *Table 1* the GLI and GOES-8 filter functions are compared. Some GOES-8 channels are close to the corresponding GLI channels, therefore the results and conclusions could also be valid for those filters.

Table 1. Average wave numbers, v_k^a, and half widths, β_k, of the GLI engineering model filter functions and some similar GOES-8 filter functions (units are in cm^{-1})

No.	GLI		GOES-8	
	v_k^a	β_k	v_k^a	β_k
1	836.47	52.52	835.97	64.18
2	945.83	69.60	934.75	86.06
3	1160.30	72.12		
4	1377.06	94.67		
5	1430.78	97.10		
6	1484.88	113.60	1482.04	122.76
7	2699.92	239.34	2559.44	165.62

Skin temperature retrieval using regression type relationships between the channel scene temperatures and the true radiative temperatures of the surface is very simple:

$$T = \alpha_0 + \sum_{k=1}^{N} \alpha_k T_k^c , \tag{4}$$

where T is the skin temperature, N is the number of the spectral channels, α_k's are regression coefficients and T_k^c's are the estimated scene temperatures. T_k^c's are computed from the brightness temperatures and they are supposed to be corrected for the shift in the effective wave number with the change in the structure of the spectral radiance. The brightness temperatures are computed from the channel radiances via the inverse Planck function and using the average wave number. The "accurate" scene temperature is computed the same way, but using the effective wave number. In case of an ideal black body radiance spectra, the magnitudes of the brightness temperature corrections at different GLI channels are presented in *Fig. 1*.

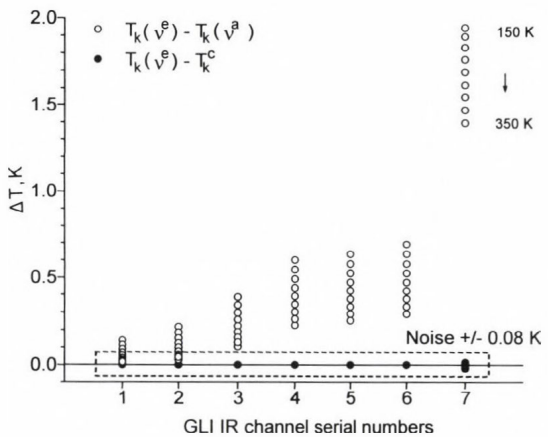

Fig. 1. Brightness temperature corrections using ideal black body functions in the range of 150–350 K. The dashed line is an assumed average noise level of the IR channels.

To perform the corrections there are several methods. NOAA uses linear (or more recently second order polynomial) fit, *Weinreb et al.* (1997). For the GLI channels we applied a logarithmical fit to express the effective wave number as the function of the channel radiance:

$$T_k^c = B^{-1}(v_k^c, I_k), \tag{5}$$

where

$$v_k^c = c_k^1 + c_k^2 \ln(I_k). \tag{6}$$

In the above equations v_k^c is the estimated effective wave number, c_k^1 and c_k^2 are regression coefficients. Eq. (5) and (6) proved to be more accurate, (not shown here), and uses less coefficients than the NOAA method. Brightness temperature corrections based on ideal black body radiation is not justified when the distribution of the spectral radiance does not follow the Planck's radiation law. In the present work the c_k^1 and c_k^2 regression coefficients were determined using real atmospheric radiance spectra. Obviously, since the degree of modulation of the ideal black body spectra is dependent on the optical path within the atmosphere, for correct scene temperature computations a set of regression coefficients are needed for different viewing angles.

In *Fig. 2*, the brightness temperature corrections as the function of the channel radiances are plotted for the GLI channel 6. The correction error is the difference between the corrections, $(T_k - T_k^c)$, using ideal black body type or real atmospheric spectra in Eqs. (5) and (6). In this channel, Fig. 2 shows a large (–0.68 K) bias, and actually suggests not to use any corrections based on ideal black body radiance spectra. The situation in the GLI channel 7 is similar, but with a bias of 0.5 K. In channel 1 and 2 the biases remain below the noise level.

In general, the success of the regression scheme given in Eq. (4) is entirely dependent on the accuracy of the computed channel radiances and the statistical representativeness of the atmospheric temperature, water vapor, ozone and other trace gas profiles.

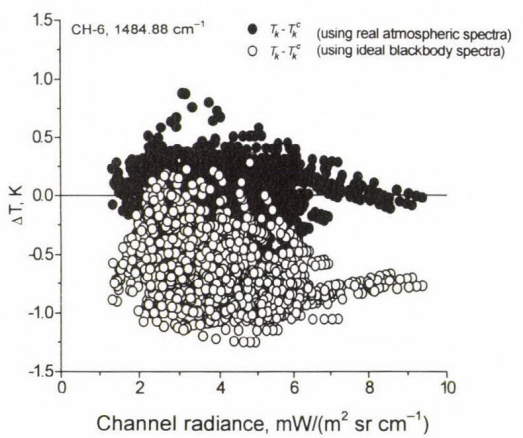

Fig. 2. Scene temperature error in the GLI water vapor channel due to the different brightness temperature correction methods.

3. *Regression data set*

The present study uses a subset of the TOVS Initial Guess Retrieval (TIGR), database of 1761 radiosonde observations (*Chedin* and *Scott*, 1983). This data set contains the pressure, temperature, H_2O and O_3 mixing ratio profiles at 40 pressure levels between 0.05 and 1013 hPa. The soundings were collected over both hemispheres and over all seasons from 1976. In *Table 2* the characteristics of the original data set are summarized.

Table 2. Average characteristics of the TIGR subset containing 1761 profiles in 11 classes (M is the number of profiles, u is in prcm, T_e is in K and p_e is in hPa)

	Region and season	M	u	T_e	P_e
1	Arctic summer	112	1.0	263	795
2	Arctic winter	295	0.3	250	779
3	North midlatitude summer	57	2.7	281	797
4	North midlatitude fall/spring	88	1.1	266	804
5	North midlatitude winter	332	0.9	263	804
6	North/South tropical	114	3.6	285	816
7	South midlatitude summer	131	1.6	271	808
8	South midlatitude fall/spring	155	1.0	264	805
9	South midlatitude winter	151	1.1	269	823
10	Antarctic summer	157	0.5	255	783
11	Antarctic winter	169	0.3	250	774

To obtain the best retrieval on a global scale, the profiles were classified according to their geographical latitudes and the seasons. Based on the latitudinal and annual distribution, 5 latitudinal belts were selected, and in each belt, one, two or three "seasons" were established, roughly based on the solar climate. Because of the apparent asymmetry in the global and seasonal distribution of the available solar radiation, the northern and southern hemispheres were treated separately. This classification of profiles resulted in 11 groups with a minimum of 57 profiles during the northern midlatitude summer, and a maximum of 331 profiles during the northern midlatitude winter. Further on, for practical reasons, it was necessary to reduce the number of the profiles to a reasonably small number, suitable for detailed line-by-line calculations. Due to the fact that the window channel radiances are affected mainly by the absorption of atmospheric water vapor, the selection of the individual TIGR profiles was based on the total precipitable water, u, effective H_2O temperature, T_e, and effective H_2O pressure, p_e. The effective values were computed by weighting the temperature and pressure profiles with the water vapor column density profile. A pre-selection based on the

statistical characteristics of the 11 groups resulted in 297 profiles. The extreme profiles from each group (profiles closest to the average +/- three standard deviations) have been excluded on the basis that we did not want the regression coefficients to be affected by some statistically insignificant rare cases. After eliminating the redundancies the final set has been reduced to 228 profiles. This set contained approximately 20 profiles in each class and has a similar statistical pattern to the original dataset.

4. Radiative transfer computation

For the radiance computations the High Resolution Radiative Transfer Code (HARTCODE) was used with the GEISA 97 absorption line catalog (*Miskolczi et al.*, 1990). In addition to the H_2O and O_3, there are nine molecular species that exhibit significant absorption in the GLI IR channels. The volume mixing ratio profiles of these absorbers (CO_2, N_2O, CH_4, NO, SO_2, NO_2, CCl_4, F11 and F12) were taken partly from the seasonal standard atmospheres. CCL_4, F11 and F12 mixing ratio profiles were measured at the Oklahoma ARM site. To create a physically consistent data set, after merging the additional absorbers into the TIGR profiles, a new exponential layering was introduced. The top altitude was set to 61.2 km and the number of the layers were reduced to 32. The new layers have a geometrical thickness of about 100 m at the bottom and 10 km at the top. The outgoing radiances were computed with 1 cm^{-1} spectral resolution in 9 different viewing angles, which makes a total of 2052 high resolution radiance spectra. In the convolution of the radiance spectra with the filter functions, the radiance spectra were interpolated to the higher resolution discrete points of the filter functions. The 1 cm^{-1} resolution was sufficient for the accurate evaluation of channel radiances in Eq. (3). The α_k regression coefficients in Eq. (4) were determined by singular value decomposition. In the present study, the first 6 GLI channels were utilized and in each group of profiles 9 set of regression coefficients were generated for each viewing angle. The reason of using 9 set of coefficients for 9 different viewing angles is in the fact that no uniform limb darkening function exists, even within one group of profiles. The best retrieval results are expected by using interpolated regression coefficients with respect to the viewing angles.

5. Results

According to test computations, the derived α_k regression coefficients were very stable, they were not sensitive to a 0.2 K white noise added to the scene temperatures, therefore, the regression coefficients were assumed to be error free. There

is no effect of the brightness temperature correction on the accuracy of the retrieval. This is expected, since the standard error in a linear regression scheme is invariant for the linear transformations of the variables. However, the use of brightness temperature instead of channel radiance improves the explained variance by about 4 to 5 per cent. It is interesting to note that the conversion of channel radiances into brightness temperatures or scene temperatures is not always beneficial. For example, in retrieving water vapor effective pressure, p_e, it is better to use directly the channel radiance. In *Figs. 3, 4* and *5* the different kinds of errors of the skin temperature retrievals as the function of the viewing angles are displayed. In all cases the computations were based on the estimated scene temperatures using Eqs. (5).

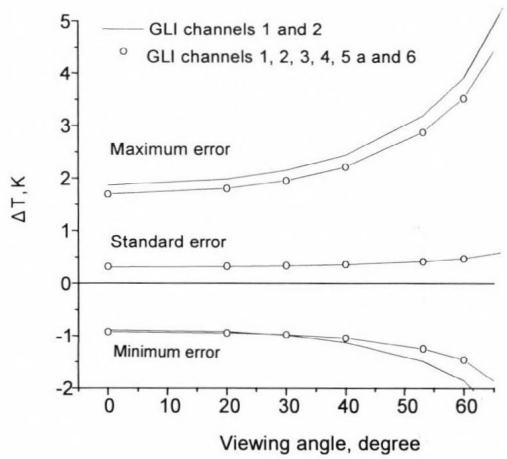

Fig. 3. Skin temperature errors in case of applying two or six spectral channels in the retrievals. (Full data set, no classes, 0.1 K noise.)

Fig. 3. shows the dependence of the errors on the number of the channels involved in the retrieval. In this case all the profiles in the 11 classes were merged into one large group of 228 profiles. It is surprising that adding an additional window channel and the three water vapor channels has no noticeable effect on the standard error, however, the minimum and maximum errors were slightly reduced. Probably there is a better way to use the information content of the excess channels than to include them directly into the regression scheme.

In Fig. 4 the effect of the grouping of the profiles are presented. Here the retrievals were based on the first 6 channels of the GLI. Apparently the accurate limb darkening corrections by using sets of regression coefficients for the different viewing angles are necessary to achieve an accuracy of around 0.1 K.

Fig. 5 shows the dependence of the errors on the noise equivalent temperatures. In this cases regression coefficients were generated for each class and viewing angle. The scene temperatures were loaded with a zero-mean white noise of different standard deviations. The close to linear degrading effect due to the measurement noise is obvious. The zero-noise curve at around 0.05 K can be regarded as a "theoretical" upper accuracy limit that can be obtained using simple linear regression methods.

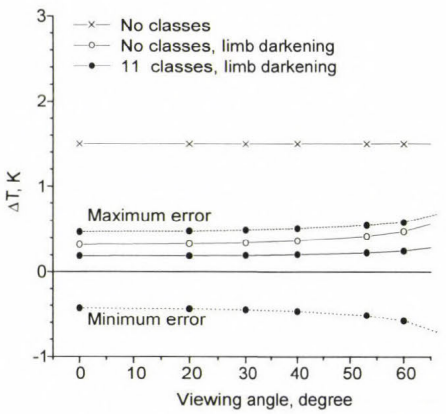

Fig. 4. Skin temperature errors in case of three different grouping. (2052 spectra in 1, 9 or 99 groups, 0.1 K noise.)

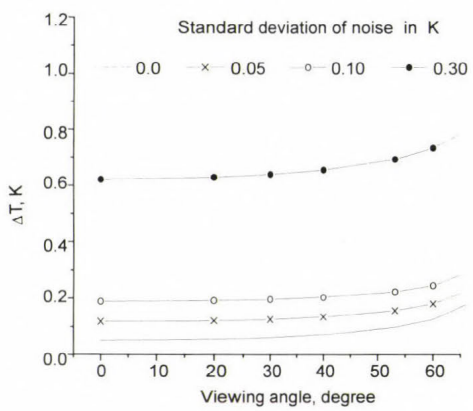

Fig. 5. Skin temperature errors in case of four different load of "white" noise.

6. Conclusions

Accurate skin temperature retrieval on global and annual scales can only be achieved by applying several sets of regression coefficients for the different regions, seasons and viewing angles. Limitations related to the instrument noise have been estimated. For the GLI instrument, assuming an average 0.08 K noise, the 0.3 K accuracy (in the sense of standard errors) is realistic. The target accuracy of the retrieval, using for example the GOES -10 imager, (assuming ~0.3 K noise and using less channels), could be around 0.6–0.8 K. Other conclusion is that sophisticated algorithms for the brightness temperature corrections using ideal black body, or even real atmospheric spectra, have no practical value when applying in a linear regression scheme. Further on, involving more H_2O and window channels into the retrieval will not increase the accuracy significantly. It seems that the only way of improvement is to reduce the noise in the spectral channels to or below 0.05 K.

References

Chedin, A. and *Scott, N., A.*, 1983: The improved initialization inversion procedure. *First International TOVS Study Conference*, Igls, Austria, August, 1983.

Miskolczi, F., Rizzi, R., Guzzi, R., and *Bonzagni, M*, 1990: High-resolution Radiance-Transmittance Code. *Meteor. Environ. Sci. Elsevier Pub. Co.* 743-790.

Weinreb, M.P., Jamieson, M., Fulton, N., Chen, Y., Johnson, J.X., Smith, B., and *Baucom, J.*, 1997: Operational calibration of geostationary operational environmental satellite imagers asounders. *Applied Optics 36*, 6895-6904.

IDŐJÁRÁS

Quarterly Journal of the Hungarian Meteorological Service
Vol. 105, No. 4 — Vol. 106, No. 1, October 2001 — March 2002, pp. 253-263

On the use of satellite-derived climatological data sets to map global land surface temperature range

Iván A. Csiszár

University of Maryland, Department of Geography
1121 LeFrak Hall, College Park, Maryland 20742 USA
E-mail: icsiszar@hermes.geog.umd.edu

(Manuscript received November 28, 2001)

Abstract—The long data record from operational environmental satellites allows the long-term, large-scale mapping of various characteristics of the Earth. This paper focuses on the diurnal temperature range (DTR) over land. The availability of necessary daytime and nighttime infrared radiation measurements within the various long-term satellite-based data sets is discussed. We conclude that currently the most suitable data sets for global DTR mapping are those that were produced by projects originally designed for the observation of atmospheric parameters: the International Satellite Cloud Climatology Project (ISCCP; mostly geostationary at low and mid-latitudes) and the Pathfinder Atmosphere from AVHRR (PATMOS; polar only). While ISCCP has more frequent sampling of the diurnal temperature cycle, there exists a large data gap over Asia due the lack of geostationary satellites. It is suggested that PATMOS data be used to fill this gap. However, daytime and nighttime PATMOS data need to be corrected for the effects of the local times of observation, which are not coincident with the times of occurrence of the daily maxima and minima. We demonstrate that, over hot surfaces, significant differences exist between coincident PATMOS surface temperatures and those from ISCCP corresponding to the same local time, indicating differences in calibration and/or in deriving surface skin temperature from top-of-the-atmosphere radiances. Residual differences also exist between coincident ISCCP and PATMOS daytime-nighttime temperature differences, suggesting that appropriate ISCCP to PATMOS normalization be made prior to adjusting PATMOS data for diurnal cycle effects to derive DTR maps.

Key-words: satellite data sets, land surface temperature, satellite observing systems

1. Introduction

Diurnal temperature range (DTR) is an important surface characteristic related to thermal inertia (*Price,* 1977). However, the properties of DTR on a global scale have not been investigated in detail. On a global scale, DTR can be

mapped and monitored only from space. Ideally, satellite measurements of the daily minimum and maximum temperatures are needed.

Operational geostationary environmental satellites (GOES, METEOSAT, INSAT, GMS,) have been providing meaningful temperature measurements between ~60°S and 60°N latitudes at a high temporal frequency, allowing the accurate estimation of daily temperature minimum and maximum. While thus the temporal sampling is sufficient for DTR mapping, the inter-satellite differences require a careful inter-calibration of the data (*Desormeaux et al.,* 1993).

The Advanced Very High Resolution Radiometer (AVHRR) on board the polar orbiting National Oceanic and Atmospheric Administration (NOAA) satellites has been providing global, near-continuous measurements over the last ~20 years. As AVHRR has on-board calibration capability of the infrared channels, in a radiometric sense the AVHRR data is relatively stable. While long-term records of its original 1-km resolution Local Area Coverage (LAC) measurements exist on a regional basis, full global continuous coverage is available only at the 4-km Global Area Coverage (GAC) resolution (*Gutman et al.,* 2001). GAC data are created from the 1-km data by a sampling and averaging procedure (*Kidwell,* 1998). From the six-hourly AVHRR measurements, the daytime (ascending orbit) and nighttime (descending orbit) temperature measurements from the "afternoon" satellites are the most useful for DTR mapping. However, the time of the observations rarely coincides with the occurrence of either the daily minimum or the daily maximum. In general, the inappropriate temporal sampling poses a bigger problem at daytime, when the temperature changes more rapidly over time. (Note that near the poles the overlapping orbits provide a much higher frequency of observations.)

Data from the geostationary and polar satellite systems have been collected and processed into well-documented climate data sets, particularly within the NOAA/NASA (National Aeronautics and Space Administration) Pathfinder Program (*Ohring* and *Dodge,* 1992). The World Climate Research Programme (WCRP) Global Energy and Water Cycle Experiment (GEWEX) also provides framework for the creation and collection of satellite data sets, in particular within the International Satellite Land Surface Climatology Project (ISLSCP, *Sellers et al.,* 1995) and the International Satellite Cloud Climatology Project (ISCCP, *Schiffer* and *Rossow,* 1983).

Long-term time series of daytime and nighttime measurements from the various operational geostationary and polar orbiting satellites are available from ISCCP. (Some of the specifications of the ISCCP products were defined at the Meeting on Real-time Satellite-derived Cloud Climatology in Balatonalmádi, Hungary in June 1980.) Although this data set was primarily designed for atmospheric applications, the clear-sky radiances allow the mapping of surface temperatures. This will be the primary data set considered in this paper for DTR mapping.

In principle, satellite-based DTR mapping also can be done by data from the global, long-term data sets that have been constructed from AVHRR data. The various existing data sets were designed to provide information for different applications. In general, surface applications require higher resolution data than atmospheric applications. The major such data sets are: the NASA Pathfinder Land data set (*James* and *Kalluri,* 1994), the NOAA/NESDIS Global Vegetation Index data set (*Gutman et al.,* 1995), Global Inventory Mapping and Modeling Studies (*Los et al.,* 1994), and the Global Land 1-km AVHRR data set (*Eidenshink et al.,* 1994). A common characteristic of these data sets is that daytime AVHRR data are preprocessed and mapped on a daily basis and then sampled in time into weekly or 10-day composites. Unfortunately, none of them include nighttime measurements and thus their usefulness for DTR mapping is limited.

The only AVHRR-based global, long-term data set that can be used for DTR mapping is the NOAA/NESDIS Pathfinder Atmosphere (PATMOS) data set, which includes daytime and nighttime AVHRR-derived radiance products from 1981 through 2000 on a global 10,000 km^2 equal-area grid (*Stove et al.,* 2002). Although this data set was created primarily for atmospheric applications, its clear-sky long-wave radiance products can be converted into surface temperatures. Thus, in addition to ISCCP, we will analyze PATMOS data for DTR mapping.

Note that surface temperature products are also available from data sets from other instruments on polar orbiting satellites, such as the Pathfinder TOVS (TIROS Operational Vertical Sounder on board the NOAA satellites) or Pathfinder SSM/I (Special Sensor Microwave Imager on board the Defense Meteorological Satellite Program satellites). As in many aspects the DTR mapping from TOVS and SSM/I these data have similar issues with AVHRR, they will not be discussed further in this paper. Also, data from the GOES Pathfinder project will not be discussed because of its limited spatial coverage.

In the remaining sections of this paper we analyze the relative merits of the ISCCP and PATMOS data sets for long-term, global DTR mapping. Description of the data used is provided in Section 2. Section 3 presents an intercomparison of data from PATMOS and ISCCP, followed by discussion and conclusions in Section 4.

2. The ISCCP and PATMOS data sets

2.1 ISCCP

From the suite of ISCCP products, we used the "mean surface (skin) temperature (T_s) from clear sky composite" product from the ISCCP Monthly Cloud Product D-2 data set from the 1984–1993 period. D-2 is a statistical

summary of the original satellite observations presented as monthly means in eight 3-hour intervals, from 00 through 24 UTC, mapped globally in an equal-area (280 km)^2 projection (*Rossow et al.*, 1996). T_s is derived from clear-sky infrared radiances corrected for water vapor absorption, assuming a surface emissivity of unity. In assigning data to a certain grid cell, data from geostationary satellites are preferred over polar data. Unfortunately, the ISCCP spatial coverage is poor over Central Asia, where only some observations from polar satellites are available due to the lack of coverage from the geostationary INSAT satellite (except for a 1-year period starting in April 1988). *Fig.1* shows data coverage in July 1993. Note the data gaps at 6 and 9 UTC, the time of the daily skin temperature maximum in that region. (Surface skin temperature very closely follows the solar radiative heating and thus on a cloud-free day daily skin temperature maximum occurs shortly after the local noon.) Missing data at 18 and 21 UTC indicate the lack of information on minimum temperature.

Filling these data gaps is one of the major issues of global DTR mapping. One plausible way is to establish relationships between ISCPP (mostly geostationary) and PATMOS (polar AVHRR) data outside the Asian gap and then use those relationships to estimate DTR within that region. In this context, AVHRR data from PATMOS are preferred to AVHRR data from ISCCP over the Asian gap because of possible effects of PATMOS-AVHRR preprocessing differences and consequent data incompatibility.

To estimate more precisely the daily maximum and minimum temperatures, an hourly global (except for the Asian gap) ISCCP-based surface temperature database was constructed by converting the 3-hour GMT time slots into local times, and interpolating the surface temperatures with cubic splines into a regular 1-hour grid. This database was used to specify daily maximum (T_{max}) and minimum (T_{min}) temperatures. DTR was calculated as $DTR = T_{max} - T_{min}$.

2.2 PATMOS

In the current analysis we used monthly mean daytime and nighttime, clear-sky, channel 4 and 5 brightness temperatures (T_{4d}, T_{4n}, T_{5d} and T_{5n}) derived from the corresponding long-wave radiance products and re-projected onto the ISCCP global grid. From the top-of-the atmosphere brightness temperatures daytime (T_{sd}) and nighttime (T_{sn}) skin temperatures were derived by the split-window equation from *Becker* and *Li* (1990):

$$T_{sx} = a + T_{4x} + b(T_{4x} - T_{5x}), \qquad x = d,n \tag{1}$$

using updated coefficients for each NOAA satellite by *Czajkowski et al.*

(1998). These formulae assume blackbody (i.e., emissivity = 1) surface and thus are compatible with the way ISCCP skin temperatures were derived.

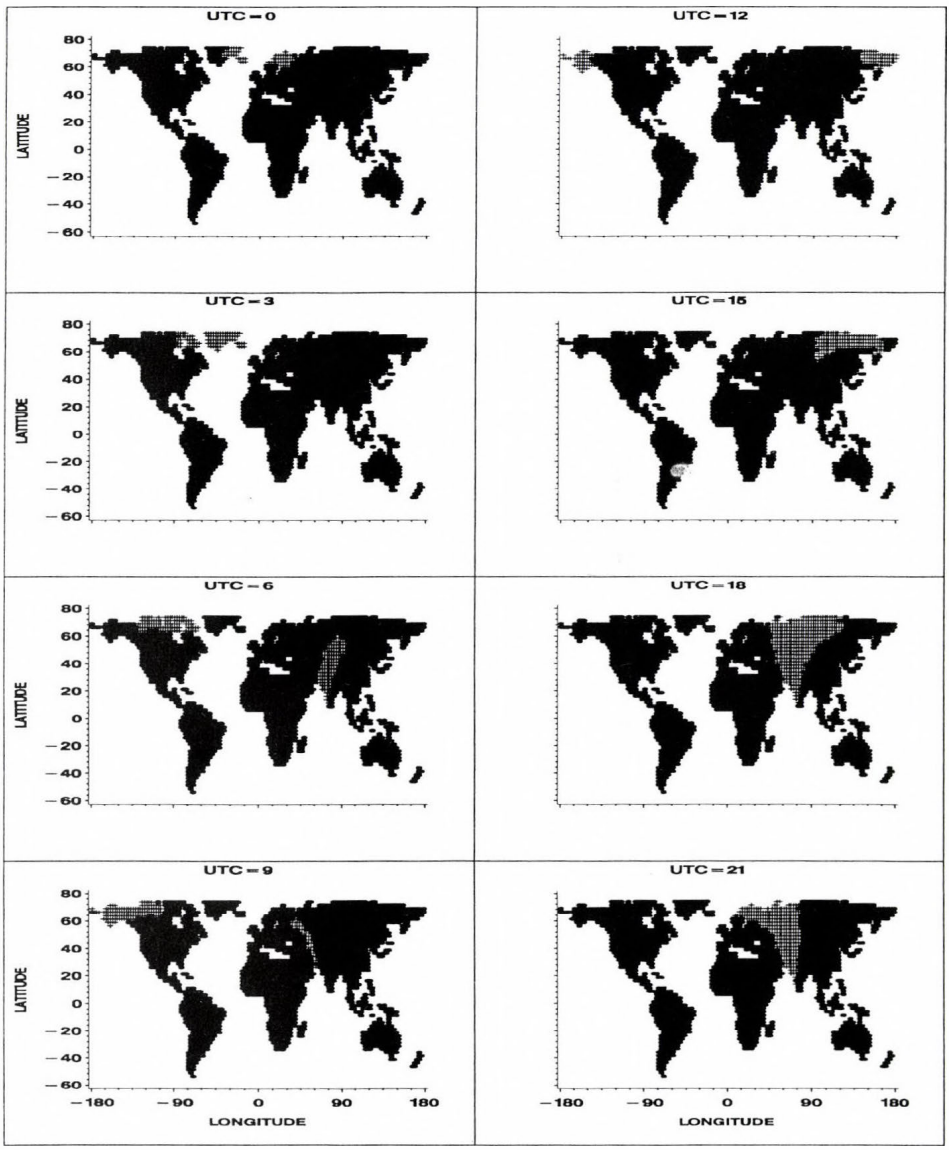

Fig. 1. Coverage of ISCCP D-2 data over land in July 1993.

While the nighttime AVHRR temperature measurements are often near the daily minimum, the daytime measurements are taken in the mid-afternoon, when the surface temperature is usually different from the daily maximum. The problem is aggravated by the orbital drift of the NOAA satellites (*Fig. 2*), which causes several hours of difference in the local time of observation over several years (*Price,* 1991). Additionally, within a given satellite orbit, there is an ~90-minute difference between the local times of observation in the mid-latitudes of the Southern and Northern hemispheres (*Fig. 3*). Thus, careful adjustment of the measurements according to the local time of observation is necessary (*Gutman,* 1999). Note that the monthly mean temperatures used here are averages of temperatures corresponding to +/–55.4° satellite scan angles, a ~2700 km wide swath and an ~1.5 hour local time difference therein. In this paper we assume that the monthly averaging compensates for these differences in daily observations and that the monthly mean characterizes the average conditions at nadir view.

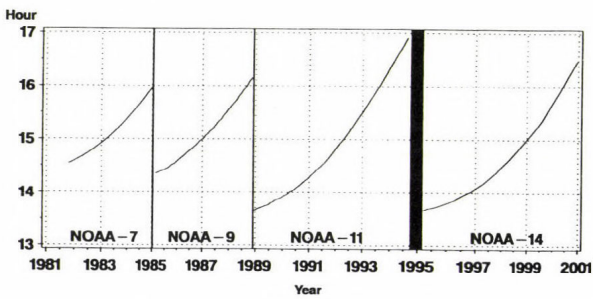

Fig. 2. Equator crossing times of the "afternoon" NOAA satellites.

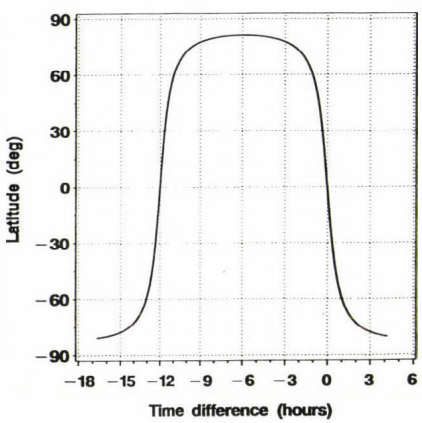

Fig. 3. Time difference between the local time of the equator crossing (ascending) and the local time of observation along a full orbit of a NOAA satellite. Note that the satellite's actual movement along its orbit corresponds to a movement along the curve from the right towards the left on this figure.

3. *Comparison of skin temperatures from ISCCP-D2 and PATMOS*

We can consider the daytime-nighttime AVHRR temperature difference as a first-order estimate of DTR and develop corrections to it using ISCCP-derived DTR as training data. The error in the AVHRR-based estimate of DTR is mainly in the decrease of the afternoon temperature with the local time of observation and thus its deviation from the daily maximum. *Fig. 4* shows the relationship between the PATMOS and ISCCP temperatures. The PATMOS daytime temperatures (*Fig. 4a*) deviate considerably from the daily maximum for high temperature values. This can be explained by the strong afternoon decrease of skin temperature in hot, mainly desert areas. The PATMOS nighttime temperatures (*Fig. 4b*), on the other hand, show good agreement with the daily minima, confirming a lower rate of temperature change in the hours before sunrise. The "daily mean temperature" from PATMOS ($[T_{sd} + T_{sn}]/2$) remains close to that derived from ISCCP daily minimum and maximum values (*Fig. 4c*), but the PATMOS "daily temperature range" ($T_{sd} - T_{sn}$; *Fig. 4d*) has a significant error for high values of DTR, driven by the high ($T_{\max} - T_{sd}$) difference.

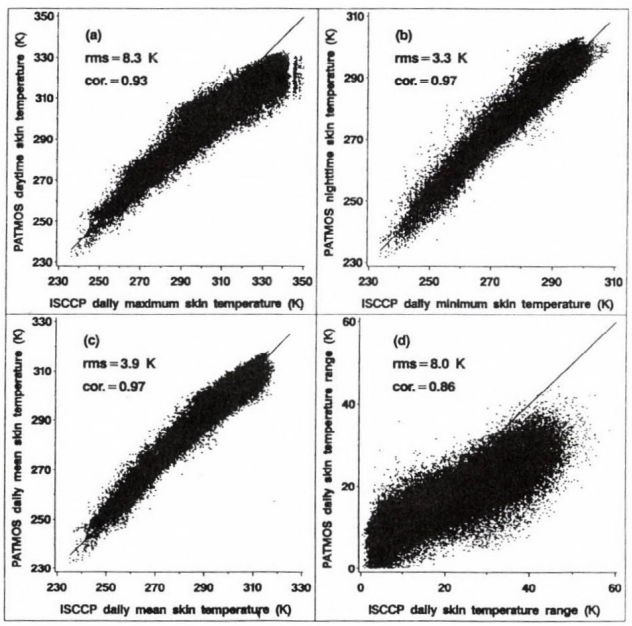

Fig. 4. Comparison of PATMOS daytime and nighttime surface skin temperatures with ISCPP daily maximum and minimum values and the daily means and daily temperature ranges derived from them.

In addition to the differences in the time of observation, some of the scatter of the data is caused by residual cloud effects inherent in both the ISCCP and PATMOS clear sky products, and by preprocessing differences, such as calibration and spatio-temporal sampling.

To analyze the compatibility of ISCCP and PATMOS surface skin temperatures, the data need to be brought to a common time of observation. This was done by selecting the ISCCP temperature values that are nearest to the actual local time of observation of the PATMOS (AVHRR) data by the following procedure:

- The equator crossing time of the NOAA satellite was determined from the year and month of the PATMOS data (Fig. 2).
- The difference between the equator crossing time and the local time of observation was calculated from the latitude of the PATMOS data, separately for the ascending (daytime) and descending (nighttime) parts of the orbit (Fig. 3).
- The actual local time of PATMOS data was calculated.
- ISCCP data corresponding to the nearest hour in local time of the PATMOS data was selected.

The results of the PATMOS-ISCCP match-up are shown in *Fig. 5*. Daytime temperatures (*Fig. 5a*) are now somewhat closer than in Fig. 4a, as the better statistics indicate. However, there is still a remarkable difference for warm temperatures, with ISCCP values systematically higher than PATMOS. This confirms that, in addition to differences in the time of observation, other factors also contribute to the ISCCP-PATMOS deviation, such as calibration differences and differences in deriving skin temperature. A significant overestimation of instantaneous AVHRR top-of-the atmosphere brightness temperatures by coincident instantaneous geostationary data has been observed in Australia (*J. Janowiak,* NOAA/CPC, 2001, personal communication) and Africa (*P. Romanov,* NOAA/NESDIS, 2001, personal communication). This suggests that of the two effects mentioned above, calibration is the more important one. In addition, this is an indication that—assuming a more reliable AVHRR calibration—the rigorous geostationary to polar orbiter (AVHRR) calibration normalization procedure within ISCCP (*Brest et al.,* 1998), may have residual errors for warm targets. Detailed analysis of the ISCCP and PATMOS infrared calibration procedures however is beyond the scope of this paper.

Nighttime temperatures, as expected, are again in good agreement. However, one still would expect some improvement in the statistics after the temporal matching of the data. But if we assume that ISCCP indeed overestimates temperatures (particularly warm ones), we should in fact expect a better

agreement between ISCCP daily minimum—with a warm bias—and PATMOS, taken a few hours before the daily minimum and thus being somewhat warmer than the daily minimum. Having just a slightly lower RMS and a somewhat lower correlation in the time-matched nighttime temperatures is thus consistent with our earlier finding; however, as the temperatures in general are lower at nighttime, the differences are not so significant as between Figs. 4a and 5a.

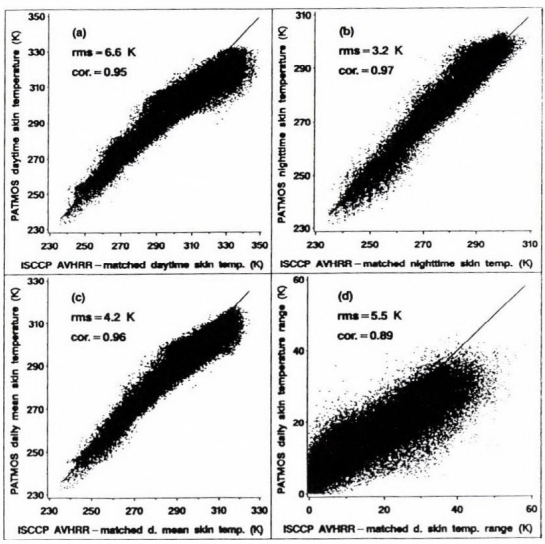

Fig. 5. Comparison of PATMOS daytime and nighttime surface skin temperatures with ISCPP temperatures corresponding to the time of the AVHRR observations within PATMOS. Daily means and daily temperature ranges are also shown.

Note that in this figure (and also in Fig. 4 for PATMOS-derived parameters) the "daily means" and "daily skin temperature ranges" are not the true values because they were not derived from daily mimima and maxima, but from temperatures at the times of the AVHRR observations in PATMOS. However, because of the temporal matching, ideally, the plots in *Figs. 5c* and *5d* now should run along the one-to-one line. But the combination of the calibration effects on daytime and nighttime data yields a slightly higher deviation of the "daily mean" values (Fig. 5c) than in Fig. 4c. The "DTR" values (Fig. 5d) show considerably better statistics than in Fig. 4d. However, the ISCCP-PATMOS difference still increases with temperature, but in a clearly more linear fashion than in Fig. 4d. This suggests that diurnal cycle effects—including their dependence on surface type and temperature—have been removed and the

residual error is mostly due to sensor calibration differences, with some scatter of the data because of incompatible cloud screening etc.

4. Summary and conclusions

Currently, the most plausible method of deriving monthly global maps of diurnal temperature range is to use monthly mean clear-sky statistics of daily maximum and minimum temperatures from ISCCP. However gaps in the spatial coverage from geostationary satellites exist particularly over the Central Asian region. To achieve a fully global coverage, ISCCP data need to be combined with other data sets, of which the AVHRR-based PATMOS appears to be the most suitable candidate.

A simple comparison of daily maximum and minimum temperatures from ISCCP, and daytime and nighttime temperatures from PATMOS has shown that there exist significant differences between them that affect DTR mapping. In general, a positive bias in ISCCP calibration for warm targets is suspected. At daytime, this calibration bias and the temperature bias caused by the later local time of the daytime AVHRR observation sum up. At nighttime, however, both effects are smaller and rather tend to cancel each other. Thus, a temporal matching of the ISCCP and PATMOS data decreases the difference at daytime and basically has no effect at nighttime. Residual calibration differences are still visible in the comparison of daytime-nighttime temperature ranges from ISCCP and PATMOS. This suggests that, in using ISCCP as a training database to derive a relationship between DTR values from PATMOS, a two-step procedure needs to be followed. First, an adjustment between ISCCP and PATMOS temperatures needs to be done (presumably rather the normalization of ISCCP to PATMOS than vice versa). Only after this step should one attempt to make adjustments for the diurnal cycle effects inherent in the PATMOS dataset.

The multi-year, monthly maps derived from PATMOS and ISCCP using the principles outlined in this paper will allow the study of the regional characteristics of the annual cycle of DTR and its inter-annual variability. Relationships between DTR and independent observations of surface characteristics (such as vegetation indices) or atmospheric effects (precipitation, cloud cover etc.) can be analyzed.

To derive higher resolution, global DTR maps, considerations need to be made for the more extensive archival and use of nighttime observations from polar orbiting satellites for land surface studies. Current efforts at NOAA and NASA in defining the future strategy of creating satellite-based climate data sets is a good opportunity to take appropriate action towards this goal.

References

Becker, F. and *Li, Z.*, 1990: Towards a local split window method over land surfaces. *Int. J. Remote. Sens. 11*, 369-393.

Brest, C.L., Rossow, W.B., and *Roiter, M.*, 1997: Update of Radiance Calibrations for ISCCP. *J. Atmos. Ocean. Tech. 14*, 1091-1109.

Czajkowski, K.P., Goward, S.N., and *Ouaidrari, H.*, 1998: Impact of AVHRR filter functions on surface temperature estimation from the split window approach. *Int. J. Remote. Sens. 19*, 2007-2012.

Desormeaux, Y., W.B. Rossow, C.L. Brest, and *C.G. Campbell*, 1993: Normalization and calibration of geostationary satellite radiances for ISCCP. *J. Atmos. Ocean. Tech. 10*, 304-325.

Eidenshink, J.C. and *Faundeen, J.L.*, 1994. The 1 km AVHRR global land data set: first stages of implementation. *Int. J. Remote. Sens. 15*, 3443-3462.

Gutman, G., 1999: On the monitoring of land surface temperatures with the NOAA/AVHRR: Removing the effect of satellite orbit drift. *Int. J. Remote Sens. 20*, 3407-3413.

Gutman, G., Tarpley, D., Ignatov, A., and *Olson, S.*, 1995: The enhanced NOAA Global Land Dataset from the Advanced Very High Resolution Radiometer. *Bull. Amer. Meteorol. Soc. 76*, 1141-1156.

Gutman, G., Elvidge, C., Csiszár I., and *Romanov, P.*, 2001: NOAA Archives of Data from Meteorological Satellites Useful for Fire Products. In *Global and Regional Fire Monitoring from Space: Planning a Coordinated International Effort* (eds.: *F. Ahern, J. Goldammer* and *C.O. Justice* (SPB Academic Publishing, The Hague, The Netherlands), pp. 257-266.

Ignatov, A. and *Gutman, G.*, 1999: Monthly mean diurnal cycles in surface temperatures over land for global climate studies. *J. Climate 12*, 1900-1910.

Rossow, W. and *Schiffer, R.*, 1991: ISCCP cloud data products. *Bull. Amer. Meteorol. Soc. 72*, 2-20.

James, M.E. and *Kalluri, S.N.V.*, 1994: The Pathfinder AVHRR land data set: an improved coarse resolution data set for terrestrial monitoring. *Int. J. Remote Sens. 15*, 3347-3363.

Kidwell, K.B. (ed.), 1998: NO*AA Polar Orbiter Data Users Guide*. U.S. Department of Commerce, National Oceanic and Atmospheric Administration, National Environmental Satellite Data and Information Service, National Climatic Data Center.

Los S.O., Justice, C.O., and *Tucker, C.J.*, 1994: A global 1°×1° NDVI data set for climate studies derived from the GIMMS continental NDVI data. *Int. J. Remote Sens. 15*, 3493-3518.

Ohring, G. and *Dodge, J.*, 1993: The NOAA/NASA Pathfinder Program. In *IRS'92: Current Problems in Atmospheric Radiation*. A. Deepak Publishing, Hampton, Virginia, USA, pp. 405-408.

Price, J.C., 1977: Thermal inertia mapping: a new view of the Earth. *J. Geophys. Res. 18*, 2582-2590.

Price, J.C., 1991: Timing of NOAA afternoon passes. *Int. J. Remote Sens. 12*, 193-198.

Rossow, W.B., Walker, A.W., Beuschel, D.E., and *Roiter, M.D.*, 1996: International Satellite Cloud Climatology Project (ISCCP). Documentation of new cloud data sets. World Meteorological Organization, World Climate Research Programme.

Schiffer, R.A. and *Rossow, W.B.*, 1983: The International Satellite Cloud Climatology Project (ISCCP): The first project of the World Climate Research program. *Bull. Amer. Meteor. Soc. 64*, 779-784.

Sellers, P.J., Meeson, B.W., Hall, F.G., Asrar, G., Murphy, R.E., Schiffer, R.A., Bretherton, F.P., Dickinson, R.E., Ellingson, R.G., Field, C.B., Huemmrich, K.F., Justice, C.O., Melack, J.M., Roulet, N.T., Schimel, D.S., and *Try, P.D.*, 1995: Remote sensing of the land surface for studies of global change: Models–algorithms–experiments. *Remote Sens. Environ. 51*, 3-26.

Stowe, L.L., Jacobowitz H., Ohring, G., Knapp K.R., and *Nalli, N.R*, 2002: The advanced very high resolution radiometer pathfinder atmosphere (PATMOS). Data set. *J. Climate*, in press.

IDŐJÁRÁS

Quarterly Journal of the Hungarian Meteorological Service
Vol. 105, No. 4 — Vol. 106, No. 1, October 2001 — March 2002, pp. 265-278

Observations of three-dimensional radiative effects that influence satellite retrievals of cloud properties

Tamás Várnai[1] and **Alexander Marshak**

Joint Center for Earth Systems Technology of University of Maryland, Baltimore County, and NASA Goddard Space Flight Center

(Manuscript received October 5, 2001; in final form November 27, 2001)

Abstract—This paper examines three-dimensional (3D) radiative effects, which arise from horizontal radiative interactions between areas that have different cloud properties. Earlier studies have argued that these effects can cause significant uncertainties in current satellite retrievals of cloud properties, because the retrievals rely on one-dimensional (1D) theory and do not consider the effects of horizontal changes in cloud properties. This study addresses two questions: which retrieved cloud properties are influenced by 3D radiative effects, and where 3D effects tend to occur. The influence of 3D effects is detected from the way side illumination and shadowing make clouds appear asymmetric: Areas appear brighter if the cloud top surface is tilted toward, rather than away from, the sun. The analysis of 30 images by the Moderate Resolution Imaging Spectroradiometer (MODIS) reveals that retrievals of cloud optical thickness and cloud water content are most influenced by 3D effects, whereas retrievals of cloud particle size are much less affected. The results also indicate that while 3D effects are strongest at cloud edges, cloud top variability in cloud interiors, even in overcast regions, also produces considerable 3D effects. Finally, significant 3D effects are found in a wide variety of situations, ranging from thin clouds to thick ones and from low clouds to high ones.

Key-words: satellite, solar radiation, cloud property retrievals, inhomogeneous clouds

1. Introduction

Satellite measurements are often used to infer various cloud properties, such as the clouds' water content or particle size. Currently, the calculations assume that when a satellite measures the solar radiation reflected from a particular area of a cloud, the characteristics of this radiation are shaped by the cloud

[1] *Corresponding author address:* Tamás Várnai, Code 913, NASA GSFC, Greenbelt, MD 20771, USA. E-mail: varnai@climate.gsfc.nasa.gov

properties in that area only. In other words, the calculations rely on one-dimensional (1D) radiative transfer theory: They interpret the radiances measured at a particular pixel by assuming that the pixel's surroundings have identical cloud properties, with no changes in horizontal directions. This approach has the advantage of allowing an unambiguous interpretation of the measured radiance values, leading to a single set of estimated cloud properties. In contrast, if the full three-dimensional (3D) radiative transfer were considered (including horizontal interactions between areas that have different cloud properties), the radiances measured at a pixel could correspond to a variety of cloud properties: For example, a thin cloud could be as bright as a thicker cloud that was shaded by an even thicker cloud.

Since the mid-1980s, numerous theoretical studies have indicated that the 1D approximation can cause significant errors in satellite retrievals and that 3D radiative effects must also be considered (e.g., *Davies,* 1984; *Kobayashi,* 1993; *Barker* and *Liu,* 1995). Simulation results have indicated that, depending on the circumstances, 1D retrievals can yield clouds that are too thin or too thick, too rough or too smooth, artificially anisotropic, and asymmetric (e.g., *Marshak et al.,* 1995; *Zuidema* and *Evans,* 1998; *Várnai,* 2000). Unfortunately, detecting the influence of 3D effects in actual observations has proven to be a much more elusive task, mainly because of the difficulties in separating the influence of 3D effects from uncertainties in other factors, such as variations in cloud droplet size. The lack of observational evidence made it difficult to tell whether the 3D effects suggested by theoretical results really occur in the atmosphere. The main question has been not whether 3D radiative processes are calculated correctly for the clouds considered in theoretical studies, but whether the simulated clouds have realistic horizontal variability.

The first unambiguous observations of 3D effects emerged in the mid-1990s. First, several studies examining 30 m–resolution Landsat images found that for high sun, the diffusion of radiation inside clouds smoothes out small-scale variability—and so clouds appear more homogeneous than they really are (*Marshak et al.,* 1995; *Davis et al.,* 1997; *Oreopoulos et al.*, 2000). Around the same time, the statistical analysis of satellite data at resolutions ranging from 1 km to 30 km revealed that 3D effects make clouds appear too thick when the sun is very oblique (*Loeb* and *Davies*, 1996; *Loeb* and *Coakley*, 1998). In addition, new multiangle satellite measurements revealed that cloud reflection into forward oblique view directions is smaller than expected from 1D theory—and that the reduction can be caused by 3D effects (*Buriez et al.*, 2001; *Ákos Horváth, Iliana Genkova* and *Roger Davies,* 2001, personal communication). Most recently, *Várnai* and *Marshak* (2002) found a clear signal of 3D effects for moderately oblique solar illumination: Side illumination and shadowing effects make clouds appear asymmetric, as if clouds were brighter

and thicker on their side facing the sun than on the opposite side. This effect makes it more difficult to combine the satellite data with ground-based or airborne measurements on a pixel-by-pixel basis, distorts the histogram of retrieved cloud properties, and makes clouds appear rougher than they really are. On the positive side, theoretical simulations by *Várnai* and *Marshak* (2002) indicated that the observed asymmetry is closely related to the way 3D effects change the average cloud reflection of large areas—which suggests that one can use the observed asymmetry values to estimate the large-scale retrieval biases due to 3D effects.

The goal of this paper is to analyze observations of apparent cloud asymmetry in order to gain new insights into 3D radiative effects. First, Section 2 describes the satellite data used in this study and briefly discusses how the apparent cloud asymmetry is determined from the observations. Section 3 then analyzes the observations to see which retrieved cloud properties are influenced by 3D effects and to better understand in which clouds 3D effects tend to occur. Finally Section 4 offers a brief summary and a few concluding remarks.

2. Data and methodology

2.1 Satellite data used

This study uses measurements by the Moderate Resolution Imaging Spectroradiometer (MODIS) instrument on board the Terra satellite. Terra was launched on a polar sun-synchronous orbit in December 1999, and it orbits the Earth in 98 minutes with a 10:30 a.m. equatorial crossing time at a 705 km altitude. MODIS is a precursor instrument to the next generation of imagers that will replace the Advanced Very High Resolution Radiometers (AVHRR) on the operational polar-orbiting satellites of the National Oceanic and Atmospheric Administration (NOAA). MODIS takes measurements at 36 wavelengths ranging from 0.4 to 14.4 μm. The spatial resolution at the subsatellite point is 250 m, 500 m, or 1 km, depending on the wavelength. This study uses 1 km resolution data from two wavelengths, 0.86 μm and 11 μm. The 0.86 μm radiances are converted to reflectances (R) using the equation

$$R = \frac{\pi \cdot I}{\cos\Theta_0 \cdot F_0}, \tag{1}$$

where I is the radiance, Θ_0 is the solar zenith angle, and F_0 is the solar constant. The 11 μm radiances are transformed into equivalent brightness temperature values using the Planck formula (e.g., *Thomas* and *Stamnes*, 1999, p. 94).

Although AVHRR and other instruments also offer measurements at similar wavelengths, MODIS is particularly well suited for this study because of its high radiometric accuracy. Especially important is the sensitivity at 11 μm, because observations of small temperature changes are crucial for the adopted methodology. (MODIS images report temperature changes as small as 0.01 K, and the noise equivalent temperature difference is around 0.05 K (*NASA*, 2000).)

In addition to using radiance measurements, this study also uses some standard MODIS products freely available at *http://daac.gsfc.nasa.gov-/CAMPAIGN_DOCS/MODIS/index.shtml*. In particular, we used the 1 km-resolution cloud optical thickness, cloud water path, and cloud particle size data; the 5 km-resolution land-water mask; and the solar and viewing zenith and azimuth angles.

MODIS data are distributed in approximately 2000 km by 2000 km segments called granules. This study used the central 450 km-wide portion of 30 granules, where the viewing zenith angle is less than 20°. This restriction eliminates potential difficulties that could arise for oblique views, such as areas being viewed twice or pixel sizes increasing. The 30 granules were taken from three days separated by 10-day intervals: May 14, May 25, and June 4, 2001. The 10-day separation ensures that the images are relatively independent from each other, because the weather systems observed on one day are not likely to still exist 10 days later. Ten granules were taken from each day—essentially all granules that satisfy the following two criteria. First, the central portion of the granule should cover mostly oceanic areas. This is helpful because cloud detection and cloud property retrievals are easier and more accurate over ocean than over land. Second, the sun should be moderately oblique, with solar zenith angles around 60°. (Due to the large size of MODIS images, the actual zenith angles vary between 45° and 75°, but they remain close to 60° most of the time.) Because of the Terra satellite's sun-synchronous orbit, this requirement implies that all granules are around 35°S latitude. Let us note that the images are from a similar season and latitude band as in *Várnai* and *Marshak* (2002)—which used images from November 2000 around 40°N latitude—but from the southern hemisphere. The specific granules used in this study are listed in *Table 1*.

Table 1. Dates and UTC times (hour:minute) that identify the granules used in this study

Date	Time
May 14, 2001	03:20, 05:00, 06:40, 09:55, 11:35, 16:30, 18:10, 19:50, 21:30, 23:05
May 25, 2001	01:25, 03:00, 04:40, 08:00, 11:15, 12:55, 17:50, 19:30, 21:10, 22:50
June 4, 2001	05:15, 06:55, 08:35, 10:15, 13:30, 15:10, 16:50, 18:30, 21:45, 23:25

2.2 *Calculation of the apparent cloud asymmetry*

This study follows the methodology described in *Várnai* and *Marshak* (2002). The method's basic assumption is that if the cloud top surface is not horizontal (as assumed in 1D theory), 3D radiative effects make pixels brighter or darker than they would be in 1D theory. The brightening or darkening is expected to come from changes in the solar illumination, depending on whether the cloud top is tilted toward or away from the sun. For any given (1 km)^2 cloudy pixel—for which the operational MODIS data processing retrieved a nonzero cloud optical thickness—the direction of the cloud slope is determined in two steps. First, Step 1 determines which two neighboring pixels in front and behind are closest to the solar azimuth. Step 2 then compares the 11 μm brightness temperatures (T) of these two neighbors. Because temperature tends to decrease with altitude, Step 2 declares that our pixel is on a slope tilted toward the sun if $T_{\text{front}} > T_{\text{behind}}$ and that it is on a slope tilted away from the sun if $T_{\text{front}} < T_{\text{behind}}$. Following *Várnai* and *Marshak* (2002), the two kinds of pixels will be identified as *illuminated* (subscript *i*) or *shadowy* (subscript *s*), even though no actual shadows are required for a pixel to be designated as shadowy.

Let us note that this designation can be made for pixels at local temperature minima and maxima as well, and even for pixels at cloud edges. The only exception is if both the neighbors in front and behind are cloud free—that is, if a single pixel contains both the illuminated and shadowy sides of a cloud. For such "isolated" pixels, the relationship between T_{front} and T_{behind} has much more to do with conditions at ground level than at the cloud top—and so these pixels are not considered in our calculations. Fortunately, such isolated pixels occur quite rarely: In the examined scenes, fewer than 2% of all cloudy pixels fall into this category.

Once all cloudy (1 km)^2 pixels in a (50 km)^2 area are designated as either illuminated or shadowy, the method compares the mean cloud properties of all illuminated pixels to the mean properties of all shadowy pixels. If the two mean values are close to each other, this indicates that 3D effects do not make much of a difference. If, however, there are large differences (e.g., if illuminated pixels are much brighter than shadowy pixels), then 3D effects are expected to be strong.

The approach described above assumes that the solar azimuth does not influence cloud development, and so the illuminated and shadowy slopes have statistically similar true cloud properties. One can argue that if 3D radiative effects did influence cloud development, the most likely consequence would be the enhancement and reduction in absorption at illuminated and shadowy slopes, respectively. This would make clouds geometrically asymmetric by making the buoyancy conditions different on the opposite clouds sides. The re-

sulting asymmetries in cloud top altitude should then make the brightness temperature fields asymmetric as well. *Fig. 1*, however, indicates that the brightness temperatures of illuminated and shadowy slopes are statistically identical, which suggests that 3D effects did not have a strong influence on the vertical growth of clouds. (Another possible consequence of 3D effects would be that the enhanced absorption in illuminated slopes could reduce droplet size through increased evaporation. Section 3, however, will show that this effect is not very large either.) Naturally, random processes (such as wind shear or the overlap of two cloud layers) can make clouds asymmetric in any particular area, but these effects should even out when a large number of areas are considered. As a result, if we see that the illuminated portions of (50 km)^2 areas are systematically brighter than their shadowy portions, 3D effects must be responsible for the systematic difference.

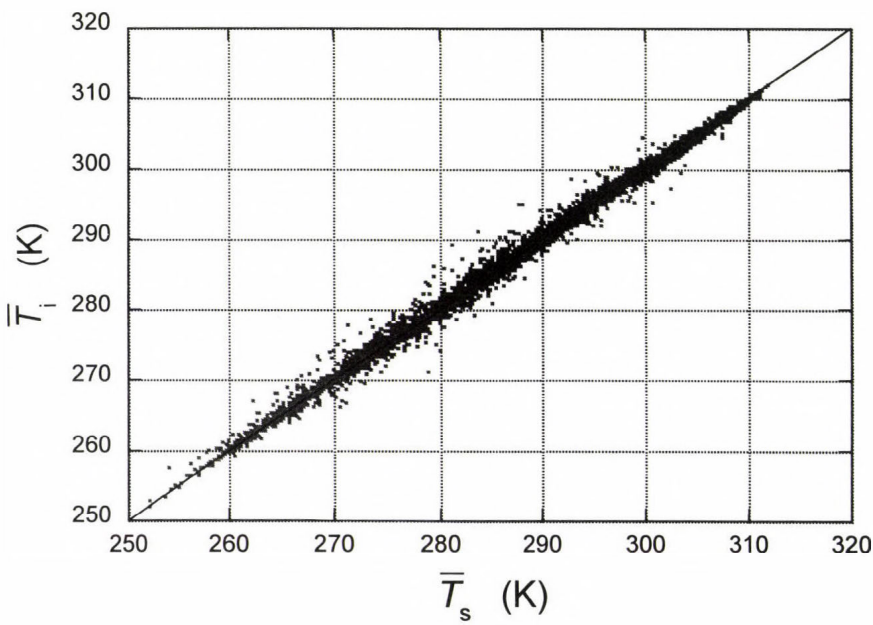

Fig. 1. Comparison of the mean brightness temperatures of illuminated $(\overline{T}_i)$ and shadowy $(\overline{T}_s)$ pixels. The overbar indicates averaging over (50 km)^2 areas, and so each point represents the mean values for a (50 km)^2 area. All figures are based on the 9410 areas in the examined 30 MODIS scenes that have a cloud coverage larger than 10%. (Areas with cloud coverage below 10% were not considered because of the large statistical uncertainties that may arise for them.)

3. *Observations of 3D radiative effects*

3.1 Analysis of 3D effects in retrievals of various cloud properties

Fig. 2 compares the 0.86 μm reflectances observed at illuminated and shadowy slopes. The figure clearly indicates that 3D effects are important in the examined scenes; the illuminated slopes are much brighter then the shadowy slopes. This intuitive tendency is in clear contrast to the behavior of 11 μm brightness temperatures in Fig. 1.

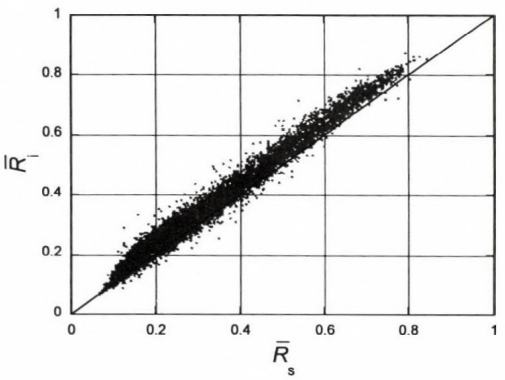

Fig. 2. Comparison of the mean 0.86 μm reflectances of illuminated $(\bar{R}_i)$ and shadowy $(\bar{R}_s)$ portions of (50 km)^2 areas.

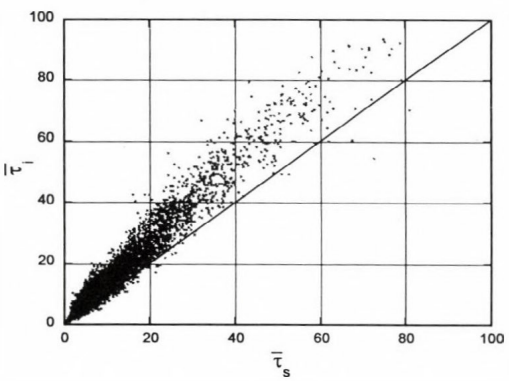

Fig. 3. Comparison of mean optical thicknesses retrieved at the illuminated $(\bar{\tau}_i)$ and shadowy $(\bar{\tau}_s)$ portions of (50 km)^2 areas.

Fig. 3 shows that the 3D effects in Fig. 2 have a strong influence on optical thickness (τ) retrievals, which estimate much larger τ values at slopes tilted toward the sun. It is interesting to note that the asymmetries in Fig. 3 are about twice as strong as in *Várnai* and *Marshak* (2002): The median relative

difference between $\bar{\tau}_i$ and $\bar{\tau}_s$ is 26%, as opposed to the 13% in the earlier study. (The mean relative difference is 28%.) The discrepancy is probably related to differences in the distribution of cloud types in the two studies: Flat stratiform clouds that are close to the 1D ideal appear to be more frequent around 40°N in November (in the earlier study), whereas the bumpier convective clouds that cause stronger 3D effects are more frequent around 35°S in May (in this study). The differences indicate large regional or interannual variations in 3D radiative effects, and they highlight the need for comprehensive studies on the climatological distribution of 3D effects.

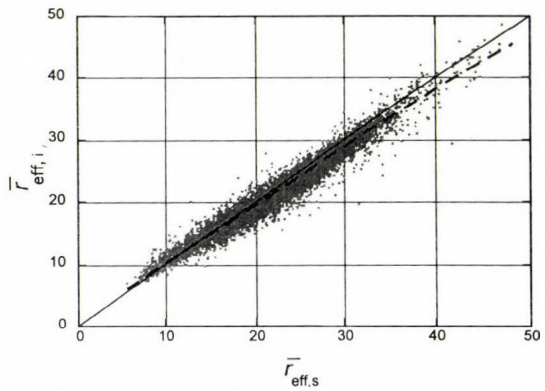

Fig. 4. Comparison of mean effective particle radii retrieved at the illuminated $(\bar{r}_{eff,i})$ and shadowy $(\bar{r}_{eff,s})$ portions of (50 km)^2 areas. The dashed line indicates a linear fit to the data.

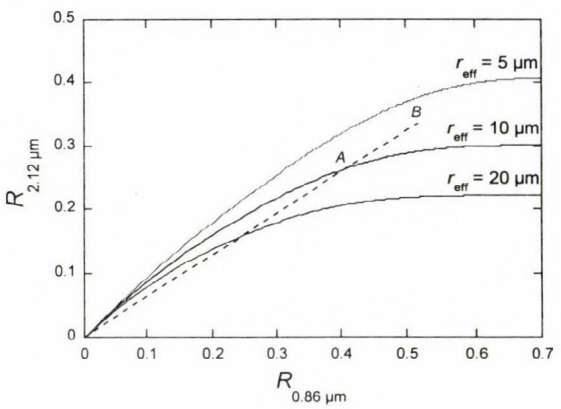

Fig. 5. Illustration of the concept of 1D effective particle radius retrievals. The figure displays the relationship between nadir cloud reflectances at 0.86 μm and 2.12 μm, which was calculated using 1D theory for three different droplet sizes. The sample calculations are for 60° solar zenith angle, completely transparent cloud-free air, and nonreflecting surface.

Fig. 4 indicates that retrievals of the effective particle size (r_{eff}) are influenced much less than, and in the opposite direction from, τ retrievals. The main reason for the opposite behavior is illustrated in *Fig. 5*, which depicts the

way particle size is retrieved from pairs of reflectance measurements at 0.86 and 2.12 μm. The retrievals use the algorithm of *Nakajima* and *King* (1990) to take advantage of the fact that absorption, and hence reflectance, depend strongly on droplet size. To explain the asymmetry in Fig. 4, let us assume that if 3D effects enhance the illumination of a pixel on an illuminated slope by a certain percentage, the 0.86 and 2.12 μm reflectances increase by a similar percentage. For example, if the true properties of the pixel put it at point *A* in Fig. 5 according to 1D theory, side illumination moves it to point *B* along the dashed line. The enhanced 2.12 μm reflectance is then interpreted by the 1D retrievals as if cloud absorption were smaller, that is, as if cloud droplets were smaller. On shadowy slopes the retrievals make the opposite error, thinking that the droplets are larger there. This overestimation of droplet size is further strengthened by the fact that absorption allows less 2.12 μm than 0.86 μm radiation to flow from the illuminated to the shadowy side inside the clouds, and so the 2.12 μm reflectance is actually reduced by a larger percentage than the 0.86 μm reflectance in shadowy slopes.

An additional factor contributing to the trend in Fig. 4 may be that—as mentioned in Section 2.2—the enhanced absorption at illuminated slopes strengthens the local radiative heating, and this increase weakens the condensational growth of cloud droplets on these slopes. Because, however, the combined effect of all these factors is quite small (about 1 to 2 μm), neither one of the contributing factors appears to be particularly strong.

After retrieving τ and r_{eff}, the operational MODIS data processing uses the results to calculate the clouds' water content (water path, or WP) from the equation

$$WP = \frac{2}{3} \rho \cdot \tau \cdot r_{\text{eff}} , \tag{2}$$

where ρ is the density of water (*King et al.*, 1997). Since Figs. 3 and 4 show that 3D effects have a much stronger influence on retrievals of τ than of r_{eff}, it is not surprising that the water path—which is a product of τ and r_{eff}—shows a behavior similar to that of τ (*Fig. 6*). The median relative difference between the water path of illuminated and shadowy slopes is 23%.

Because theoretical simulations in *Várnai* and *Marshak* (2002) indicated that the observed asymmetries are closely related to the area-averaged biases caused by 3D effects, we can conclude that the results discussed above indicate that 3D effects introduce the largest errors in retrievals of τ and *WP*, whereas the retrievals of r_{eff} are much less affected.

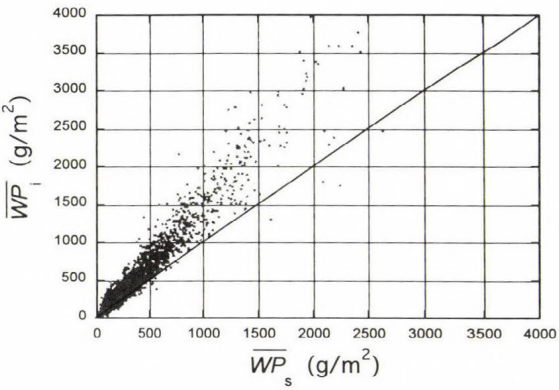

Fig. 6. Comparison of mean water paths retrieved at the illuminated $\left(\overline{WP_i}\right)$ and shadowy $\left(\overline{WP_s}\right)$ portions of (50 km)^2 areas.

3.2 Examination of where 3D radiative effects occur

Although the possibility of random asymmetries in true cloud properties prevents our technique from locating 3D radiative effects on a pixel-by-pixel basis, the technique can nevertheless yield valuable statistical information on where 3D effects tend to occur. One important question is whether 3D radiative effects are limited to some specific situations, or whether they occur under a wide range of circumstances. To address this question, *Fig. 7* plots the relative difference between the (50 km)^2 average water path values retrieved for illuminated and shadowy pixels, as a function of the mean optical thickness of the (50 km)^2 areas. The figure indicates that the relative difference increases rapidly until about $\tau \approx 5$, as multiple scattering (essential for any 3D effects) becomes more and more important. Once cloud reflection gets dominated by multiple scattering, however, the relative differences remain fairly constant. On one hand, this means that the absolute magnitude of 3D effects increases with cloud reflectance. On the other hand, the results reveal that clouds in a wide range of optical thicknesses are similarly effective in causing 3D radiative effects.

One can also use the available data to examine how 3D effects depend on cloud altitude. For this, *Fig. 8* displays the overall average water path of all (1 km)^2 illuminated and shadowy pixels (combined over all 30 scenes) as a function of cloud top pressure. (This pressure value is reported in the operational MODIS cloud product.) The figure reveals that average cloud thickness tends to increase with altitude—which is consistent with the idea that convective clouds contain more water as they grow taller. Although the absolute magnitude of 3D effects ($WP_i - WP_s$) increases with altitude accordingly, the inset reveals that clouds in a wide range of altitudes are similarly effective in creating strong 3D effects and that low-level clouds in the boundary layer are the most effective ones.

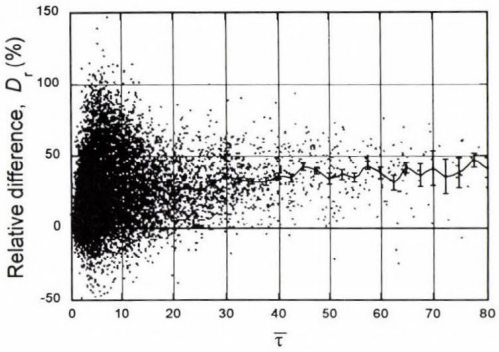

Fig. 7. Dependence of 3D effects on the (50 km)^2 average cloud optical thickness. The relative difference (D_r) is calculated as $D_r = \frac{\left(\overline{WP_i} - \overline{WP_s}\right)}{\left(\frac{\overline{WP_i} + \overline{WP_s}}{2}\right)} \cdot 100\%$. The solid line shows the local mean values at τ–steps of 2.5, and the error bars indicate the uncertainty of these mean values.

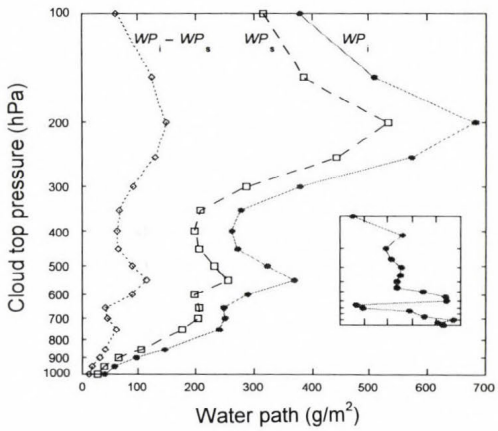

Fig. 8. Dependence of the overall average water path of illuminated (WP_i) and shadowy (WP_s) pixels on cloud top pressure. The dotted line indicates the difference $WP_i - WP_s$. The inset shows the overall average relative difference calculated as $\frac{\left(WP_i - WP_s\right)}{\left(\frac{WP_i + WP_s}{2}\right)} \cdot 100\%$ using all cloudy pixels in each cloud top pressure interval.

Finally, let us examine how 3D effects depend on cloud brokenness. For this, *Fig. 9* plots the relative difference between the area average values for WP_i and WP_s as a function of the cloud coverage in (50 km)^2 areas. Although the cloud coverage is not a very good indicator of cloud brokenness (for example, 50% cloud coverage can occur not only in truly broken scenes, but also at the edges of large overcast cloud fields), the figure has two interesting features: It shows that 3D effects are quite important even in overcast scenes and that 3D effects become even stronger in broken clouds. These results suggest that cloud edges may be more effective than areas inside the cloud at creating 3D effects, but cloud top variations are also very important. These conclusions are confirmed clearly in *Fig. 10*, which displays the difference between the overall average WP_i and WP_s values (combined over all 30 scenes) as a function of the cloudy pixels' distance to the closest cloud-free pixel. As expected, the differences are largest right at the cloud edges, but they remain significant even in the interior of clouds.

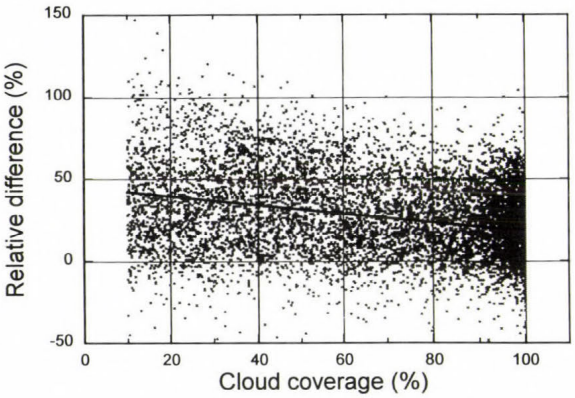

Fig. 9. Dependence of D_r values (defined at Fig. 7) on the cloud over of (50 km)^2 areas.

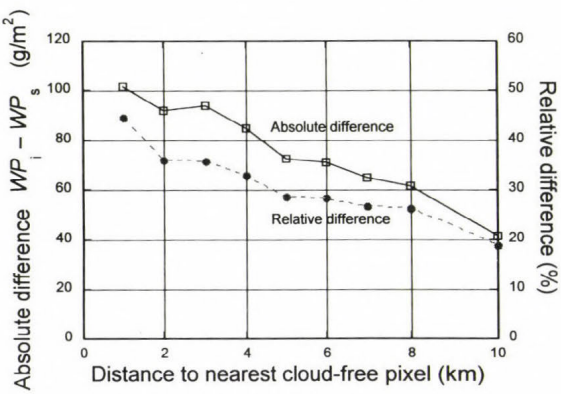

Fig. 10. Dependence of the illuminated-shadowy differences on the distance to the nearest cloud-free pixel. The relative difference is calculated as in Figs. 7 and 8, but combining all (1 km)^2 pixels in all 30 examined scenes (instead of combining only pixels in individual (50 km)^2 areas). The values displayed at a distance of 10 km represent the results for all distances greater than 8 km.

4. Summary

This study examined three-dimensional (3D) radiative effects, which arise from horizontal radiative interactions between areas that have different cloud properties. Current methods of retrieving cloud properties from satellite measurements do not consider these effects, because the retrievals rely on one-dimensional (1D) radiative transfer theory—that is, they treat each pixel as if it were surrounded by identical pixels, without any changes in horizontal directions. Although the 1D approximation has the advantage of allowing an unambiguous interpretation of the radiances measured at a given pixel, numerous studies have argued that not considering 3D effects can cause problems in the retrievals. This paper focused on two particular questions: which retrieved cloud properties are most influenced by 3D radiative effects, and where 3D effects tend to occur.

To address these questions, the study examined 30 images, 2000 km by 450 km each, by the Moderate Resolution Imaging Spectroradiometer (MODIS), which were taken in May and June 2001 over oceans around 35°S latitude. The images were analyzed using the method proposed in *Várnai* and *Marshak* (2002). The method's basic idea is that if 3D effects are present in a scene, they make areas tilted toward the sun better illuminated—and consequently brighter—than the areas tilted away from the sun. This can result in systematic differences between the two kinds of areas, causing systematic asymmetries in the retrieved cloud properties. Thus, the method examines 3D effects by first estimating the tilt of cloud top surfaces from thermal infrared images, and then comparing the cloud properties retrieved for the two kinds of slopes.

The results revealed that 3D effects cause quite large uncertainties in the retrievals of cloud optical thickness and cloud water path: The median (and mean) difference between the values retrieved for areas tilted toward and away from the sun was about 25%. This result highlights that there are large regional differences in the importance of 3D effects, because, when *Várnai* and *Marshak* (2002) examined optical thickness fields, they found 3D effects only about half this strong in a similar season and latitude band in the northern hemisphere. In contrast, the present study found cloud particle size retrievals to be much less influenced by 3D effects: On average, droplet sizes were only about 1 to 2 μm larger on slopes that are tilted away, rather than toward, the sun.

The results also revealed that 3D radiative effects are not limited to some narrow range of situations or cloud types, because 3D effects remained significant over a wide range of cloud thicknesses and cloud top altitudes.

Finally, the results showed that although cloud edges are most effective in causing 3D radiative effects, cloud top variability is nearly as important. Consequently, 3D effects were found to be strongest in broken clouds, but they were quite significant even in large overcast regions.

Overall, the results highlight that the 1D approximation is a significant limitation in current techniques that retrieve cloud properties from shortwave satellite measurements. Because the simulation results of *Várnai* and *Marshak* (2002) indicate that the observed consequence of 3D radiative interactions (the apparent cloud asymmetry) is closely related to other consequences of 3D effects, the presented results have implications for a wide range of issues, from the interpretation of satellite measurements to the modeling of photochemical processes. The abundance of 3D effects indicates that radiative transfer in cloudy atmospheres is an inherently 3D process, and it highlights the need for new radiative transfer models that can move beyond the 1D framework both in remote sensing and in other applications involving radiative transfer calculations.

Acknowledgments—We appreciate funding for this research from the NASA EOS Project Science Office (under Grant NAG5-6675) and support from project scientist David O'C. Starr. We also thank Laura L. Atwood for proofreading the manuscript and providing helpful suggestions.

* * *

I am very happy to be able to contribute to this special issue honoring *Dr. Major*. I am deeply grateful to him for his support throughout my years at the Hungarian Meteorological Service, and for his help when I applied to graduate school.

Tamás Várnai

References

Barker, H.W., and *Liu, D.*, 1995: Inferring optical depth of broken clouds from Landsat data. *J. Climate 8*, 2620–2630.

Buriez, J.-C., Dutriaux-Biucher, M., Parol, F., and *Loeb, N.G.*, 2001: Angular variability of the liquid water cloud optical thickness retrieved from ADEOS–POLDER. *J. Atmos. Sci. 58*, 3007-3018.

Davies, R., 1984: Reflected solar radiances from broken cloud scenes and the interpretation of satellite measurements. *J. Geophys. Res. 89*, 1259–1266.

Davis, A., Marshak, A., Cahalan, R., and *Wiscombe, W.*, 1997: The Landsat scale-break in stratocumulus as a three-dimensional radiative transfer effect, implications for cloud remote sensing. *J. Atmos. Sci. 54*, 241–260.

King, M.D., Tsay, S.-C., Platnick, S., Wang, M., and *Liou, K.-N.*, 1997: *Cloud retrieval algorithms for MODIS: Optical thickness, effective particle radius, and thermodynamic phase.* MODIS Algorithm Theoretical Basis Document No. ATBD-MOD–05, Version 5, NASA.

Kobayashi, T., 1993: Effects due to cloud geometry on biases in the albedo derived from radiance measurements. *J. Climate 6*, 120–128.

Loeb, N. G., and *Davies, R.*, 1996: Observational evidence of plane parallel model biases: Apparent dependence of cloud optical depth on solar zenith angle. *J. Geophys. Res. 101*, 1621–1634.

Loeb, N.G., and *Coakley, J. A.*, 1998: Inference of marine stratus cloud optical depths from satellite measurements: Does 1D theory apply? *J. Climate 11*, 215–233.

Marshak, A., Davis, A., Wiscombe, W., and *Cahalan, R.*, 1995: Radiative smoothing in fractal clouds. *J. Geophys. Res. 100*, 26,247–26,261.

Nakajima, T.Y., and *King, M.D.*, 1990: Determination of the optical thickness and effective radius of clouds from reflected solar radiation measurements. Part I: Theory. *J. Atmos. Sci. 47*, 1878–1893.

NASA, 2000: *MODIS—Moderate Resolution Imaging Spectroradiometer*. Available from http://modarch.gsfc.nasa.gov/MODIS/INSTRUMENT/modis_brochure.pdf

Oreopoulos, L., Marshak, R., Cahalan, F., and *Wen, G.*, 2000: Cloud 3D effects evidenced in Landsat spatial power spectra and autocorrelation functions. *J. Geophys. Res. 105*, 14,777–14,788.

Thomas, G.E., and *Stamnes, K.*, 1999: *Radiative Transfer in the Atmosphere and in the Ocean.* Cambridge University Press, 517 pp.

Várnai, T., 2000: Influence of three-dimensional radiative effects on the spatial distribution of shortwave cloud reflection. *J. Atmos. Sci. 57*, 216–229.

Várnai, T., and *Marshak, A.*, 2002: Observations of three-dimensional radiative effects that influence MODIS cloud optical thickness retrievals. *J. Atmos. Sci.*, in press.

Zuidema, P., and *Evans, K.F.*, 1998: On the validity of the Independent Pixel Approximation for the boundary layer clouds observed during ASTEX. *J. Geophys. Res. 103*, 6059–6074.

IDŐJÁRÁS

Quarterly Journal of the Hungarian Meteorological Service
Vol. 105, No. 4 — Vol. 106, No. 1, October 2001 — March 2002, pp. 279-291

Operative cloud classification using Meteosat images

Márta Diószeghy

Hungarian Meteorological Service, Satellite Research Laboratory,
P.O. Box 39, H-1675 Budapest, Hungary
E-mail: dioszeghy.m@met.hu

(Manuscript received November 19, 2001; in final form January 31, 2002)

Abstract—Satellite based cloud information is an essential input for the nowcasting system recently developed at the Hungarian Meteorological Service (HMS). This paper describes the cloud classification method used operationally for half-hourly Meteosat images. It was worked out in frame of a co-operation between HMS and Météo-France. A pixel by pixel algorithm is applied using auxiliary data as well such as the actual surface temperature and surface reflectivity. For the classification we use the results of the test runs of clustering type cloud classification methods earlier developed by Météo-France and by HMS separately. The monthly averaged kernels of those clusters are actualized as functions of the surface parameters pixel by pixel and images are classified according to these actual kernels. Verification was made by the forecasters of HMS. We also examined the possibility of applying the method for filtering noisy radar images. The results of a special study comparing the radar and satellite based cloud top height values according to cloud types gave new considerations for the development of the cloud classification method as well.

Key-words: cloud classification, Meteosat, nowcasting, satellite meteorology

1. Introduction

Cloud parameters extracted from satellite imagery became more and more important in the last years at the Hungarian Meteorological Service (HMS) as lots of the synoptic stations were changed for automatic weather stations with less detailed cloud representation. At the Satellite Research Laboratory of HMS we have access for half-hourly images of the geostationary Meteosat and also the AVHRR (Advanced Very High Resolution Radiometer) images of the polar orbiting NOAA (National Oceanic and Atmospheric Administration) satellites 4–6 times a day. The different spatial and spectral resolutions result in different

approaches for deriving cloud parameters. Usually threshold techniques are used for multi-channel NOAA/AVHRR images while statistical or combined methods with auxiliary data for the present geostationary satellite of Europe, the Meteosat-7. The geostationary GOES satellites of the United States have more channels, therefore threshold techniques can be effective for those images. The launch of Meteosat Second Generation (MSG) is planned for July 2002. It will have 12 channels compared to the present 3 of Meteosat, with 15 min time resolution and 3 km spatial resolution in most of the channels. There is a possibility to develop methods for MSG with the help of the already available GOES or NOAA/AVHRR data. International efforts are focusing to develop such algorithms (e.g., *Derrien* and *Le Gléau*, 1999). NOAA/AVHRR based fog and cloud detection has already been worked out at HMS as well (*Putsay*, 2001), and the results are available operationally for the forecasters. We will use this algorithm for MSG but until then for nowcasting and very short range forecasting, where the good temporal resolution of images is essential, we have to use Meteosat cloud parameters.

An automatic nowcasting system (MEANDER: Mesoscale Analysis Nowcasting and Decision Routines) has been worked out recently at the Hungarian Meteorological Service (*Geresdi* and *Horváth*, 2000). The analysis runs operationally since the end of 1999, while the nowcasting for 3 hours in 15 min time steps is pre-operational since summer 2001. The scheme makes use of most of the available data like radiosonde, synop and automatic weather station measurements, mesoscale numerical model outputs, radar and satellite images and lightning data. All raw data are interpolated and derived fields are calculated on the nowcasting grid. Decision trees have been defined to derive "present weather codes" and other complex parameters for the grid points. Meteosat derived cloud parameters like cloudiness, cloud top height and cloud types are among the most important elements of the system (*Diószeghy et al.*, 1999).

This paper focuses on Meteosat cloud classification as one of the operational procedures of the nowcasting scheme. The cloud classification program package separates and determines the different cloud types on the images. The algorithm was developed in frame of a co-operation with Météo-France, CMS, Lannion (*Brisson et al.*, 1997).

Earlier clustering type automatic cloud classification from Meteosat imagery had been developed at both HMS and Météo-France. The cluster analysis was performed on a time cumulated histogram made from the infrared and visible images. The heights of cloud layers are represented by the infrared (IR) measurements, while reflectance values on the visible images (VIS) refer to cloud thickness, therefore, the peaks on the two dimensional histogram present different cloud types. Cluster analysis is a statistical tool to find these peaks automatically on the histogram. The standard deviation fields of the images

were used as well in order to separate cumuliform and layer clouds. The method of CMS was reported by *Bellec et al.* (1992) based on the algorithm of *Seze* and *Debois* (1987). In this method the standard deviation fields of the infrared data were involved as a third dimension of the histogram. For an attempt to use the method operationally during a test year in 1992, the clusters were automatically assigned to cloud types using thresholds for the kernels of the classes (centers of clusters). At HMS we worked out a method (*Diószeghy* and *Fejes*, 1995) based on the work of the already referred French authors (*Seze* and *Debois*, 1987) and also *Porcú* and *Levizzani* (1992). We used bispectral histograms and used a threshold for the standard deviation field of IR images. We tried to use kernels of multiyear cumulated monthly histograms to determine the clusters as traditional cloud types as they are used in the forecasters' terminology.

The clustering algorithm using visible and infrared data could separate distinct classes of clouds but this statistical approach requires a large amount of data accumulated in time and leads to the mixing of pixels with different surface conditions (temperature and albedo). Besides, the methods for automatically assigning cloud types to the clusters were not reliable enough. Therefore, in the frame of the co-operation with CMS we decided to establish a new cloud classification scheme based on a pixel by pixel approach.

2. Data requirements and collocalization

The new method is a combination of the statistical clustering and the threshold methods and as such besides Meteosat IR and VIS images it requires auxiliary data as well.

The spatial resolution of Meteosat images over Hungary is 6–7 km for the infrared and water vapor channels and 3–4 for the visible channel. The mash size of the nowcasting grid is a variable parameter, but usually it has a smaller resolution than that of the image. Satellite data are transformed to the grid. Pixel values are attributed to the nearest grid point. If more than one pixel found for one grid point then the maximum value is used for the visible and the minimum for the infrared images. This means an overestimation of the cloudiness and cloud development, but it is more appropriate for nowcasting purposes, especially for thunderstorm warning. All the other fields are also transformed to this grid within the MEANDER procedure, so all the input data of the cloud classification are available in the same resolution (*MEANDER*, 1999).

We need surface temperature fields, more exactly the brightness temperature of the surface, mainly for the separation of cloud free areas from low clouds. 2m temperature fields are used and transformed into surface brightness

temperature values according to the function found for NOAA/AVHRR derived brightness temperatures (*Brisson et al.*, 1997). We have to use model forecasts for the real time processing, but the field is corrected with SYNOP data already available at the time of the run of the nowcasting procedure. The used model outputs within MEANDER are from the ALADIN numerical weather prediction model running operationally at HMS (*Horányi et al.*, 1996).

For the surface reflectivity we use monthly surface albedo maps derived from Meteosat visible data (*Brisson et al.*, 1994). These maps were also transformed to the nowcasting grid.

Monthly "kernel library" was built using the centers of clusters of the test year (1992) at CMS. The automatic cloud type assignment to kernels was manually corrected and the average kernels of the months were derived. The values were transformed from the IR-VIS fields to physical parameters as cloud top temperature, variance of temperature and reflectivity values to be comparable to the surface parameters. We can say these kernels are the average cloud characteristics (cloud top temperature, its variance and reflectivity) of the different cloud types for the months. The kernels are given as linear functions of the surface parameters coming from regression analysis in case of surface dependent clouds. This dependence is especially important in the cloud top temperature of low clouds and reflectivity values of very thin cirrus. Different kernels were determined for sea and land cases and also for daytime and night-time classification. The grid of the nowcasting calculations at HMS consists of land points only. Details on the kernel library can be found in *Brisson et al.* (1997).

3. Cloud classification scheme

The flow diagram of the cloud classification algorithm is shown in *Fig. 1*. In this pixel by pixel method the raw visible and infrared counts disseminated by Meteosat are first transformed into physical units. VIS data are calibrated to reflectivity considering the calibration coefficients for the satellite, Sun-Earth distance for the day and illumination conditions. IR data are transformed to cloud top temperature values according to the Planck law. The standard deviation field of the cloud top temperature is derived in 3×3 pixel boxes and logarithmically rescaled in order to be comparable with the scales of the reflectivity and cloud top temperature values on the three-dimensional histogram. These 3 values of the pixel are then compared to the predetermined cloud characteristics, which means they are attached to the nearest kernel representing the average values of a certain cloud/surface type. These kernels are already actualized pixel by pixel as linear functions of the surface temperature and surface reflectivity. At night only the cloud top temperature and its vari-

ance can be used, and from the surface parameters, only the temperature. The kernels are also different at night and do not have reflectivity components. The boundary of the daytime and night-time classification is defined by an 80 degrees threshold applied on the solar zenith angle, thus it can happen that part of the image is classified as daytime classification while the other part as night-time classification. *Brisson et al.* (1997) describe more details on the classification algorithm. The cloud types are listed in *Table 1*.

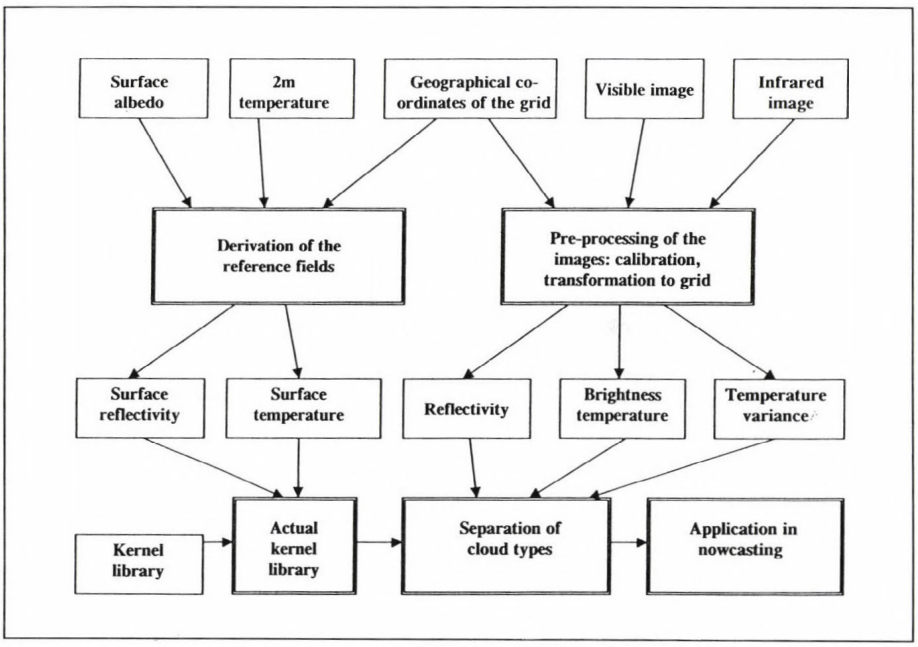

Fig. 1. Flow diagram of the cloud classification algorithm.

The visible channel is important in separating clear sky and cloudy pixels and evaluating cloud thickness. But for different illumination conditions the reflectance of the surfaces (land, sea, clouds) can vary, so it is difficult to compare consecutive images or different areas of the same image. Therefore, we use homogenized visible data for the continuity of the classification results throughout the day and the kernels were also corrected for the illumination conditions.

The usual homogenization procedure (dividing the reflectance values by the cosine of the solar zenith angle and normalizing to a constant angle) overestimates the reflectance values for high solar zenith angles due to anisotropy effects. We used the MODTRAN3.5 radiative transfer model (*Berk et al.*,

1989) for simulating reflectance values for cases representing all the illumination conditions (considering satellite zenith angle and relative azimuth angle as well) detailed enough for a further linear interpolation. We used different built in cloud models of MODTRAN. After the simulations we integrated the radiance values with filter functions of different satellite detectors. The validation was made with NOAA 12, Meteosat and ERB measurements (*Diószeghy et al.*, 1996). We had some difficulties for a limited range of the illumination conditions (forward scattering close to the sunglint case) which might be neglected for the Meteosat B format but will become important for further GOES and NOAA applications. We produced correction tables from the simulations by linear interpolation which can be used directly to measured radiance values. At the moment this correction method is used in the cloud classification scheme of CMS (Météo-France), where it is not in direct operational use, but it is applied for radiation calculations for ocean areas. For the nowcasting system of HMS this correction method would not be fast enough so only the mentioned cosine correction is used at the moment. Attempts are made to use the new analytical correction method of *Manalo-Smith et al.* (1998).

Table 1. Cloud categories of the classification scheme

No.	Cloud type	Abbreviation on figures	Remarks	Dependence on the surface
1	Clear	-		YES
2	Cloud edge	CE1		YES
3	Cloud edge	CE2	only night	YES
4	Thin cirrus	Ci		YES
5	Thick cirrus	Cs		YES
6	Cirrus + other clouds below	Ci+af		NO
7	Nimbostratus	Ns		NO
8	Small cumulus	Cu		YES
9	Cumulus mediocris	CuM	only day	YES
10	Cumulus congestus	CuC	only day	NO
11	Stratus	St		YES
12	Stratocumulus	Sc		YES
13	Altostratus	As		NO
14	Altostratus, Nimbostratus	As+Ns	only day	NO
15	Altocumulus	Ac	only day	NO
16	Cumulonimbus	Cb	May to October	NO

4. Verification and possibilities of combined use with radar data

At CMS, Météo-France, we compared the results to the earlier classification. Remarks of skilled nephanalysts were available for the selected test cases of 1992 to help the validation. Also the results of the classification were compared to the NOAA/AVHRR cloud analysis.

At HMS the verification work is done by the Forecasting Division. Two periods, from November 8 to December 31, 2000 and from September 1 to 30, 2001 were tested and all noon images were compared to SYNOP cloud codes. The verification was made within the Hungarian Advanced Weather worKstation (HAWK), where it is easy to visualize all available meteorological information together with satellite information (*Diószeghy et al.,* 1999). An example of the cloud classification results together with the IR image is shown in *Fig. 2a* and *b*.

The new scheme allows a homogeneous processing of all individual pixels. Earlier images had to be divided to small zones with different surface characteristics (mountains, etc). Some discontinuity remains however at the boundary of the daytime and night-time cases at sunrise and sunset.

The frontal cloudiness is generally well classified although cloud edges might appear as cirrus clouds. Subpixel cumulus clouds and very thin cirrus might be misclassified and at nighttime, in case of inversion (mainly winter), separation of very low clouds from clear areas is not possible with the only one IR channel of Meteosat. For very large Cb cells sometimes it occurs that the center of the cell is classified as Ns+Ci, as it is very homogeneous and cirrus cloud can cover the Cb (cirrus spissatus cumulonimbogenitus). For the forecasters it is not misleading but in statistics or in an automatic use for decision trees it can cause problems. We should remark that in case of very high Cb clouds, the top of the tower can be tilted with several pixels compared to the cloud base. Thus the position of the maximum of the VIS counts is shifted from the minimum of the IR counts in the image and it is very difficult to properly catch the Cb with a pixel by pixel or any other method (*Anthis et al.,* 1996).

An overestimation of cirrus clouds was reported by the forecasters. It is very difficult to compare the satellite based and surface based (SYNOP) cloud observations because of the different points of view. So it is natural that the satellite can see more high clouds while the observer can see the lower cloud layers. For the same reason it is nearly impossible to work out an objective and automatic verification procedure with SYNOP data. Only one layer cloud types can be compared and one should consider that a visual observer can see the dome of the sky with a 20–30 km radius, so all the satellite pixels within this area should be included in the comparison. At the moment the verification is interactive, but we made automatic statistical comparisons for precipitating cloud types with radar data.

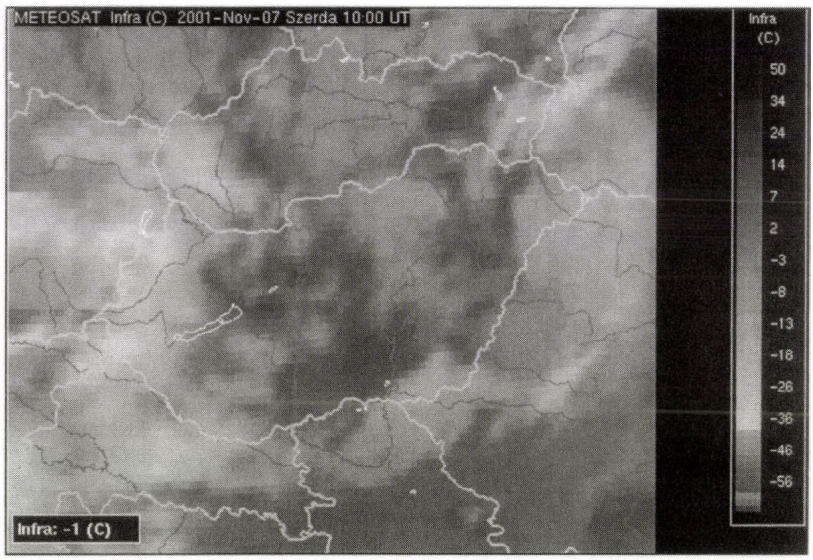

(a)

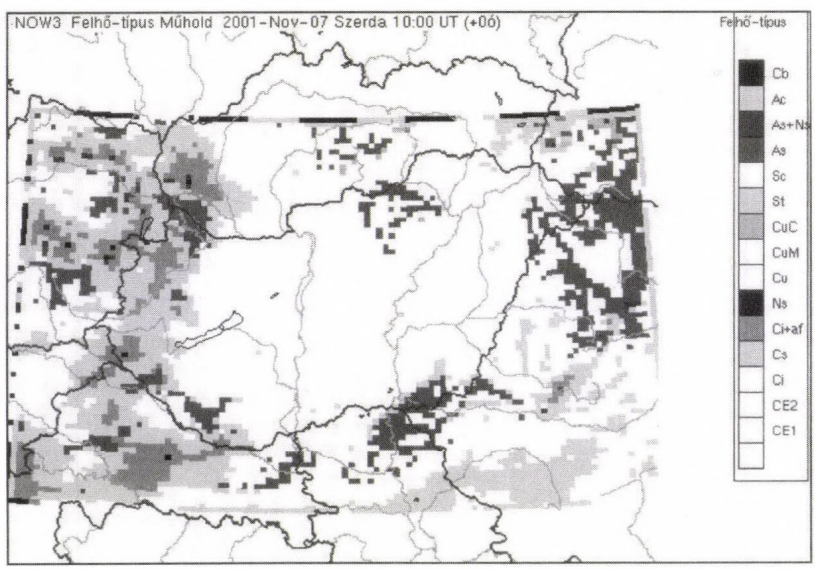

(b)

Fig. 2. Satellite and radar information for 10 UTC, November 7, 2001. (*a*) Infrared Meteosat image; (*b*) Cloud classification based on Meteosat data. For the black and white presentation we replaced the 16 colors with a special scale. All non precipitating types are white and the others are darker according to the precipitation possibilities. →

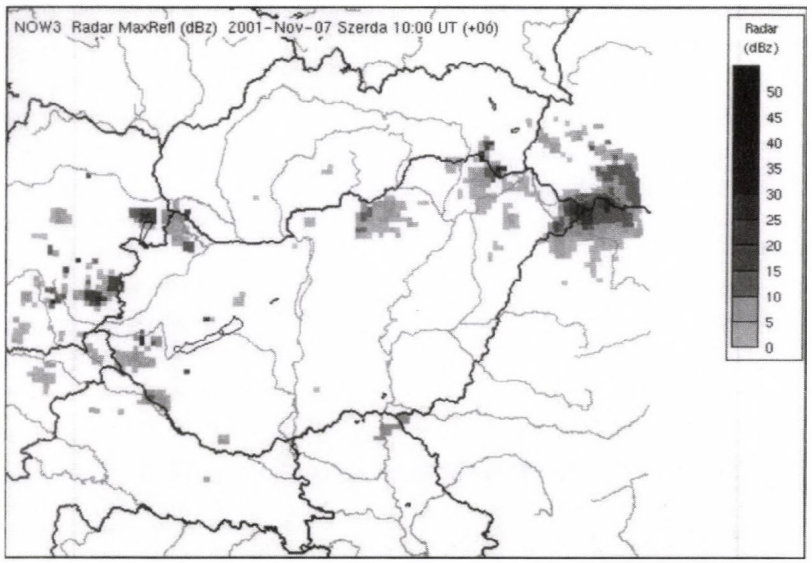

(c)

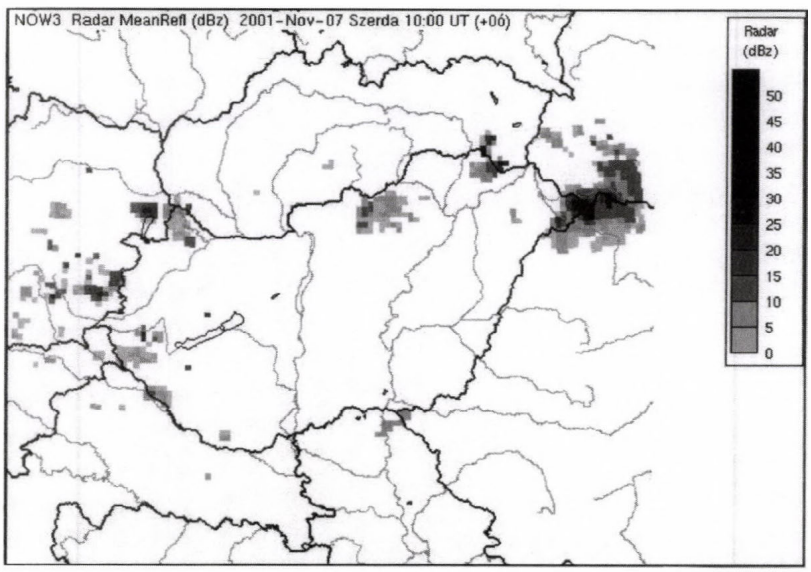

(d)

(*c*) Composite radar image made from the data of the three Hungarian radar stations and data from the neighboring countries. A median filter was applied. (*d*) Radar data after the filter according to non-precipitating cloud types of the satellite based cloud classification.

During a special experiment in summer 2001 we compared satellite and radar based cloud top height (CTH) values for the different cloud types (*Diószeghy et al.*, 2001). The aim of the study was to improve the precipitation and cloud information available for the nowcasting system of HMS as two important input of the different decision trees are the cloud top height and the radar intensity. Besides the radar based cloud top height measurements, an independent product from Meteosat data is available. As described in *Randriamampianina et al.* (2000), the cloud top height is calculated using satellite derived cloud top temperature compared to temperature profiles from numerical weather prediction model (ALADIN). As the radar and the satellite also observe the atmosphere from two different points of view, the reliability of the two methods depends on the cloud types. Results of the Meteosat based cloud classification of the nowcasting system were used to make a statistical comparison of the two cloud top height fields separately for the different cloud types.

From hourly satellite and radar CTH values we calculated difference fields and collected them together with cloud classification results for the summer months, June, July and August of 2001. Histograms of these differences were calculated for the different cloud types for all the data and also separately for night-time and daytime cases. Only those pixels were involved where radar echoes existed. *Fig. 3* shows some of these histograms for 5 selected cloud types.

Only types 5, 6, 7, 10, 13, 14, 16 (as listed on Table 1) have considerable peaks on the histogram as these are the precipitating clouds or precipitating clouds below cirrus clouds. The monthly histograms had different frequency values but the maximum of the peaks were placed at the same difference values, so we can consider this representative.

For most of the cloud types we can say that the satellite gives higher values, since it measures also the cirrus clouds above precipitating clouds. Also for the higher layers of Nimbostratus the echo can be very small and the radar can underestimate CTH. We should remark that in the cloud classification procedure we cannot separate Altostratus (As) and Nimbostratus (Ns) with satellite data alone, in the future we should include radar intensity values as well. A visual observer only calls an As as Ns after the first rain drops has fallen which cannot be determined by the satellite of course.

For Cumulonimbus (Cb) clouds the histogram is very flat and wide as the range of the differences between satellite and radar based CTH values can be very large. When overshooting cloud top occurs the difference is big and the radar measures higher and also more realistic values, since we cannot find equivalent temperatures for the cloud top in the numerical temperature profiles. Here we should notice that this difference value can be very useful for estimating the range of overshooting and from this the status of the develop-

ment and the maximum vertical velocity inside the Cumulonimbus clouds. But for this purpose we should update the cloud classification procedure first in order to have more accuracy in Cb detection.

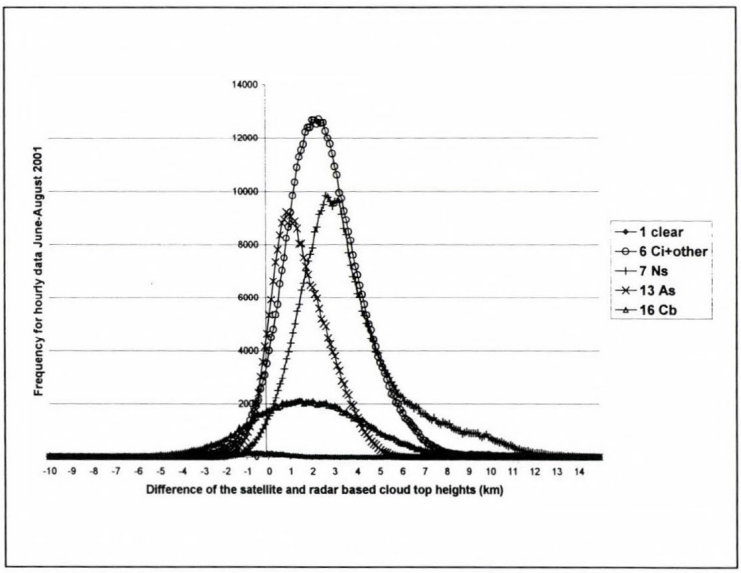

Fig. 3. Histogram of the differences between Meteosat and weather radar derived cloud top height values for different cloud types. All pixel values for hourly data of the period June 1–August 31, 2001.

The results of the comparison with radar data can also be used to determine the precipitating cloud types of the cloud classification to help to filter the radar fields from noise. In case the classification gives clear, cloud contaminated pixel or non raining clouds we can mask out the radar values. An example of this application is shown on *Fig. 2c* and *d*. First a median filter is applied to the original radar data (c), involving not only the three Hungarian stations but also the data of the neighbouring countries. Then we mask out the left noise with the cloud types (d). Since this filter is not yet verified the forecasters have access for both the filtered and non filtered data of course. On the figures the case of 10 UTC, November 7, 2001, is shown corresponding to Fig. 2a and b. Some noise around the Nyíregyháza-Napkor radar station of HMS were filtered out with the help of the cloud types. In this case no rain was reported at the neighboring synop stations.

5. Conclusions

- We found the new cloud classification algorithm applicable for operational use and the results are already available for the forecasters half hourly.
- At HMS the most important application of satellite based cloud types is the nowcasting system. It is one of the main inputs for the decision trees calculating "present weather" codes.
- In the future the conclusions of the study comparing radar and satellite based cloud top height values for different cloud types should be integrated in the decision trees of the nowcasting system and further we should make statistics considering the radar intensity values as well and compare them to different CTH values and cloud types.
- We should remark that satellite derived cloud types alone will never be as accurate as visual observations especially for low clouds or subpixel scale cumulus and very thin cirrus, but for frontal cloudiness and multilayer clouds it gives very important information for the forecasters. Combined use with radar data improves this information and the forthcoming MSG satellites will give lots of new possibilities in this field.

Acknowledgements—The cloud classification scheme was worked out in frame of a bilateral cooperation with Centre Météorologic Spatiale, Météo-France, and the essential input fields of albedo values and the kernel library were made available for us in the Hungarian adaptation. I am especially grateful to *Guy Rochard*, *Pierre Le Borgne*, *Anne Marsouin* and *Alain Brisson* and the financial support of the French Ministry for Foreign Affairs for the possibility to take part in this project. The study for cloud top height comparisons was partially supported by the Hungarian Scientific Research Foundation (OTKA-T031865).

***

I am very grateful for the supervising of *Dr. György Major*, for the help of the colleagues at the Satellite Research Laboratory and for the useful validation work of the forecasters of HMS.

References

Anthis, A.I. and *Cracknell A.P.*, 1996: Cloud classification of a typical synoptic situation affecting Greece using Meteosat data. *Proc. of the 1996 Meteorological Satellite Data Users' Conference, Vienna*. Austria, 16-20 Sept. 1996, EUM P19, 203-207.

Bellec, B., Brisson, A., Le Borgne, P., and *Marsouin, A.*, 1992: Operational cloud classification with Meteosat data. *Proc. of the Central Symposium of the ISY Conference*. Munich, 30 March - 4 April 1992, ESA SP-341, 323-327.

Berk, A., Bernstein, L.S., and *Robertson, D.C.*, 1989: *MODTRAN: A Moderate Resolution Model for LOWTRAN 7.* Air Force Geophysical Laboratory, Hanscom AFB, MA 01731, GL-TR-89-0122.

Brisson, A., Le Borgne, P., Marsouin, A., and *Moreau, T.*, 1994: Surface irradiances calculated from Meteosat sensor data during SOFIA-ASTEX. *Int. J. Remote Sensing 15*, 197-203.

Brisson, A., Diószeghy, M., Le Borgne, P., and *Marsouin, A.*, 1997: Classification nuageuse Meteosat: experience 1996 (in French). *Technical Report, CMS, Météo-France*, Lannion, France.

Derrien, M. and *Le Gléau, H.*, 1999: Cloud classification extracted from AVHRR and GOES imagery. *Proc. of the 1999 EUMETSAT Meteorological satellite Data Users' Conference*. Copenhagen, 6-10 September 1999, EUM P 26, 471-474.

Diószeghy, M. and *Fejes, E.*, 1995: Cloud classification derived from METEOSAT data involving the standard deviation fields of the brightness values. *Advances in Space Research 16*, (10)33-(10)36.

Diószeghy, M., LeBorgne, P., Marsouin, A., and *Putsay, M.*, 1996: Sun zenith angle correction applied to Meteosat visible data. *Proc. of the 1996 Meteorological Satellite Data Users' Conference*. Vienna, Austria, 16-20 Sept. 1996, EUM P19, 209-213.

Diószeghy, M., Horváth, Á., Randriamampianina, R., and *Szenyán, I.G.*, 1999: Applications of Meteosat images in the Hungarian Advanced Weather worKstation. *Proc. of the 1999 EUMETSAT Meteorological Satellite Data Users' Conference*. Copenhagen, 6-10 September 1999, EUM P 26, 471-474.

Diószeghy, M., Horváth, Á., Kerényi, J., Nagy, J., Németh, P., Randriamampianina, R., and *Sebők, I.*, 2001: Cloud and rain information for nowcasting from the combined use of weather radar and Meteosat data. *Proc. of the 2001 EUMETSAT Meteorological Satellite Data Users' Conference*. Antalya, 1-5 October, 2001, in press.

Geresdi, I. and *Horváth, Á.*, 2000: Nowcasting of precipitation type. Part I. Winter precipitation. *Időjárás 104*, 241-252.

Horányi, A., Ihász, I., and *Radnóti, G.*, 1996: ARPEGE/ALADIN: A numerical weather prediction model for Central-Europe with the participation of the Hungarian Meteorological Service. *Időjárás 100*, 277-301.

Manalo-Smith, N., Smith, G.L., Tiwari, S.N., and *Staylor, W.F.*, 1998: Analytic forms of bidirectional reflectance functions for the application to Earth radiation budget studies. *J. Geophys. Res. 103*, D16, 19733-19751.

MEANDER, 1999: Mesoscale Analysis Nowcasting and Decision Routines (in Hungarian; ed.: *Horváth, Á.*) Internal Publication of HMS, Budapest.

Porcú, F. and *Levizzani, V.*, 1992: Cloud classification using Meteosat VIS-IR imagery. *Int. J. Remote Sensing 13*, 893-909.

Putsay, M., Kerényi, J., Szenyán, I. G., Sebők, I., Németh, P., and *Diószeghy, M.*, 2001: Nighttime Fog and Low Cloud Detection in NOAA-16 AVHRR Images and Validation with Ground Observed Synop Data and Radar Measurements. *Proceedings of the 2001 EUMETSAT Meteorological Satellite Data Users' Conference*. Antalya, 1-5 October, 2001, in press.

Randriamampianina, R., Nagy, J., Balogh, T., and *Kerényi, J.*, 2000: Determination of cloud top height using meteorological satellite and radar data. *Phys. Chem. Earth (B) 25*, 1103-1106.

Seze, G. and *Desbois, M.*, 1987: Cloud cover analysis from satellite imagery using spatial and temporal characteristics. *J. Climate Appl. Meteor. 26*, 287-303.

IDŐJÁRÁS

Quarterly Journal of the Hungarian Meteorological Service
Vol. 105, No. 4 — Vol. 106, No. 1, October 2001 — March 2002, pp. 293-303

Using observed data for testing the statistical consistency of initial ensemble perturbations

István Szunyogh[1], Györgyi Gyarmati[2] and Dezső Dévényi[3]

[1]*Institute for Physical Science and Technology and*
Department of Meteorology, University of Maryland,
Computer and Space Sciences Building, College Park, MD, 20742-2431, USA
E-mail: szunyogh@ipst.umd.edu

[2]*Department of Meteorology, Eötvös Loránd University, Budapest, Hungary*

[3]*NOAA, Forecast Systems Laboratory and University of Colorado, CIRES, USA*

(Manuscript received February 22, 2002; in final form March 12, 2002)

Abstract—Two random variables are defined, one by an initial ensemble perturbation at a given geographical location, and another by the analysis uncertainty at the same location. The initial ensemble perturbations are said to be statistically consistent with the analysis uncertainty if the probability density functions of the two aforementioned random variables are equal. In this paper, it is shown how observed data can be used to test this statistical consistency. The usefulness of the proposed approach is demonstrated by an application to the global ensemble forecasting system of the National Centers for Environmental Prediction. Targeted dropsonde observations, collected during the 2000 Winter Storm Reconnaissance program, are used to show that increasing the rescaling frequency in the breeding cycle from once a day to four times a day improves the consistency of the initial ensemble perturbations.

Key-words: initial ensemble perturbations, statistical consistency

1. Introduction

The performance of an ensemble prediction system, especially for short forecast lead times, is mainly determined by the representativeness of the initial ensemble perturbations for the analysis uncertainty. Therefore, it is important to verify, whether the initial ensemble perturbations correctly represent the analysis uncertainty defined by the expected difference between analysis and truth. The chief difficulty with this verification is that the analysis

uncertainty cannot be directly determined since the true state of the atmosphere is unknown.

The most frequently used technique to avoid the aforementioned problem is based on Observing System Simulation Experiments (OSSE; *Houtekamer* and *Derome,* 1995; *Hamill et al.,* 2000), in which the "true state" of the atmosphere is obtained by a model integration. Hence, the analysis error statistics can be directly determined from a sample of the difference between the analysis and the simulated "true state". While the OSSEs have provided important insights into the strengths and the weaknesses of the different ensemble generation techniques, they cannot be used to measure the performance of an operational ensemble prediction system, whose goal is to predict the true state of the atmosphere.

In the operational practice, the quality of the initial perturbations is usually inferred from the performance of the ensemble at short (6–72 hours) forecast lead times. This approach is based on replacing the true state by its best estimate, the analysis. However, there are two important limitations of this technique. Firstly, the analysis errors are not negligible compared to the short-term forecast errors. Secondly, forecast errors are due not only to growing analysis but also to model errors. This means that the performance of the technique used to generate the ensemble perturbation cannot be separated from the short-term performance of the forecast model.

In this paper, we propose an alternative verification technique, for which the results are not affected by model errors. This technique exploits the opportunity provided by a unique set of targeted dropsonde observations collected during the 2000 Winter Storm Reconnaissance (WSR00) field program over the northeast Pacific. This data set has several favorable features (*Szunyogh et al.,* 2002):

- The instrument errors are small for the University Corporation for Atmospheric Research Global Positioning System (UCAR GPS) dropsondes that collected the data.
- The data were collected in regions of significant synoptical features that later had significant impact on the weather over the United States.
- Once assimilated, the data led to significant improvements in the 1–5 days forecasts over the United States. This indicates that the data are capable to detect errors in the analysis cycle that did not assimilate them.

Section 2 explains how observed data can be used to verify the statistical consistency of the initial ensemble perturbations. Section 3 demonstrates the usefulness of the technique by an application to the initial ensemble perturbations generated at the National Centers for Environmental Prediction/National Weather Service (NCEP/NWS) of the United States of America.

2. *Verification technique*

Let y^t, y^o, y^e, and x^a be random variables that represent, respectively, the true state, the observed state, the observational error, and the analysis at the observational location. These quantities are related through the following equation

$$(y^o - x^a) = (y^t + y^e) - x^a = (y^t - x^a) + y^e. \tag{1}$$

Our goal is to test whether the initial ensemble perturbations are representative for the difference between the true state and the analysis, $(y^t - x^a)$. This goal is achieved by (*i*) first replacing $(y^t - x^a)$ by the random variable x^p that represents an initial ensemble perturbation at the observational location and then (*ii*) comparing the two sides of Eq. (1). Since the variables are random, the equality of $(y^o - x^a)$ and $x^p + y^e$ can be verified only in a statistical sense.

Suppose that (*i*) sufficiently large samples of $(y^o - x^a)$ and x^p are available to estimate their probability density functions (pdfs), $f(z)$ and $h(z)$, respectively; and (*ii*) an estimate of the pdf of y^e, $g(z)$, is available. Our goal is to verify whether the initial ensemble perturbations are *statistically consistent* with the analysis uncertainty, i.e., whether $h(z)$ can be equal to the probability density function of $(y^t - x^a)$.

If the observations y^o are not used in preparing the analysis, the random variables that represent $(y^t - x^a)$ and y^e become independent. This means that the initial ensemble perturbation represents a random variable, which must be independent of the observational error. Therefore, the initial ensemble perturbation can be consistent with the analysis uncertainty, only if the pdf of $(y^o - x^a)$ is equal to the pdf of $x^p + y^e$; i.e.,

$$f(z) = \int_{-\infty}^{+\infty} h(z - v)\, g(v)\, dv. \tag{2}$$

The statistical consistency between the ensemble perturbation and the analysis uncertainty can be verified by the following algorithm:

- Compute the empirical density functions $f(z)$ and $h(z)$ based on a sample of $(y^o - x^a)$ and x^p at the observational locations.
- Choose a probability density function, $g(z)$, to represent the distribution of the observational errors.
- Compute the convolution $c(z)$ of $h(z)$ and $g(z)$:

$$c(z) = \int_{-\infty}^{+\infty} h(z - v)\, g(v)\, dv, \tag{3}$$

- Compare $c(z)$ and $f(z)$.

We note that one might (falsely) assume that there exists an alternative verification technique, in which Eq. (3) is applied to the alternative

$$(y^t - x^a) = (y^o - x^a) - y^e \tag{4}$$

form of Eq. (1). This way the pdf of $(y^t - x^a)$ could be directly determined from $f(z)$ and $g(z)$ and compared to $h(z)$. This approach does not work, however, because the two terms on the rhs. of Eq. (4) are not independent random variables; the observation (therefore the difference between the observation and the analysis) is not independent of the error in the same observation.

3. Application

During the WSR00 field program, nearly 300 dropsondes were released over the northeast Pacific on 12 separate flight days. To assess the forecast effect of the data, an additional analysis-forecast cycle was run parallel to the operational cycle. This parallel cycle was identical to the operational one, except no dropsonde data were assimilated (see *Szunyogh et al.*, 2002 for more details). The ensemble initial conditions evaluated in this study were prepared by perturbing analyses from the parallel cycle. This was done to ensure that the difference between the dropsonde observations and the unperturbed analyses is independent of the observational errors.

The computation of the difference between the observations and the analyses at the observational locations required the interpolation of the analysis fields, which were originally available on the Gaussian grid of the spectral NCEP model. The same interpolation was also needed to obtain the initial ensemble perturbations at the observational locations. Statistical samples were collected for the horizontal wind components and the virtual temperature at the 700 hPa, 500 hPa, and 300 hPa pressure level and for the surface pressure. At these levels observations were available from each sonde dropped during the field program. The empirical pdfs were estimated by the average shifted histogram technique (*Scott,* 1985) with using unit bins and shifting the unit-bin histograms twenty times.

The most difficult task was to find a proper statistical model for the observational errors. In this paper, the observational errors are assumed to be normally distributed and results will be shown for two different choices of the standard deviation. One of them is the manufacturer provided instrument error for the NCAR GPS sondes (*Hock* and *Franklin*, 1999), while the other one is the value assumed by the operational NCEP data assimilation system. The former choice is expected to provide an estimate of the lower bound of the

observational error since beyond the instrument error, the observational error also has an elusive representativeness error component. The observational errors assumed by the operational analysis scheme, on the other hand, include an implicit estimate of the representativeness error, since they are experimentally tuned to provide optimal forecast performance. The problem with this estimate is that the tunable parameter, the assumed observational error, may also be affected by other deficiencies of the analysis scheme (e.g., problems with the background error covariance matrix).

The initial ensemble perturbations were generated by the breeding technique (*Toth* and *Kalnay,* 1993, 1997), which is the operationally used method at NCEP. The current operational version of the algorithm is explained in detail in *Iyengar et al.* (1996) and *Szunyogh* and *Toth* (2002). Here, we provide an alternative explanation of the algorithm, which is more suitable for explaining the results of the present paper.

The purpose of the breeding technique is to mimic the effects of the analysis cycle on the growing analysis error. More precisely, it assumes that errors are growing freely in the direction of the atmospheric instabilities between two analysis cycles and the magnitude of the growing errors is reduced when observed data are assimilated. The operational breeding algorithm takes the analysis uncertainty into account through defining a seasonally varying *mask*, which is also a function of the geographical location. Formally, the *mask* is defined by the rms distance between analyses from two independent and nearly equal quality analysis cycles. That is,

$$mask = \sqrt{< (x^{a1} - x^{a2})^2 >}, \tag{5}$$

where x^{a1} and x^{a2} are the two independent analysis and the angled bracket denotes sample mean. The *mask* is also smoothed by a spectral filter, in such a way, that the variability at and below the synoptic scales (above wave number 10) is negligible. The ensemble perturbations, which evolve freely between two breeding cycles, are rescaled so that their magnitude at analysis time becomes equal to the *mask*. Since the *mask* is smooth this rescaling strategy can change only the magnitude, but not the structure, of the perturbations at the synoptic and smaller scales. We note that since the quality of the two analysis cycles is equal, $< (y^t - x^a)^2 >$ is the same for both cycles. Making use of the independence of the two cycles, it can be easily shown that

$$mask = \sqrt{2 < (y^t - x^a)^2 >}\,. \tag{6}$$

The *mask* used in operation was computed based on a one-year sample of daily analysis differences. It was prepared by considering one particular state

variable of the atmosphere, the rotational component of the horizontal wind. In the breeding algorithm the same local rescaling factor is applied to all state variables. Strictly speaking, this rescaling strategy assumes that there exists a linear relationship between the rotational wind and the other atmospheric state variables. While this is not an unrealistic assumption (e.g., the linear balance equation can provide the required linear relationship for synoptic and larger scale motions) there can be strong local deviations from this rule in the real atmosphere or in a model based on the primitive equations, such as the NCEP model.

Based on Eq. (6), it can be expected that the initial ensemble perturbations overestimate the analysis uncertainty, on average, by a factor of $\sqrt{2}$. This is not an error in the formulation. The initial analysis uncertainty is overestimated in order to compensate a deficiency of the ensemble: errors in the forecasts grow faster than the ensemble perturbations. Without overestimating the analysis uncertainty, the ensemble would underestimate the forecast uncertainty at all forecast lead times. The $\sqrt{2}$ factor can ensure that the ensemble spread, defined by the standard deviation of the ensemble, is equal to the average error in the ensemble mean at about three-day forecast lead time.

Two sets of initial ensemble perturbations were generated by running breeding cycles (*Toth* and *Kalnay*, 1997) for the duration of the WSR00 field program. In one of these cycles, the initial perturbations were generated by a replica of the operational breeding cycle. The other cycle was identical, except for that the perturbations were rescaled every six instead of every twenty-four hours. This change was expected to improve the consistency of the initial ensemble perturbations with the analysis uncertainty. In what follows, our verification technique is used to investigate whether this expectation was fulfilled by the experimental ensemble.

The results presented in *Fig. 1* for the surface pressure suggest the following conclusions: (1) the frequency of the large analysis errors is overestimated, while the frequency of the small analysis errors is underestimated by the ensembles, (2) this problem is more serious for the ensemble with 24-hour rescaling frequency, (3) the performance of the ensemble is found to be better when the smaller estimate of the observational error (the instrumental error) is used in the verification.

Interestingly, the above conclusions remain valid regardless of which state variable (temperature or wind) is used, even though the shape of the particular pdf is strongly variable dependent (*Fig. 2–Fig. 4*). The good agreement between the results for the different state variables indicates a systematic problem with the initial perturbations. To further investigate this problem, it is useful to define a measure that can characterize the difference between the

random variables compared by one single number. A straightforward choice is

$$\left(\frac{\sqrt{< x^{p2} >}}{\sqrt{< (y^o - x^a)^2 > - < y^{e2} >}} - 1 \right) \times 100, \tag{7}$$

which shows, in percentages, the extent to which the root-mean-square (rms) of the analysis uncertainty is overestimated by the initial ensemble perturbations. The results summarized in *Table 1* corroborate the conclusions drawn by visually inspecting the estimated probability density functions: the ensemble perturbations, on average, overestimate the analysis uncertainty. The only exception is the wind at the 300 hPa pressure level, but only when the smaller estimate of the observational error is considered.

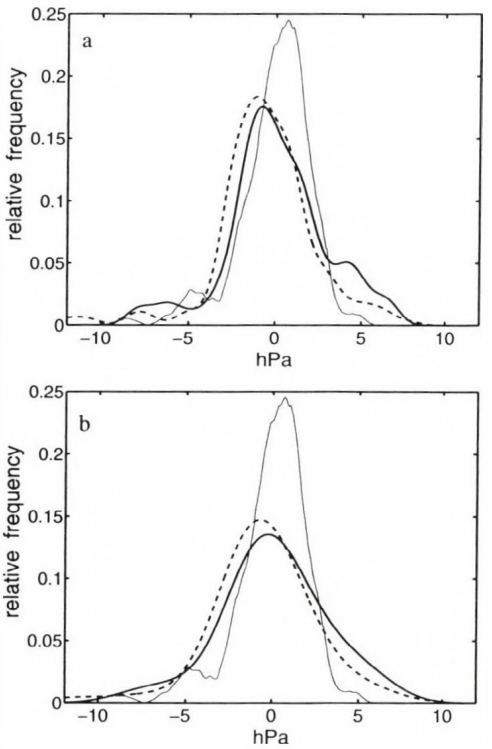

Fig. 1. Probability density functions for the surface pressure. Shown are the pdfs for $y^o - x^a$ (thin solid line), $x^p + y^e$ with 24-hour rescaling (solid line), and $x^p + y^e$ with 6-hour rescaling (dashes). The manufacturer provided instrument error is $y^e = 0.5$ hPa (panel *a*), while the observational error assumed by the data assimilation scheme is $y^e = 1.6$ hPa (panel *b*).

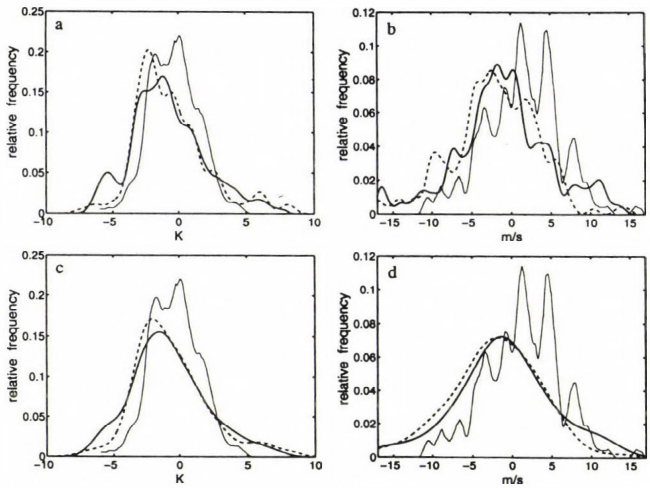

Fig. 2. Probability density functions for the temperature and wind at 700 hPa. Shown are the pdfs for $y^o - x^a$ (thin solid line), $x^p + y^\epsilon$ with 24-hour rescaling (thick solid line), and $x^p + y^\epsilon$ with 6-hour rescaling (dashes). The manufacturer provided instrument error for the temperature is $y^\epsilon = 0.2$ K (panel *a*), while the observational error assumed by the data assimilation scheme is $y^\epsilon = 0.8$ K (panel *c*). The instrument error for the wind is 0.5 m/s (panel *b*), and the assumed observational error is 2.4 m/s (panel *d*).

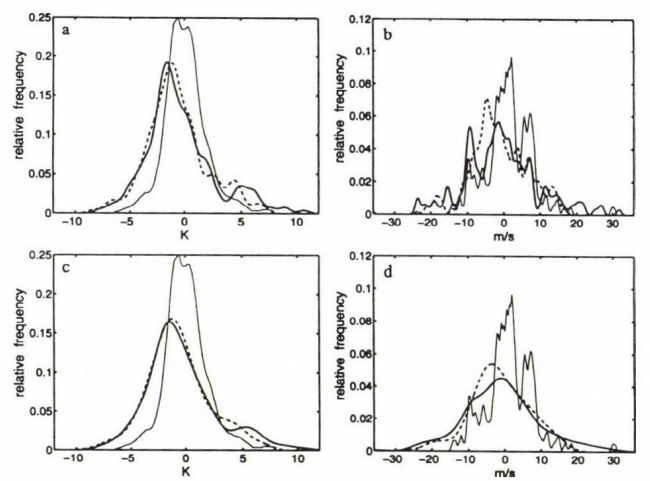

Fig. 3. Probability density functions for the temperature and wind at 500 hPa. Shown are the pdfs for $y^o - x^a$ (thin solid line), $x^p + y^\epsilon$ with 24-hour rescaling (thick solid line), and $x^p + y^\epsilon$ with 6-hour rescaling (dashes). The manufacturer provided instrument error for the temperature is $y^\epsilon = 0.2$ K (panel *a*), while the observational error assumed by the data assimilation scheme is $y^\epsilon = 0.8$ K (panel *c*). The instrument error for the wind is 0.5 m/s (panel *b*), and the assumed observational error is 2.8 m/s (panel *d*).

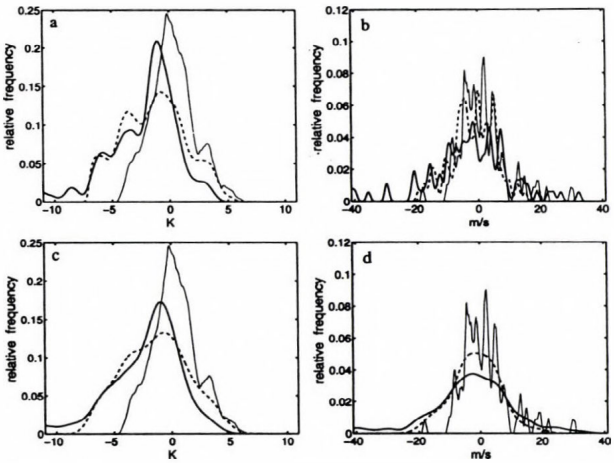

Fig. 4. Probability density functions for the temperature and wind at 300 hPa. Shown are the pdfs for $y^o - x^a$ (thin solid line), $x^p + y^e$ with 24-hour rescaling (thick solid line), and $x^p + y^e$ with 6-hour rescaling (dashes). The manufacturer provided instrument error for the temperature is $y^e = 0.2$ K (panel a), while the observational error assumed by the data assimilation scheme is $y^e = 0.8$ K (panel c). The instrument error for the wind is 0.5 m/s (panel b), and the assumed observational error is 2.8 m/s (panel d).

Table 1. Overestimation of the analysis uncertainty by the initial ensemble perturbations (for definition see Eq. (5)). Shown are the selected state variables (first column), the pressure levels at which the observations were taken (second column), the estimated observational error (third column), overestimates in the 6-hour rescaling cycle (fourth column), and in the 24-hour cycle (fifth column)

Variable	**Level**	y^e	**06-h rms %**	**24-h rms %**
Pressure	Surface	1.6	140	160
Temperature	300	0.8	60	85
Wind	300	2.8	6	84
Temperature	500	0.8	68	93
Wind	500	2.8	35	81
Temperature	700	0.8	68	68
Wind	700	2.4	32	45
Pressure	Surface	0.5	49	61
Temperature	300	0.2	46	69
Wind	300	0.5	−1	71
Temperature	500	0.2	52	75
Wind	500	0.5	22	63
Temperature	700	0.2	52	52
Wind	700	0.5	15	26

As it can be expected by considering the specific form of Eq. (7), the overestimation of the analysis uncertainty is always found to be a less serious problem when the smaller estimate of the observational error is used. What could not be predicted by simply considering Eq. (7) is the fact that the overestimation is always smaller for the more frequent rescaling. Nevertheless, this result is in good accordance with the conclusions drawn based on comparing the pdfs.

The initial ensemble perturbations overestimate the analysis uncertainty, on average, by 38,7% in the 6-hour breeding cycle, and by 67.1% in the 24-hour cycle. (These values were obtained by disregarding the grossly overestimated surface pressure uncertainty and assuming that the results can be averaged for the two different estimates of the observational error.) This result is remarkable considering that the overestimation of the analysis uncertainty by the breeding cycle with 6-hour rescaling (38.7%) is extremely close to the value (about 41%) that can be expected based on Eq. (6). It should be recalled that the *mask* controls the large-scale areal mean of the magnitude of the initial ensemble perturbations, but it has little effect at the synoptic scale, where the energetically dominant baroclinic instabilities are the most intense. Our results, therefore, show that in the regions of atmospheric instabilities, where the observations were collected, the 6-hour rescaling provides perturbations, which are more consistent with the estimates of the analysis uncertainty. (The 24-hour rescaling tends to overestimate the analysis uncertainty in the regions of baroclinic instabilities.)

The relatively large variability of the numbers in Table 1 for the different state variables can be attributed to a couple of possible factors. Firstly, the representativeness error can be different for the different variables. Secondly, as mentioned before, the breeding algorithm rescales all variables with the same factor at a given geographical location, which can lead to inconsistencies in the regions where the linear balance equation is not satisfied.

4. Concluding remarks

In this paper, a new and simple statistical technique was introduced to test the statistical consistency between initial ensemble perturbations and analysis uncertainties. Our study indicates that better statistical consistency can be achieved with the breeding technique when the ensemble perturbations are rescaled every 6 instead of every 24 hours. This result is not surprising considering that the purpose of the breeding technique is to mimic the effects of the analysis cycle on the growing analysis errors. Based on this consideration, the rescaling was done every 6 hours at the time (in 1992) when

operational ensemble prediction was introduced at NCEP. This meant, however, that an extra day of ensemble integration was needed to evolve the initial ensemble perturbations and a 24-hour rescaling was introduced soon to save computer time. In this new setup the regular 24-hour ensemble forecasts were rescaled.

Partly based on the results presented here, NCEP is considering to return to the 6-hour rescaling later this year. The preliminary forecast verification results (not shown in this paper) indicate that increasing the rescaling frequency also improves the skill of the individual ensemble members.

Acknowledgments—We would like to thank the staff of EMC, and in particular *Dr. Zoltan Toth* and *Jack Woollen*, for their support of this work. *Dr. András Horányi* provided helpful comments on an earlier version of the manuscript. The research presented in this paper was partly supported by the *W. M. Keck Foundations*.

References

Hock, T.F. and *Franklin, J.L.*,1999: The NCAR GPS Dropwindsonde. *Bull. Amer. Meteor. Soc. 80*, 407-420.

Hamill, T., Snyder, C., and *Morss, R. E.*, 2000: A comparison of probabilistic forecasts from bred, singular vector, and perturbed observation ensembles. *Mon. Wea. Rev. 128*, 1835-1851.

Houtekamer, P.L. and *Derome, J.*, 1995: Methods for ensemble prediction. *Mon. Wea. Rev. 123*, 2181-2196.

Iyengar, G., Toth, Z., Kalnay, E., and *Woolen, J.S.*, 1996: Are the bred vectors representative of analysis errors? *Preprints, AMS Conference on Numerical Weather Prediction*, Norfolk, VA, 64-65.

Scott, D.W., 1985: Averaged shifted histograms: Effective nonparametric density estimators in several dimensions. *Annals of Statistics 13*, 1024-1040.

Szunyogh, I. and *Toth, Z.*, 2002: The effect of increased resolution on the NCEP global ensemble mean forecasts. *Mon. Wea. Rev. 130*, 1125-1143.

Szunyogh, I., Toth, Z., Majumdar, S.J., and *Persson, A.*, 2002: On the propagation of the effect of targeted observations: The 2000 Winter Storm Reconnaissance Program. *Mon. Wea. Rev. 130*, 1144-1165.

Toth, Z. and *Kalnay, E.*, 1993: Ensemble Forecasting at NCEP: The generation of perturbations. *Bull. Amer. Meteor. Soc. 74*, 2317-2330.

Toth, Z. and *Kalnay, E.*, 1997: Ensemble forecasting at NCEP and the breeding method. *Mon. Wea. Rev. 125*, 3297-3319.